NASA Contractor Report 3570

Generation of X-Rays and Neutrons With a RF-Discharge

Richard T. Schneider

CONTRACT NAS1-15812
JUNE 1982

NASA

NASA Contractor Report 3570

Generation of X-Rays and Neutrons With a RF-Discharge

Richard T. Schneider
RTS Laboratories, Inc.
Gainesville, Florida

Prepared for
Langley Research Center
under Contract NAS1-15812

National Aeronautics
and Space Administration

Scientific and Technical
Information Office

1982

Contributors to this work were:

Peter H. Handel*, Consultant to RTS Laboratories, Inc.
M.J. Rowe, RTS Laboratories, Inc.
B.D. Carter, RTS Laboratories, Inc.

Independent detection of neutrons was performed by

William H. Ellis, University of Florida, Gainesville, Florida

*Address: University of Missouri, St. Louis, Missouri 63121

TABLE OF CONTENTS

I. INTRODUCTION

The present report describes a new device in which unusual discharge characteristics with generation of neutrons from nuclear fusion reactions are observed at very modest input power levels of the order of 100 W. In addition, X-rays of energy higher than what the 1000 V amplitude of the applied high frequency (HF) voltage would normally allow, are generated.

The two main advantages of a HF discharge in general are: 1) the principal possibility of resonance phenomena which may accelerate particles or may excite collective modes up to very high energies with modest HF power inputs; 2) the absence of electrodes in contact with the plasma. The spectacular results obtained with the new device are at least in part due to these two major advantages.

There is, however, another important, fundamentally new advantage which is directly related to the name of the new device: ENRAD. This acronym means "Electrostatically Confined Nuclear Radiation Device" and was coined by the authors on the basis of physical intuition long before the novel confining principle of the device, which justifies its name, was understood. The new advantage is based on a new confinement principle which is stated here for the first time: rather than confine the plasma from the outside with a field, it is preferable to confine the field from the outside with a plasma, i.e., to have the electric field localized inside a radiation bubble, surrounded by a plasma which in turn is embedded in layers of neutral gas. The basic reason is that the field is coherent, and, therefore, characterized by fewer degrees of freedom and more stable, while the plasma is incoherent and characterized by a larger number of degrees of freedom, many of which are very unstable. The plasma does not need to be in thermal equilibrium but must form a resonant state together with the field. This combined state of plasma and electrostatic field is a new type of solution of a nonlinear equation which describes what is in essence a localized standing electrostatic (Langmuir) wave, a particular type of soliton, and a special case of what has become known in the last decade as plasma caviton. The properly tuned discharge consists of one or more pairs of luminous disks. Each pair is invariably separated by a sharply defined dark space of about 0.5 cm width which does not depend on pressure and is, therefore, fundamentally different from the familiar striations often observed in d.c. or a.c. discharges. The disks occur only in pairs, and are the source of a spectrocopically identified axially directed beam of deuterons, and also of keV x-rays.

On the basis of this experimental evidence, we have been able to identify the discharge with just one pair of disks as a ground state electrostatic plasma caviton and the states with n pairs of disks as the corresponding (n-1)-th excited cavitonic state. The caviton is resonant with, and pumped by, the applied HF field. The sharply defined dark space is occupied by the strong localized electric field of the caviton, which exceeds the amplitude of the applied HF field by a factor of the order of 10^3 and which oscillates at a frequency which differs from the local plasma frequency by a small amount determined as the eigenvalue of the cavitonic state. The luminous disks represent the walls of the density cavity which houses the localized electric field of the caviton, and are active in defining the caviton. Inside the caviton the plasma concentration is by about two orders of magnitude lower than the surrounding plasma concentration due to the action of the ponderomotive force of the localized field which pumps the plasma out and thereby reduces the convective loss of energy of the caviton in form of electrostatic (Langmuir) waves and electromagnetic waves. This, in turn, facilitates the further increase of the localized resonant electric field and the deeper excavation of the density cavity.

The initial generation of the caviton is explained in detail in the present report (Sec. V). The explanation is based on a resonance between the applied HF field of frequency ω and the plasma frequency $\omega_p = (4\pi ne^2/m)^{1/2}$ in the center of the device as soon as the HF power is applied to the device and as soon as the electron concentration reaches the level $\omega_o(m/4\pi e^2)^{1/2}$ in the center of the device. The ENRAD cavitons are obtained at pressures of the order of 1 torr which is about a thousand times higher than the pressures at which cavitons were obtained previously.

Due to its unique resonance properties, the ENRAD device has the potential to be developed into a controlled fusion device. As suggested by Handel in 1974, natural plasma cavitons, pumped by huge atomospheric H_2O masers may already be known as ball lightning.

The intriguing question which arises is why does a plasma caviton arise in this device and not in any other simple d.c. or a.c. gas discharge? To understand why, we note that due to the ring-shape of the electrodes and their positioning outside the discharge tube, an extended quasi-homogeneous high-electric field volume is present in the center of the device. This is an electrostatic analog of the familiar Helmholtz coils. Due to the remoteness of all solid surfaces which could produce increased plasma recombination, the plasma density exhibits an extended, flat maximum in the center of the device, with a quasi-homogeneous concentration of electrons and ions which is steadily increasing from zero after the HF field is turned on. After 10-20 periods of the HF-fields at the nominal field amplitude, the local electron plasma frequency $(4\pi ne^2/m)^{1/2}$ in the center of the device approaches the frequency ω_o of the applied field. Since the dielectric constant of the plasma (derived in Sec. V) is $\varepsilon = 1 - \omega_p{}^2/\omega^2$, it approaches zero in the median plane, i.e., at the center of the device. On the other hand $\vec{D} = \varepsilon\vec{E}$ = const. in the space between the electrodes. Therefore, in the resonant volume at the center of the device $\vec{E} \to \infty$ when n increases to the point where $\omega = \omega_p$. Moreover, this strongly enhanced electric field amplitude is in resonance with the free electrostatic oscillations of the electrons. Indeed, under the influence of the strong electric field present only in the median plane of the device electrons are depleted on the +E side and accumulated on the -E side. Electrostatic repulsion, which is the restoring force of the Langmuir waves, causes the electrons to rebound after $T_{p/2}$, where $T_p = 2\pi/\omega_p$. However, since $\omega_o = \omega_p$ in the center plane of the device, the electric HF field will have changed its direction also meanwhile. Therefore, the electrons will be accelerated again, and rebound even stronger, like a harmonic oscillator, whose period does not depend on the amplitude; this is true for electrostatic waves. The electrons are, therefore, continuously accelerated by the electric field which is always in phase. The resonance process enhances the average kinetic energy and the kinetic pressure of the electrons in the resonance volume dramatically, thereby creating a density cavity. The amplitude of the electric field and of the electronic oscillation would increase indefinitely if it were not bounded by two processes which carry away approximately equal amounts of energy: a) the generation of high amplitude Langmuir waves which propagate away from the central plane in both directions towards the hollow electrode-planes, and b) the acceleration of ions up to energies of tens or hundreds of keV, leading to fusion reactions at very modest HF powers.

The creation of the initial density cavity reduces the loss of electromagnetic and Langmuir wave energy due to the formation of a resonator-like structure with conducting cavity walls. This reduction in loss causes another, additional electric field increase in the caviton and in turn a deeper excavation of the density caviton until a dynamic equilibrium structure emerges, with very high values of the electrostatic and plasma kinetic energy, with vacuum inside, limited by nonlinear and loss phenomena, the ENRAD caviton. This is a dark space between two luminous disks. The inner side of the disks appears blueish due to the action of primary electrons and ions which have higher energies, while the outside regions of the disks appear reddish in color due to the lower excitation energies of the bombarding particles and of the radiating species in the tails of the plasma distribution of the caviton.

We can also understand the initial large accumulation of electromagnetic field energy at the resonant region in the center of the device by following the field lines of the Poynting vector $\vec{S} = \frac{c}{4\pi} \vec{E} \times \vec{B}$ which represents the energy current density. These enter the discharge tube radially, i.e., laterally through the glass walls, perpendicular to $\vec{E}$ and $\vec{B}$. The energy flows in with the group velocity $v_g = d\omega_o/dk = c\sqrt{\varepsilon}$ which is derived from the dispersion relation (Eq. 4.6)

$$\omega_o^2 = \omega_p^2 + c^2k^2$$

and is therefore $v_g = \sqrt{c/(1-\omega_p^2/\omega_o^2)}$. At the center of the device $\omega_p = \omega_o$ and $v_g = 0$, i.e., the buck stops there... Energy, again would pile up indefinitely because in the electromagnetic energy current the product of energy density w and group velocity must be constant in stationary conditions, as required by the continuity equation

$$\frac{\partial w}{\partial t} + \nabla \cdot (w\, \vec{v}_g) = 0$$

i.e.

$$\vec{S} = w\, \vec{v}_g = \text{const. along the field lines of } \vec{S}.$$

Since $v_g \to 0$ we have again $w \to \infty$. This line of thought is equivalent to the initial $D = \varepsilon E$ argument, used above.

The most amazing property of the ENRAD device is the excellent stability of the obtained cavitons against instabilities and collapse. This allows the unlimited c.w. operation of the device at the relatively high pressures of more than 1 torr which exceeded by at least three orders of magnitude any previous observations of laboratory cavitons. Concomitantly, the electric field and the particle energies are also by about 3-4 orders of magnitude larger in our device, therefore allowing for fusion reactions and x-ray emission.

We are sure that the pressure and the energy density can be further enhanced in the ENRAD device and we believe that this is the way to solve the fusion problem.

II. EXPERIMENTAL SETUP

1. The ENRAD Principle

ENRAD stands for electrostatically confined nuclear radiation device. Basically, the intention is to contain a field inside a plasma, rather than going the usual way where a plasma is confined within some sort of field configuration. For the field to exist within the plasma, it has to displace the major part of the plasma within a certain region (dig itself into the plasma). The result should be a low density region surrounded by a steep density gradient. The resulting plasma cavity (caviton) gives charged particles trapped inside an opportunity to obtain energy in the applied radiofrequency field (RF) until they become too energetic to follow the vibrations of the RF field and are ejected from the cavity region. They collide with the plasma wall giving rise to excitation, ionization and possibly some fusion reactions.

There are probably more than one electrode configuration which will shape a field in a way that it can "dig in." The present experiments used two cooper rings, placed outside of the discharge tube, so that the coupling is capacitive. Electrode distance is about twice the electrode diameter. The wavelength of the applied RF is large compared to the electrode distance or diameter, so that initially a fairly homogeneous field can be expected between the electrodes.

In the following two different discharges which are based on the ENRAD principle are discussed. Both use the same electrode configuration. One discharge is a pulsed DC-high voltage discharge, while the other one is a low voltage RF discharge.

The work concerning the high voltage discharge was done more than 10 years ago, while the work on the RF discharge was done under the present effort. However, only now, after having the results of the RF discharge, can we understand the results of the older work.

2. High Voltage Discharge

The high voltage discharge is excited by a voltage pulse, 5 μsec wide and 60 kV high. Its repetition rate is 50 hz. The voltage pulse is capacitively coupled to the plasma, using the ENRAD configuration. The relatively high repetition rate has several advantages. One of them is the outgassing of the structure which results from repeated electrical pulses, driving out contaminating wall gases and permitting the operation of a stable relatively reproducible plasma. Another advantage is that the residual gas pressure can be stabilized after a short time of operation.

The pulse generator used can produce voltage pulses as high as 100 KV and currents as large as 100 A. The pulse duration is approximately five microseconds and the repetition rate may be either 60 Hz or 400 Hz. The shape of the pulse is, to a large extent, determined by the load characteristics which in the case of the gaseous discharge vary considerably with the operating condition. Since the high field gradients produce a large amount of ozone in the surrounding atmosphere, the tube and electrodes have been enclosed by a large steel tank equipped with suitable ports for observation. This tank serves to confine the ozone and prevent its entrance into the experimental environment. It also acts as a good X-ray shield. Still another advantage of this enclosure is the electrical shielding which results, reducing interference to measuring equipment in the immediate vicinity of the discharge.

Figure II-1 shows the schematic diagram of the power supply. The trigger circuits consist of an adjustable phase, synchronous pulse generator which serves to trigger an intermediate level trigger, a thyratron

Figure II-1 Schematic Diagram of Power Supply and Discharge Tube.

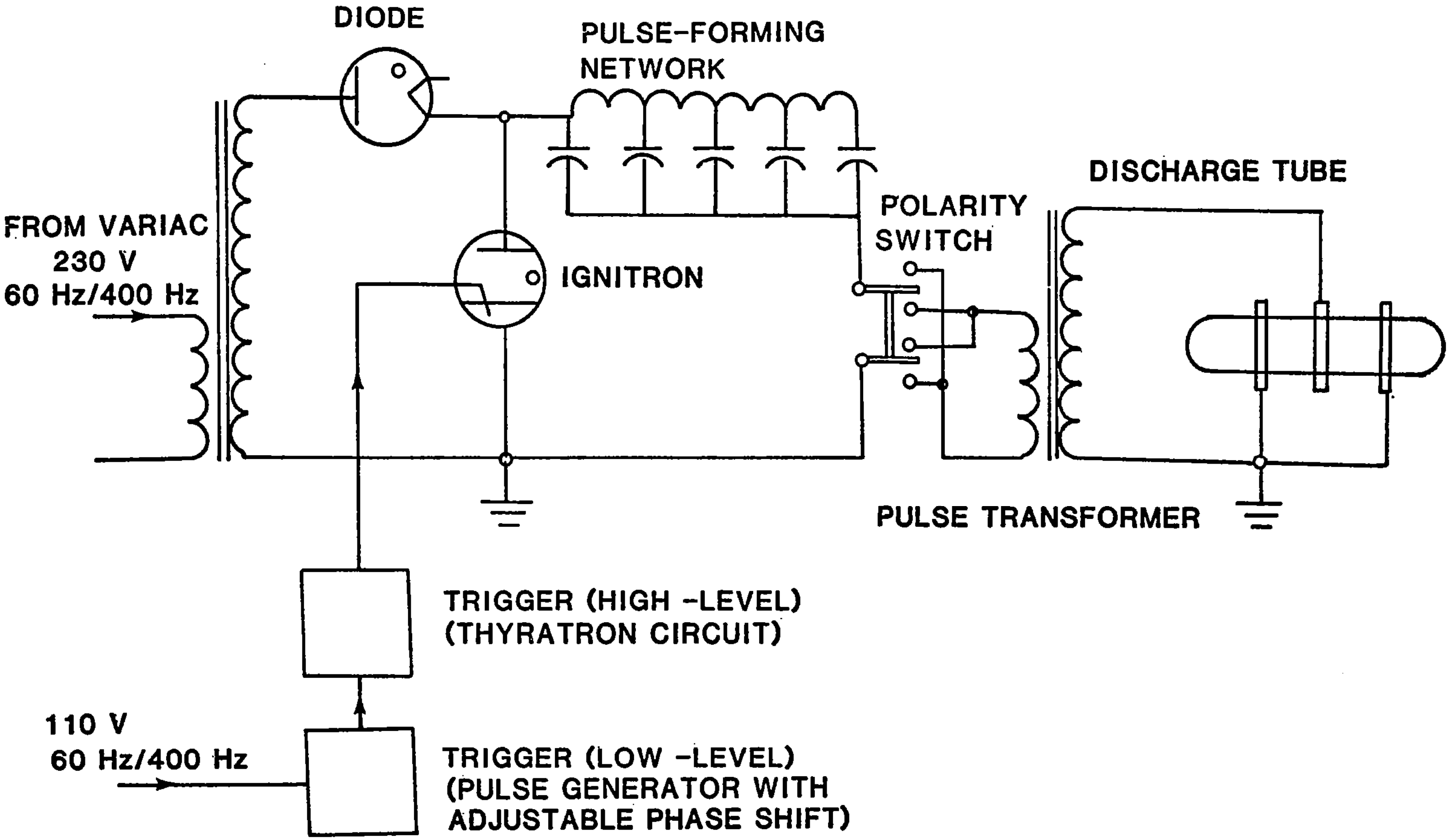

circuit which, in turn, triggers a high-power ignitron circuit supplying energy to the high-level pulse transformer which supplies the 100 KV pulse.

Energy for the high-level pulse is obtained by discharging a transmission line which can be adjusted to produce various wave forms of the resultant pulse. This energy storing line is charged by a diode and fired during the nonconducting portion of the cycle thus establishing synchronous operation. The pulse repetition rate is thus established by the source frequency. Such modulators are employed in most high-powered pulse work.

A switch is provided to change the pulse polarity. In the following discussions, the term "positive" or "negative polarity" is defined as the potential of the ungrounded electrode.

The discharge tube consists of a cylindrical Pyrex glass tube 200 cm long and 8 cm in diameter. Three cylindrical Al-electrodes are placed on the outside of the tube as can be seen in Figure II-2. This figure also shows the above mentioned enclosure. As pointed out, the power input is transferred to the plasma by capacitive coupling. The central electrode has guard rings in order to reduce the corona discharge on the outside of the tube. The tube was filled with either hydrogen or deuterium at pressure levels between 10 and 200 microns.

A closer look at the relationship between current and voltage reveals an important feature of this discharge, namely that the current rings in the 1 Mhz range, although the applied voltage, is a dc pulse. This can be seen in Figure II-3 where the applied voltage pulse is +50 KV high and 4 μsec wide, while the current rings (positive and negative values of current) at high frequencies.

Figure II-2 Dimensioned Tube Enclosure

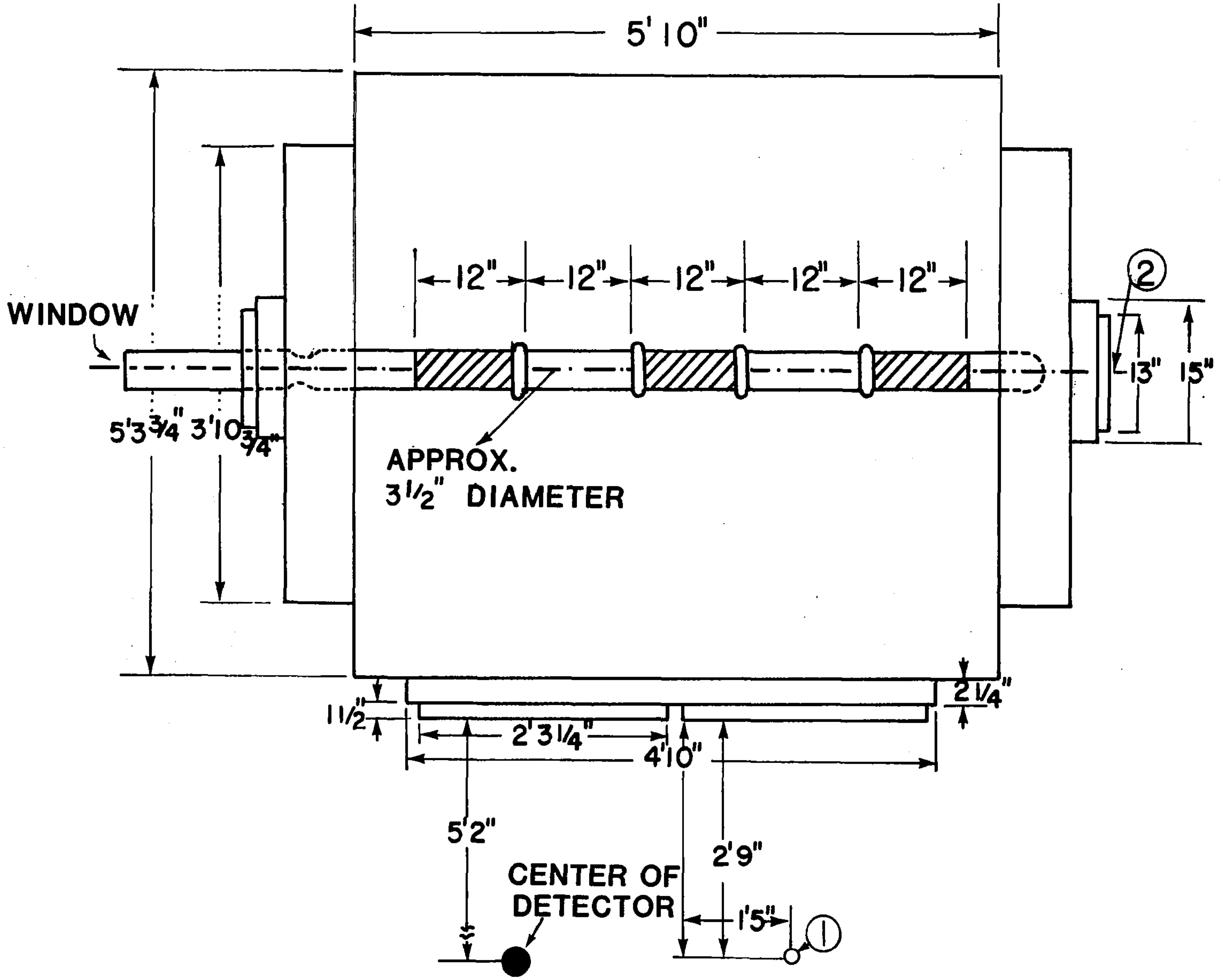

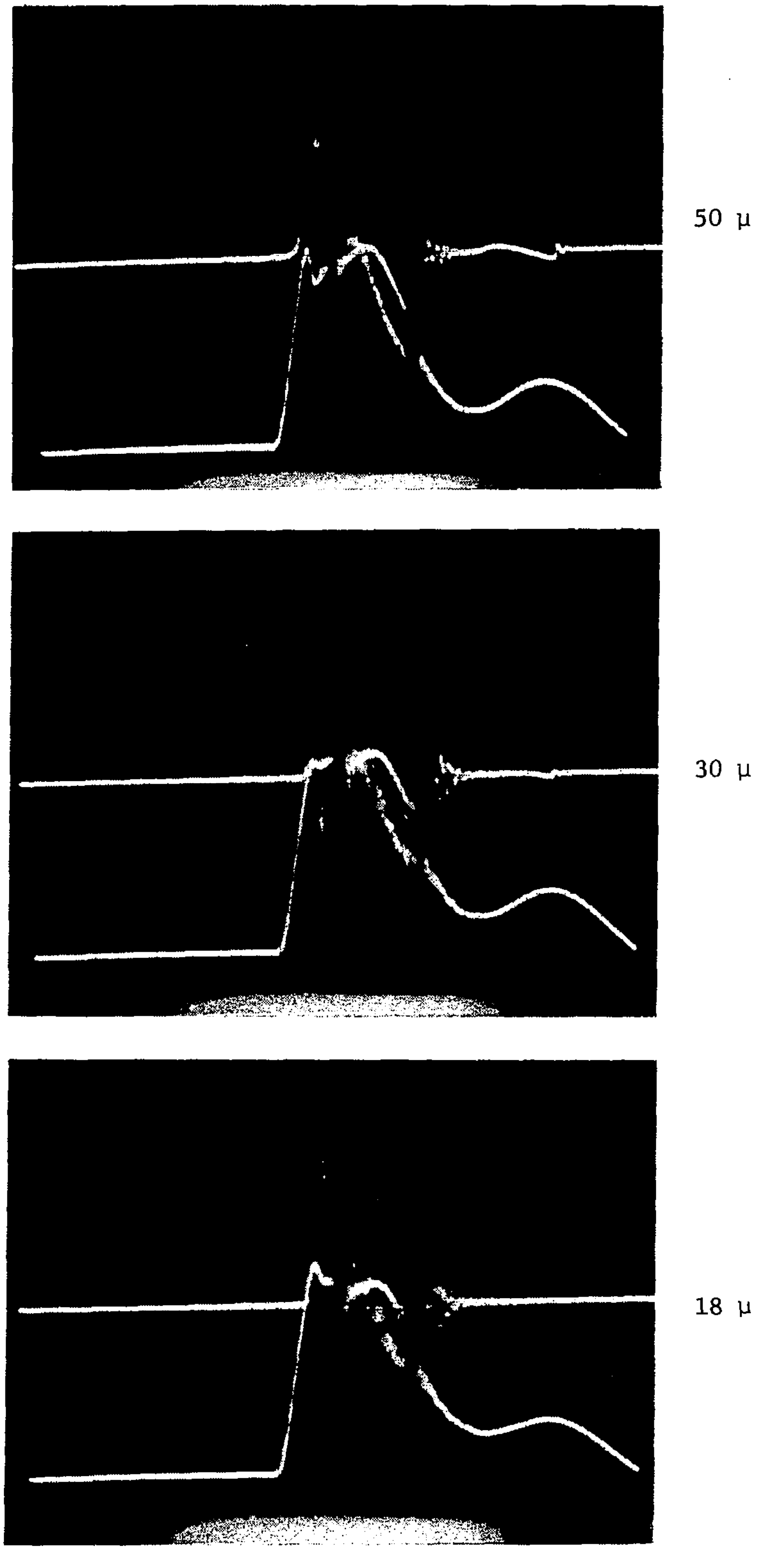

Figure II-3 Relation between Current (Top Trace) and Voltage (Botton Trace) at 50 kV Pos. Pulse Polarity (Time Base 2 μsec/cm) for various pressures.

3. Low Voltage Discharge

a) Description

The low voltage system consists of a test section, a matching circuit, a driver unit, a gas handling system-pump station and a diagnostic unit as shown in Figure II-4. The driver unit is a 500 watt RF power supply (0.5 to 1.7 Mhz) feeding a matching circuit instead of a conventional antenna system. The matching circuit is a variable L-C network which allows matching of the output impedance of the RF power supply to the imput impedance of the test section.

The test section consists of a 80 cm long glass tube (7740 borosillicate glass) having an outer diameter of 10 cm. According to the ENRAD Principle, the HF is capacitively coupled into the fill gas of the test section by two ring electrodes which are again attached to the outside wall of the glass tube. Intra-electrode distance is typically 5 - 50 cm.

The gas fill for the test section is introduced through the gas handling system while the vacuum is monitored and maintained through a separate port. This configuration allows studies with either static or dynamic gas fills.

b) Operational Characteristics

Like all gas discharges, this device has a breakdown voltage which is a function of pressure and electrode separation. It is usual to present such relationships in the form of E/p vs pd. (E: electric field, p: pressure, d: electrode distance). The breakdown E/p is shown in Figure II-5 for a frequency of 1.34 Mhz, which is the primary frequency used for the data in this report. The dependence on frequency is weak. As a comparison, an argon HF-discharge at 3000 Mhz is shown. [II-1] The discharge characteristics are quite similar despite the large difference in

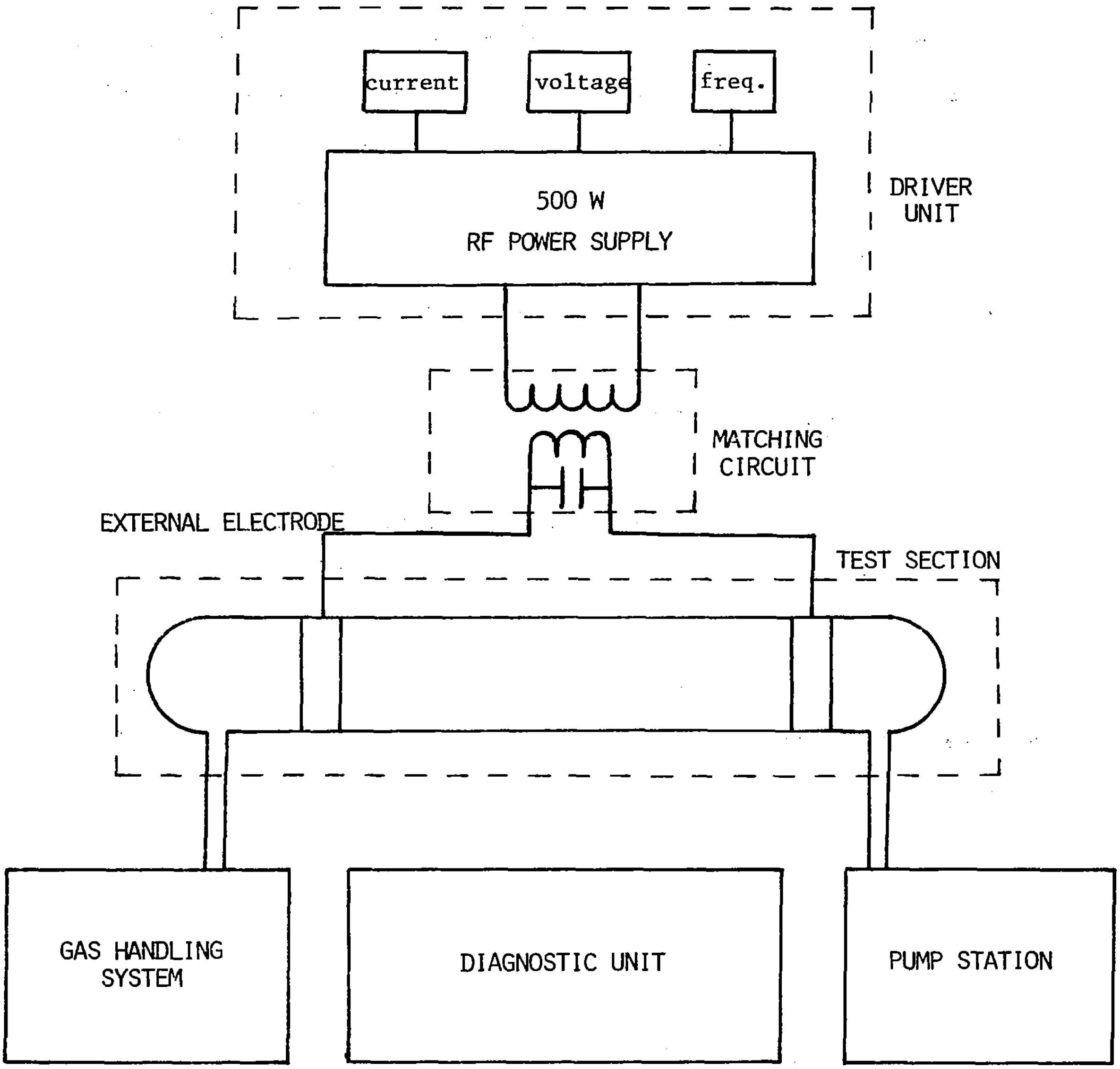

Fig. II.4. The ENRAD System

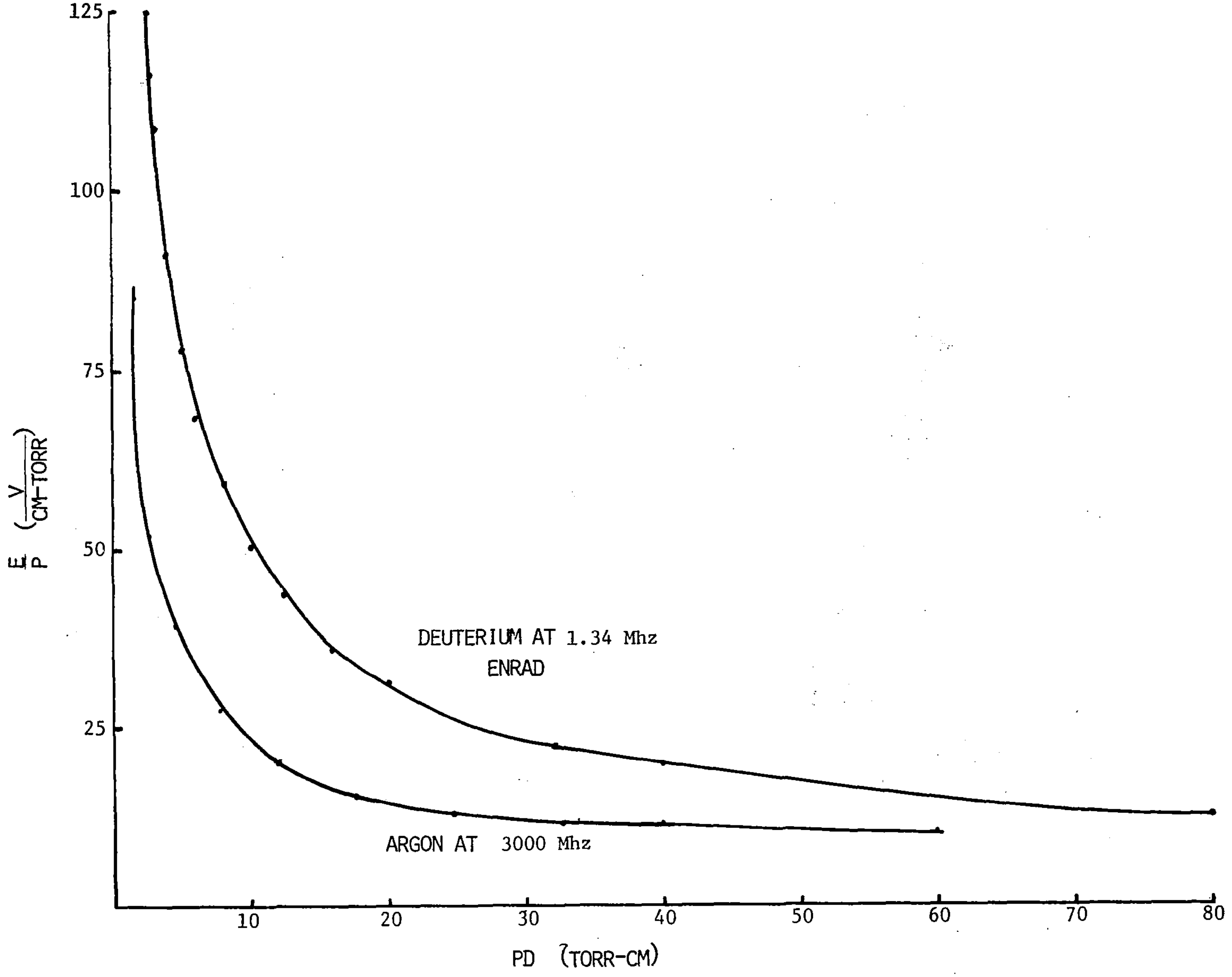

Fig. II-5. E/p vs pd for ENRAD at 1.34 Mhz

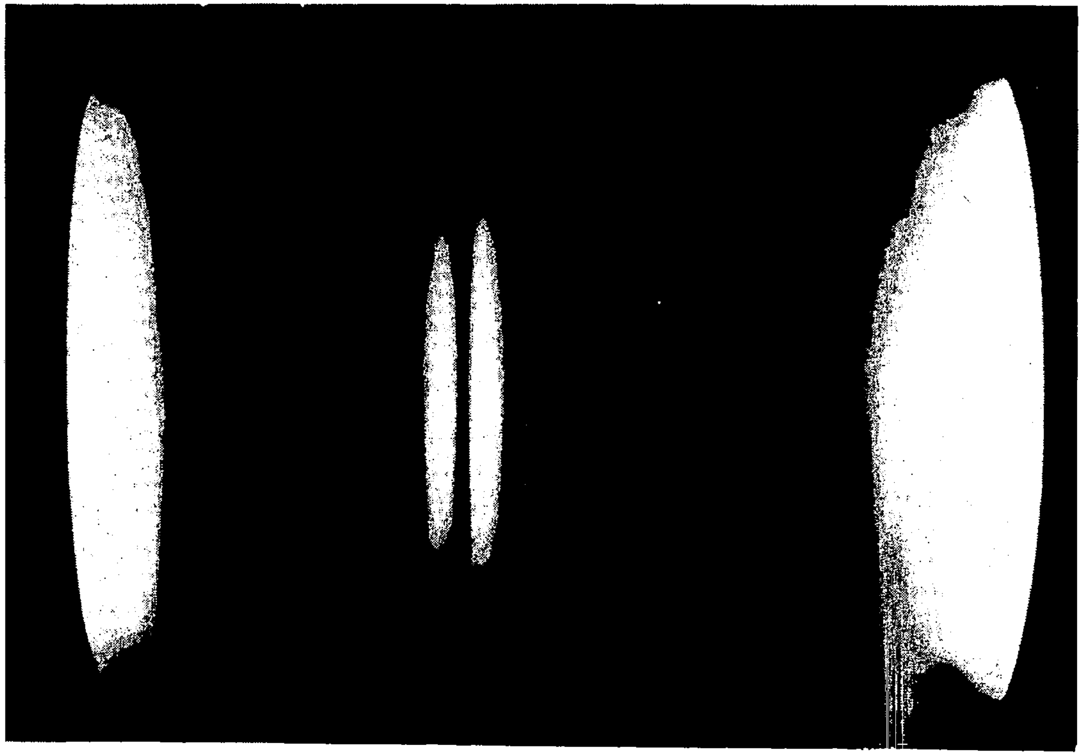

Fig. II-6. Typical pair of plasmoid disks in Hydrogen.

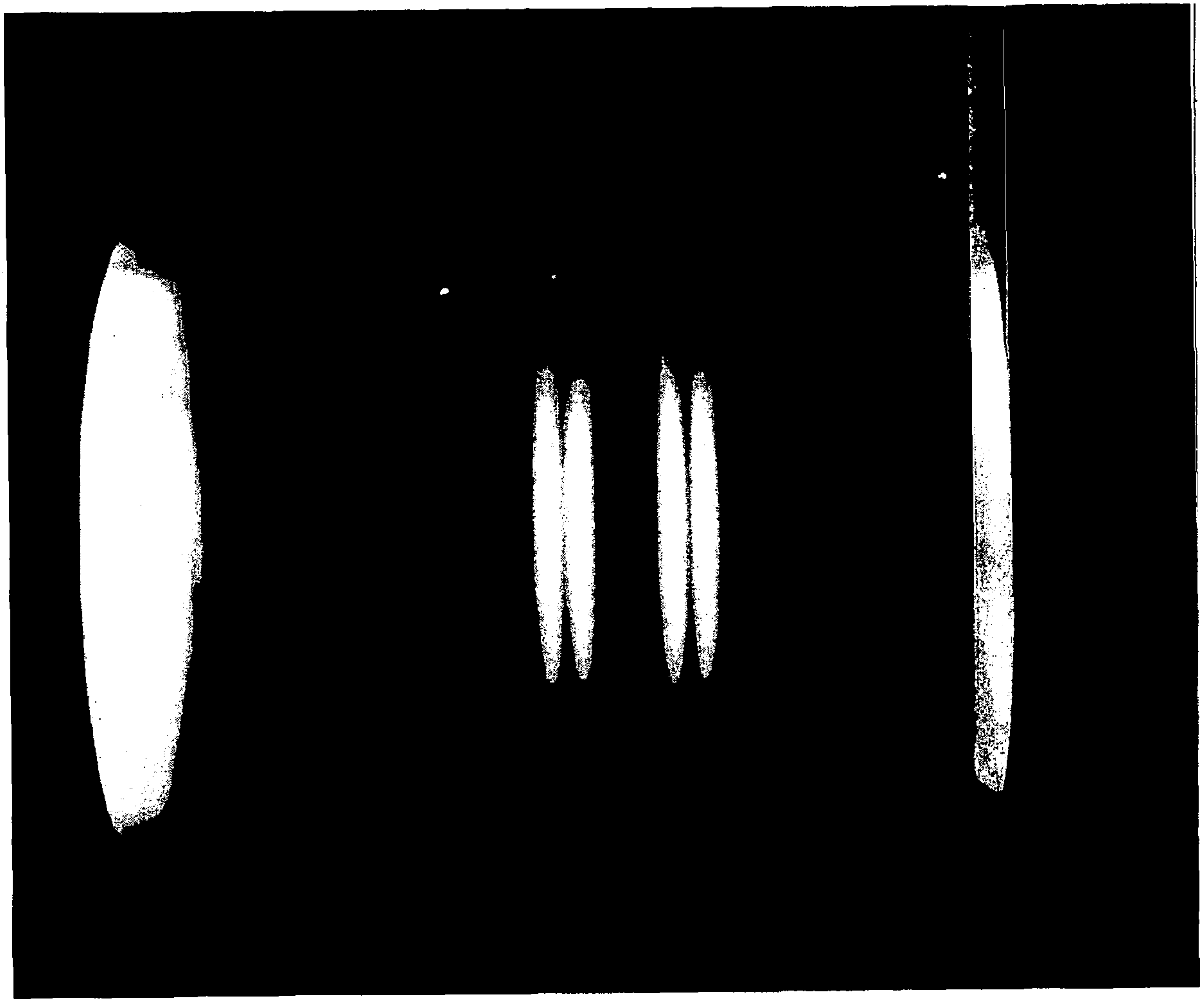

Fig. II-7. Two Pairs of Disks in Hydrogen.

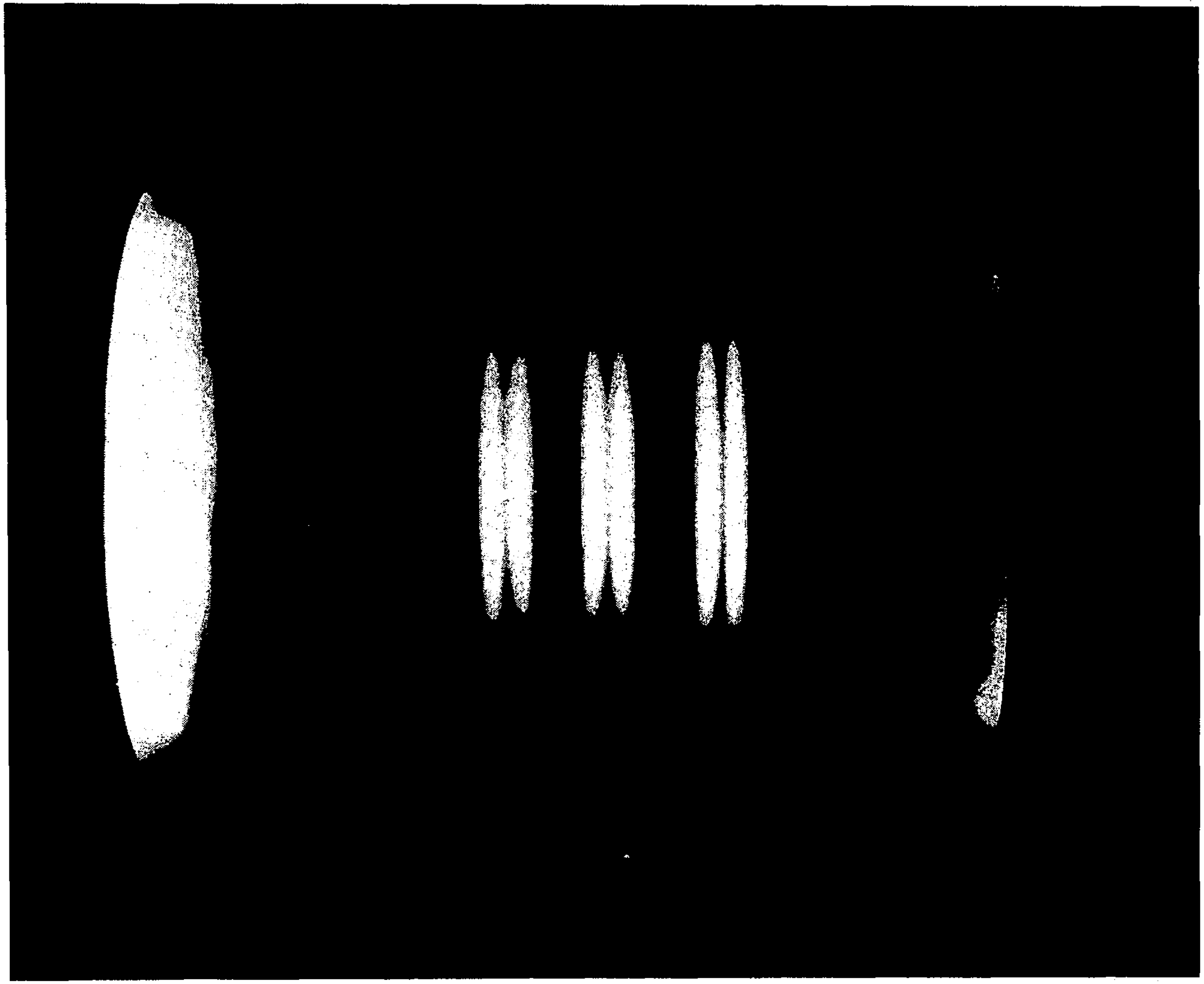

Fig. II-8. Three Pair of Disks in Hydrogen.

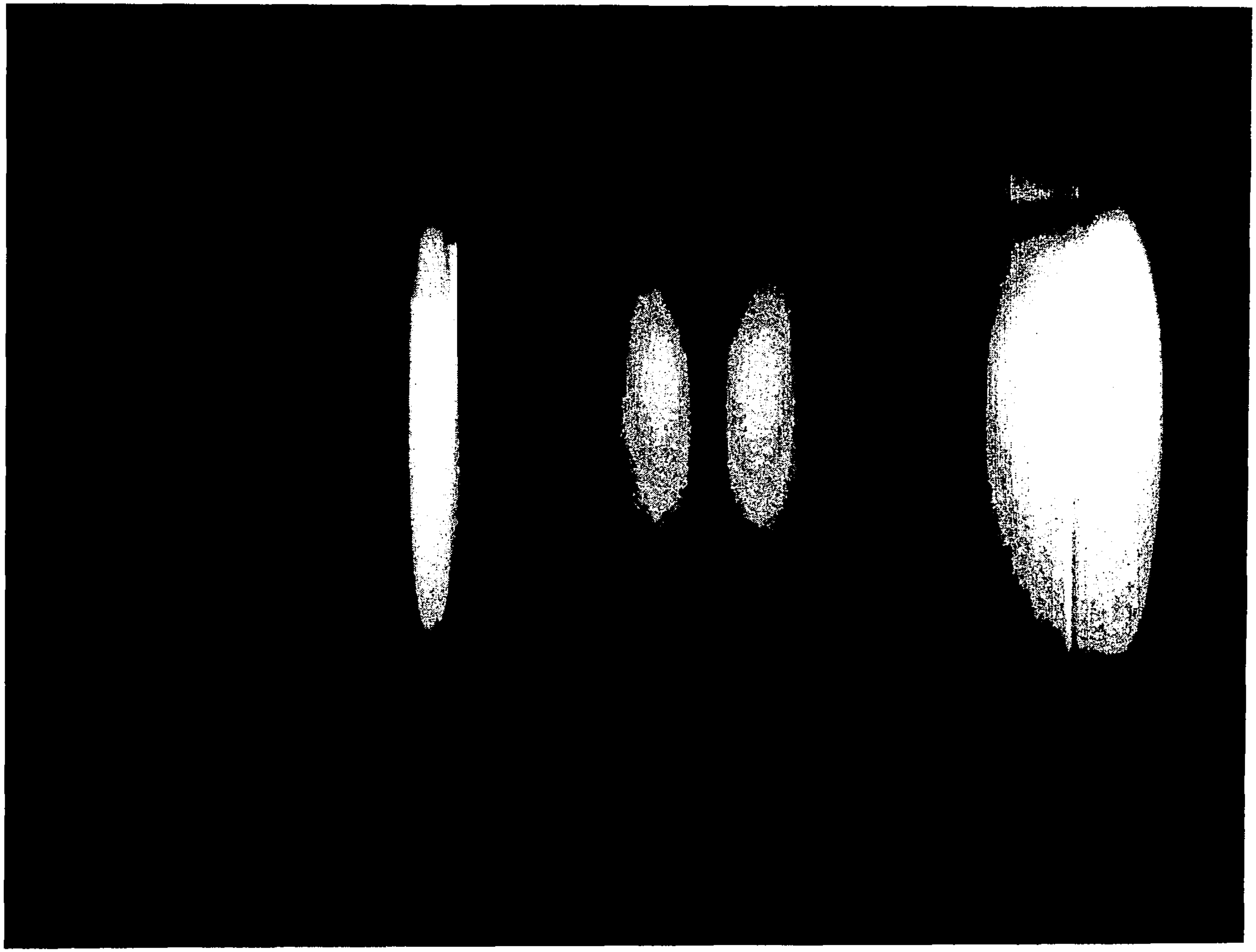

Fig. II-9. One Pair of Disks in Helium.

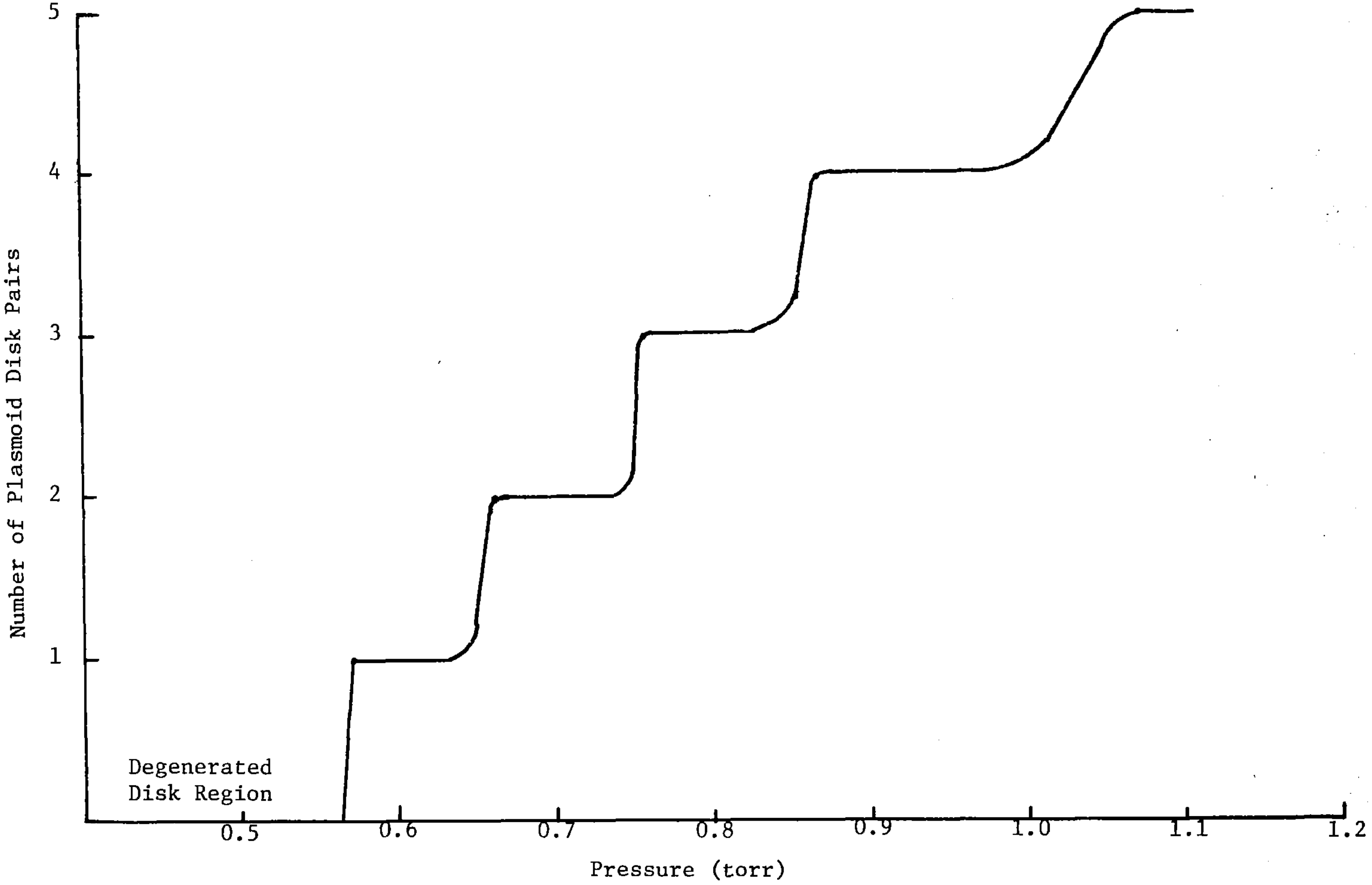

Fig. II-10. Number of disk pairs vs pressure for ENRAD device frequency, especially at larger pd values. It seems that after the cycle time is shorter than the effective recombination time or diffusion time (whichever is shorter), the plasma is stationary and an increase in the frequency has very little effect as far as maintenance of the discharge is concerned. (This is not to say that other properties such as neutron emission are independent of frequency.)

Once the discharge is ignited, particular E/p ratios will establish certain well defined visible plasma structures. These structures are pairs of disks in the following referrred to as "cavitons" which are separated by a very well defined dark space. (The separation appears black to the eye.) A pair of disks (a caviton) will exist over a certain pressure range (the applied voltage is kept constant) and if a certain critical pressure is exceeded, the plasma transforms (abruptly) into another mode consisting of 2n disks, or n cavitons where n is an integer. Again, each pair is separated by a very well defined dark space.

Figure II-6 shows such a caviton (n=1) while Figure II-7 and II-8 show two and three cavitons in deuterium. If helium is used, cavitons still can be obtained but are not as well defined as in deuterium or hydrogen. Figure II-9 shows such a caviton in helium. In any case the location of the cavitons is always symmetrical to the electrodes.

The cavitons should not be mistaken with the familiar striations (moving or stationary) of d-c or a-c discharges. The difference is that in these discharges the distance between striations changes when the pressure is changed; while for the cavitons described here the distances remain constant even if the pressure is changed until the critical pressure is reached where abruptly the next higher number of disk pairs is formed, having then different distances from each other. This relationship between pressure and number of disks can be seen in Figure II-10.

If the pressure is too low for formation of cavitons another phenomenon can be observed, which is referrred to as degenerated cavitons.

The cavitons are no longer suspended between the electrodes but are now attached to them. It appears that the one wall of the caviton is now a crescent, while the other wall is formed by the sharp edge of the electrode. Figure II-11 shows a photograph of such a degenerated caviton.

Since there is a minimum pressure for formation of regular cavitons, an obvious questions is--if there is also a minimum frequency? Therefore, the minimum frequency required to form a disk for a given pd-value was determined. In Figure II-12 this relationship is shown. The electrode distance (d) was varied while the pressure was kept constant ($p = 0.6$ torr). At any frequency below the straight line in Figure II-12, no cavitons will be formed, but a regular diffused discharge will appear. However, operation above the straight line will have little effect on the then established cavitons. This is confirmed up to 1.7 Mhz.

Another important piece of information relates to the question if the plasma remains in existence during the time when either voltage or current is zero. If the plasma should cease to exist at that time, restart of the discharge would be required each time. In this case, confinement of the plasma would not have been achieved.

Demonstration of a continuous plasma can be done by determining the relationship between light output, and electron density. The light output indicates the presence of excitation rather than ionization. However, lifetimes of excited states are typically 10^{-8} seconds, two orders of magnitude shorter than the cycle time. Therefore, if the electron density were to be lowered significantly or should totally disappear, light output would cease between cycles since electrons are undoubtedly responsible

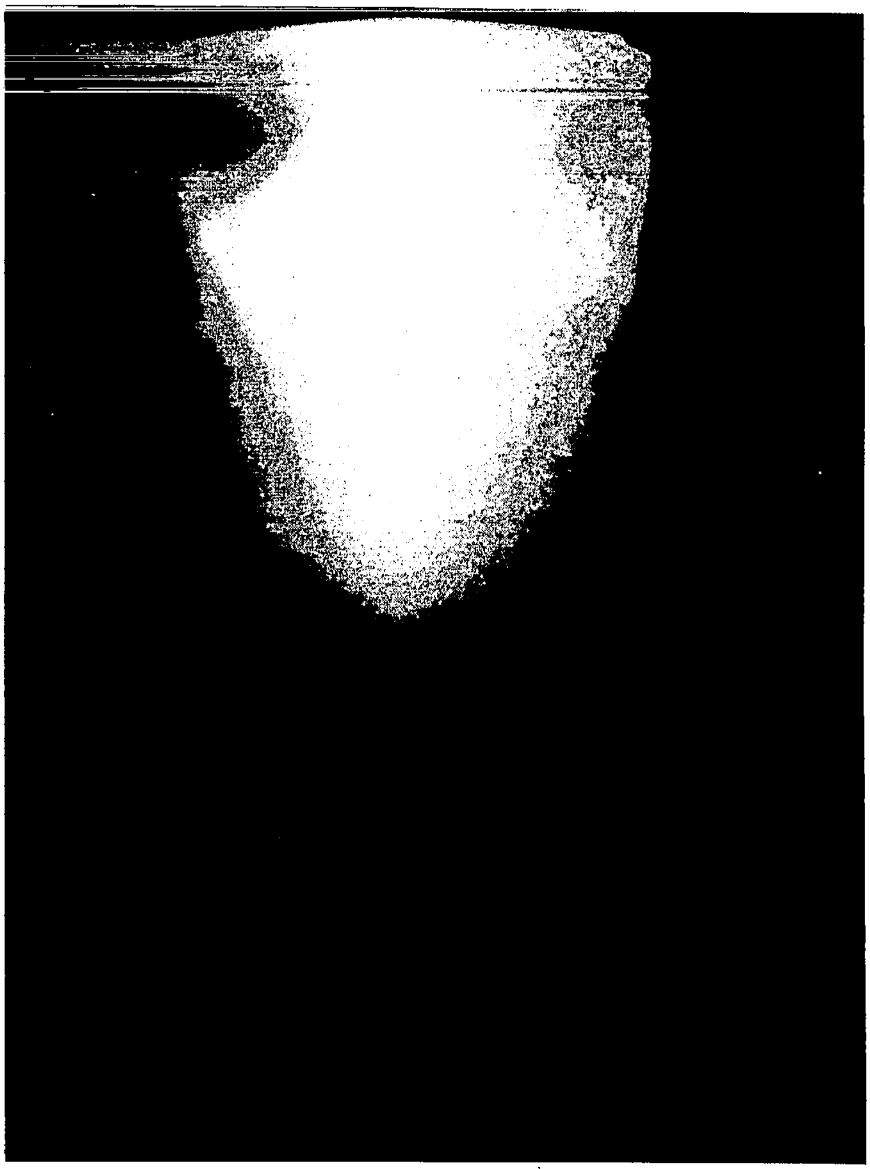

Fig. II-11. Degenerated Caviton.

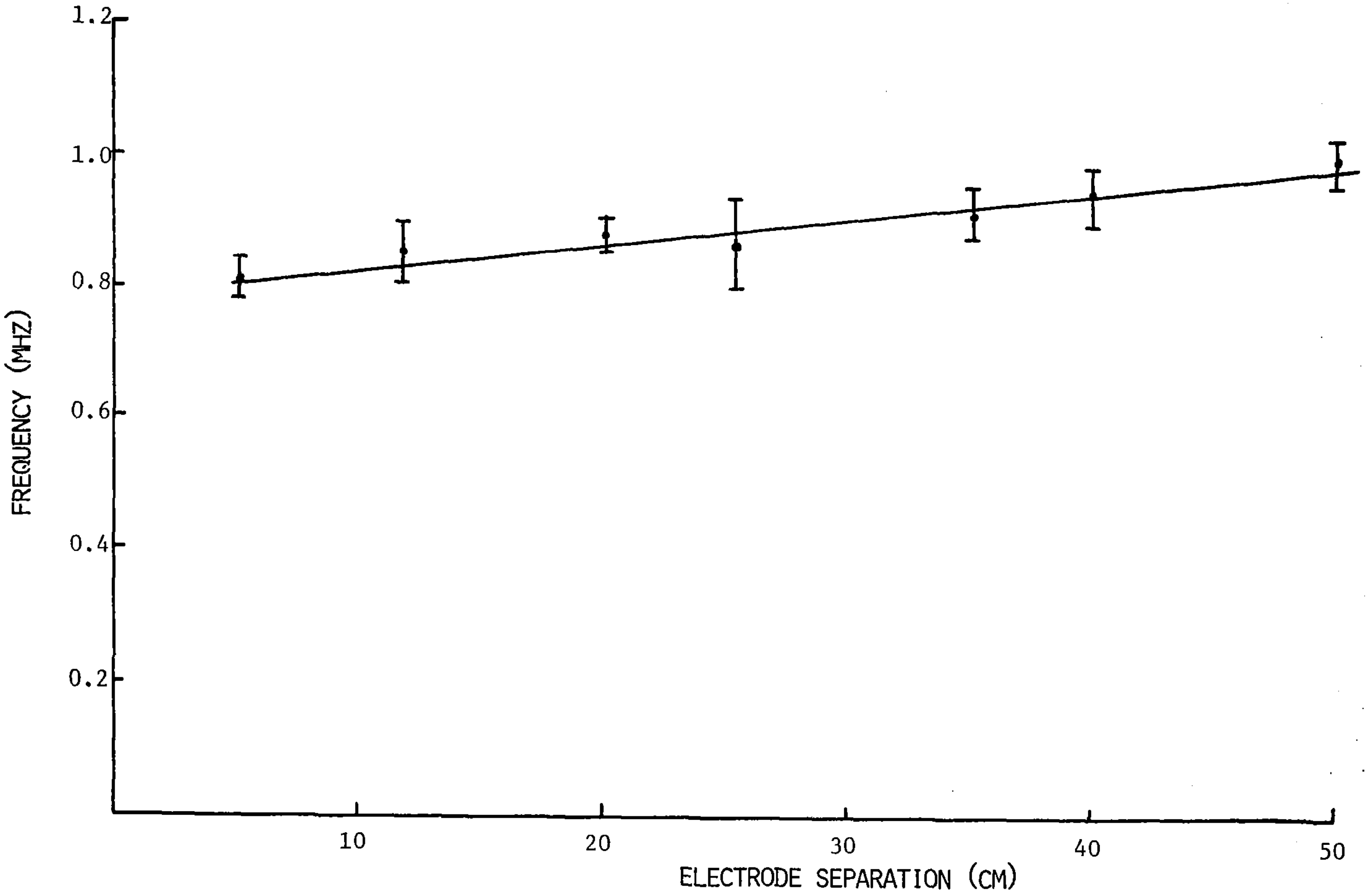

Fig. II-12. Electrode separation vs Plasma structure cut-off frequency for excitation of the atoms. Therefore, we believe that the intensity of the observed Balmer lines is a good indicator for the presence of electrons.

Figure II-13 shows a series of oscilloscope traces depicting total luminosity versus time for different operation conditions. Figure II-13a is the degenerated caviton mode. Here the lowest light output is observed. However, it is fairly constant with time, seemingly very well confined. (The signal is negative in all oscilloscope traces in Figure II-13.) When more cavitons are added, several types of oscillations can be observed. However, none of these oscillations have a frequency which is equal to or harmonic of the applied frequency. The time deflection on the oscilloscope traces is: 5 msec/cm. The conclusion which can be drawn from this figure is that the light intensity never equals zero, confirming that the plasma is in existence at all times.

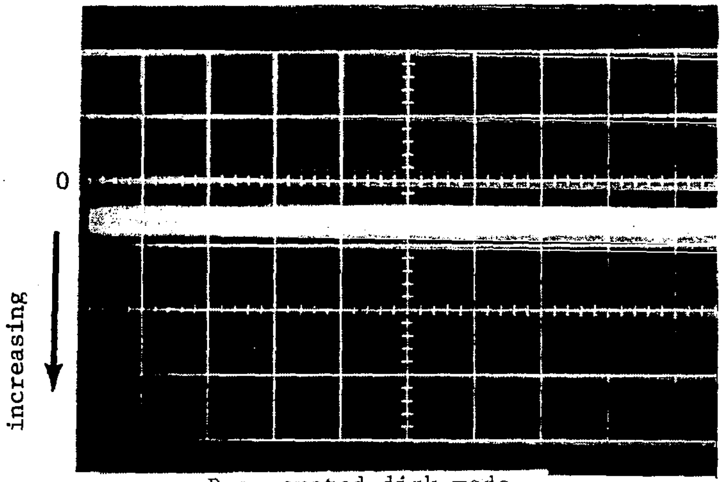

a. Degenerated disk mode.

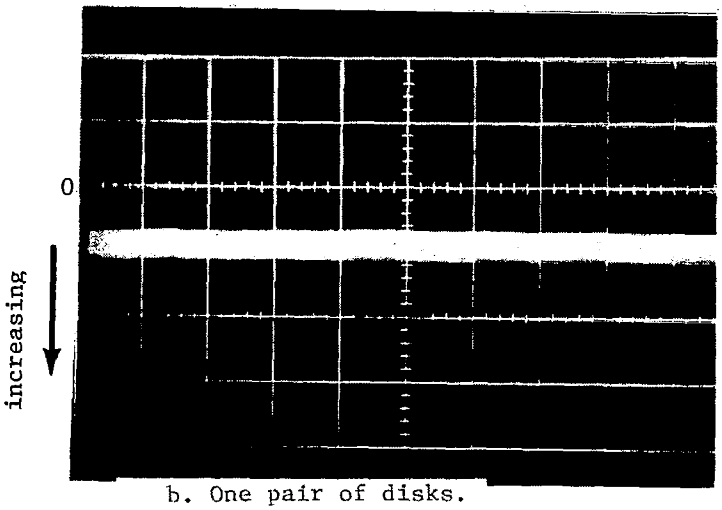

b. One pair of disks.

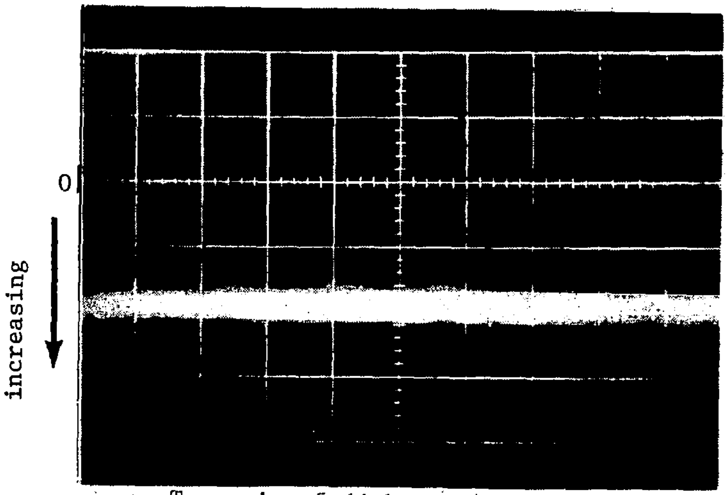

c. Two pair of disks.

Fig. II-13. Total Luminosity Output of ENRAD Device. Time Deflection 5 msec/cm.

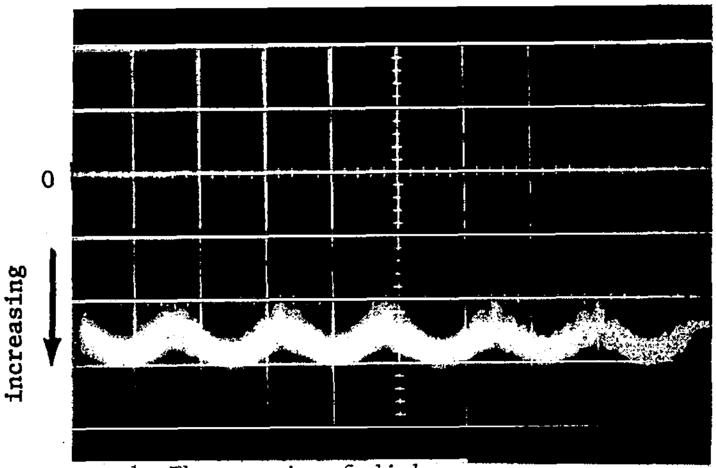

d. Three pair of disks

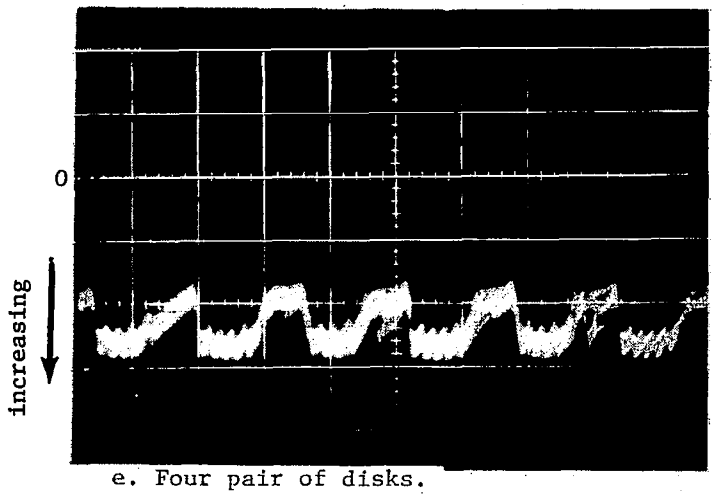

e. Four pair of disks.

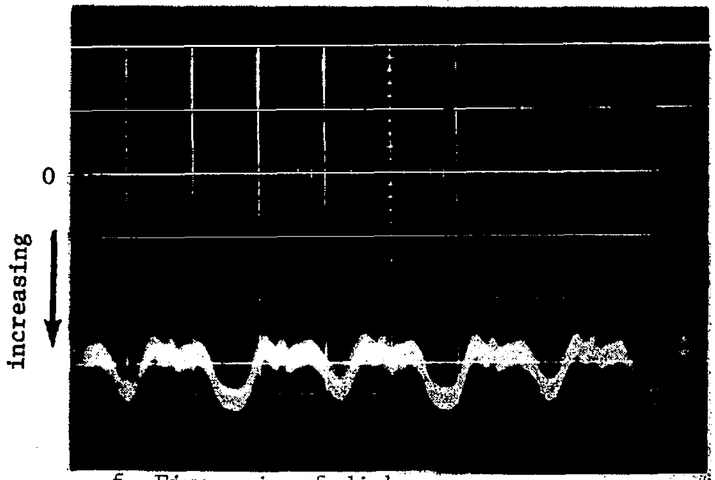

f. Five pair of disks.

Fig. II-13 Continued.

III. EXPERIMENTAL RESULTS

1. X-Ray Emission

In both discharges emission of x-rays took place. While this can be expected in the case of the high voltage discharge, it is not immediately evident that this would also happen in the case of the low voltage discharge.

The x-ray emission from the latter was, indeed, very weak and since, at the same time, neutrons were observed in the discharge, we cannot state beyond a reasonable doubt that the observed TLD readings and x-ray film exposures were actually caused by x-rays and not by a γ-background.

Since information on x-ray emission from the low-voltage discharge is so marginal, we will discuss first the x-ray emission from the high voltage discharge. Since the geometrical set up is very similar, it should give a good indication what kind of x-ray emission can be expected from a caviton forming electrodeless RF discharge.

a) The high voltage discharge is a strong source for x-ray radiation. This radiation seems to appear at or after the onset of the high frequency oscillations of the current and is, therefore, somewhat delayed in respect to the voltage pulse. This can be seen in Figure III-1 where the upper trace is the x-ray radiation and the lower trace is the applied voltage. This figure can be compared to Figure II-3 where the current trace can be found. Careful comparison shows that the x-ray radiation starts after the first full swing of the current oscillations.

The location of the x-ray emitting areas within the discharge tube was determined by wrapping a Kodak-Medical X-Ray Film enclosed in a light tight envelope around the discharge tube in the region between the electrodes. Figure III-2 shows the location where the film was placed, while

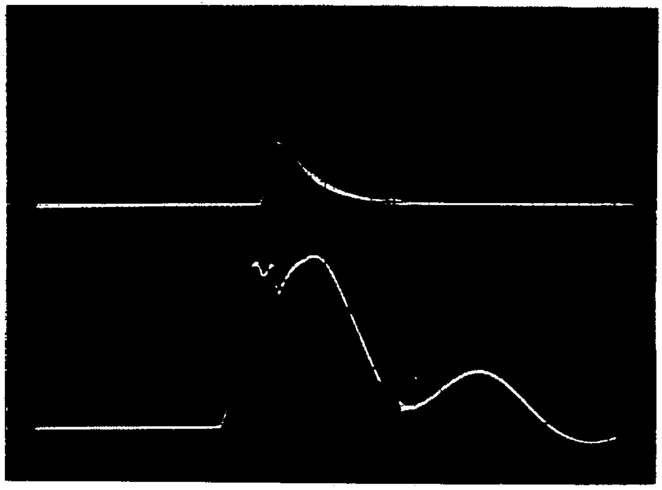

Figure III-1 Radiation and Voltage (common time base 2 μsec/cm)

Upper trace: Radiation
Lower trace: Voltage

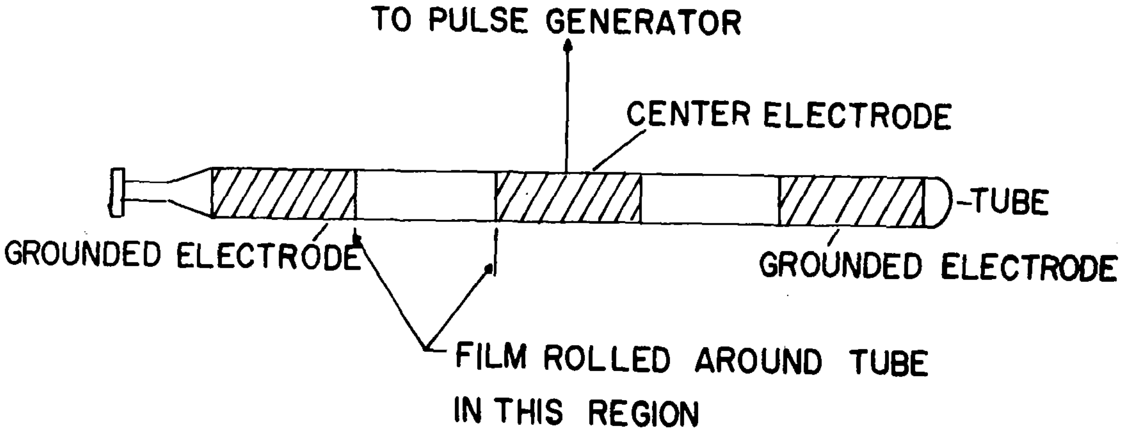

Figure III-2 Location of X-ray Film on Discharge Tube.

a more detailed sketch of the whole device, including its enclosure, can be found in an earlier figure (Fig. II-2). The results (positive) of the wrap around is shown in Figure III-3. The most interesting features are the crescent shaped exposure patterns and the sharp transition from exposed to unexposed areas, although the long side bars are also a phenomenon which needs to be explained. In Figure III-3 some of the crescents overlap, since the x-ray film overlapped when it was placed. Therefore, a positive of the x-ray negative, namely the one shown in Figure III-3, was rolled up and glued together. The unexposed part was cut away. Figure III-4 then shows a photograph of this composite. As one can see there are 3 symmetrically aligned crescents, quite similar in appearance as the one shown in Figure II-11, although the latter figure is a photograph of the visible glow of the low voltage discharge.

The pulsed high voltage discharge has a feature which the low voltage RF discharge does not have. Namely, since a dc voltage pulse, which is applied, can run the ungrounded electrode either positive or negative. As it turns out, this makes a difference as far as x-ray production is concerned. To show this the x-ray radiation was observed side on using a collimator and scintillation detector. Figure III-5 shows the general outlay of the discharge tube, the shielding enclosure and the location of the detector. Scans parallel to the axis of the discharge tube were made and it was found that the maximum radiation emissions occur close to the negative electrode, which is also the electrode where the crescents were observed. Figure III-6 shows the scan with the center electrode negative, while Figure III-7 shows the scan with the center electrode positive, which means the grounded electrode is negative. As can be seen, the radiation maximum is always toward the negative electrode. Its loca-

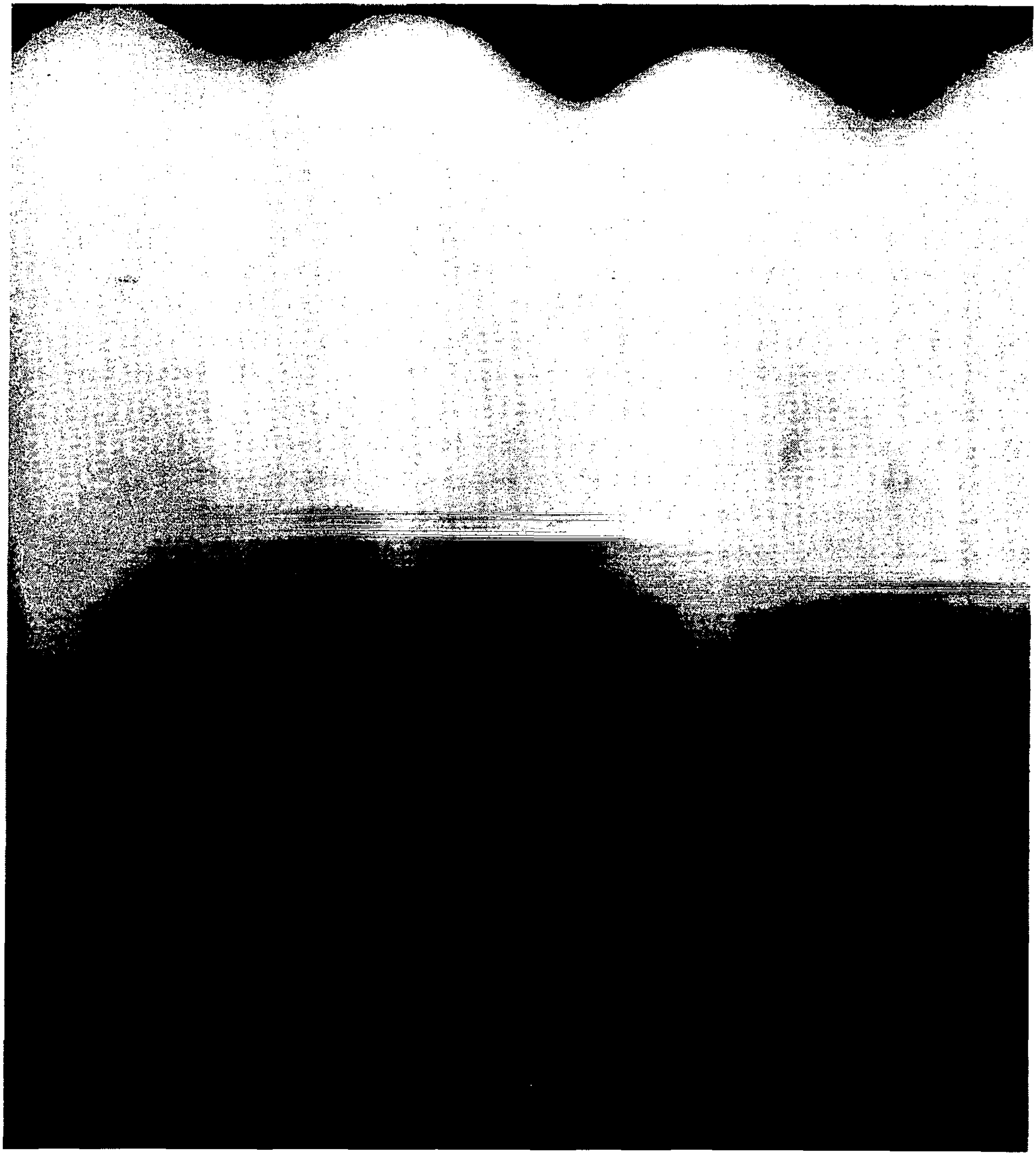

Fig. III-3. Wrap around x-ray from older ENRAD like device.

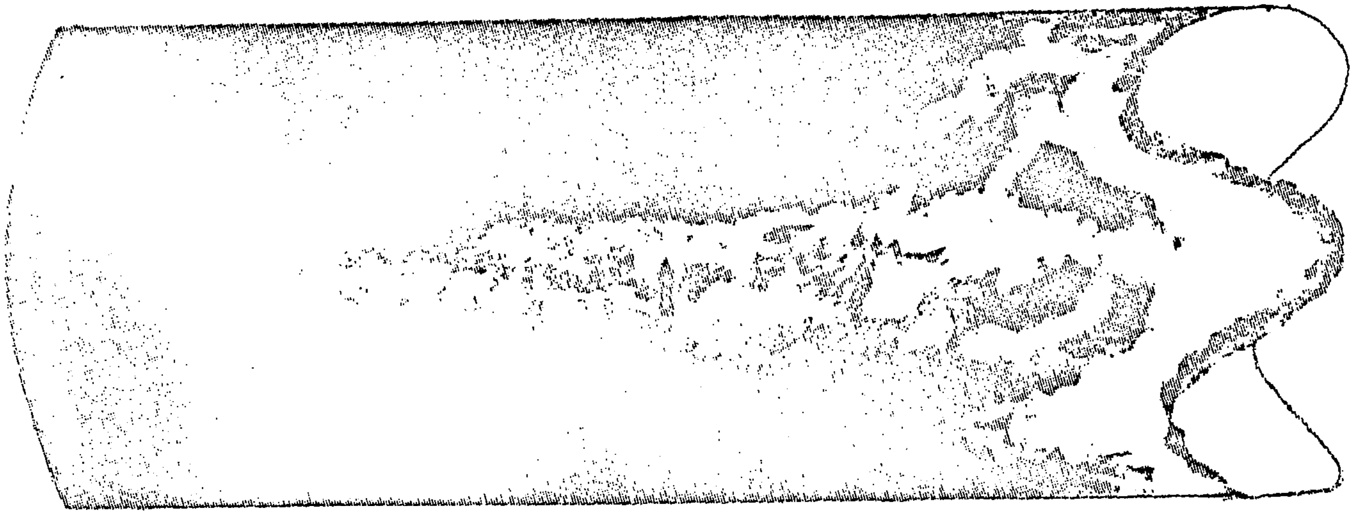

Fig. III-4. Three Dimensional Sketch of X-Ray Pattern Around Tube.

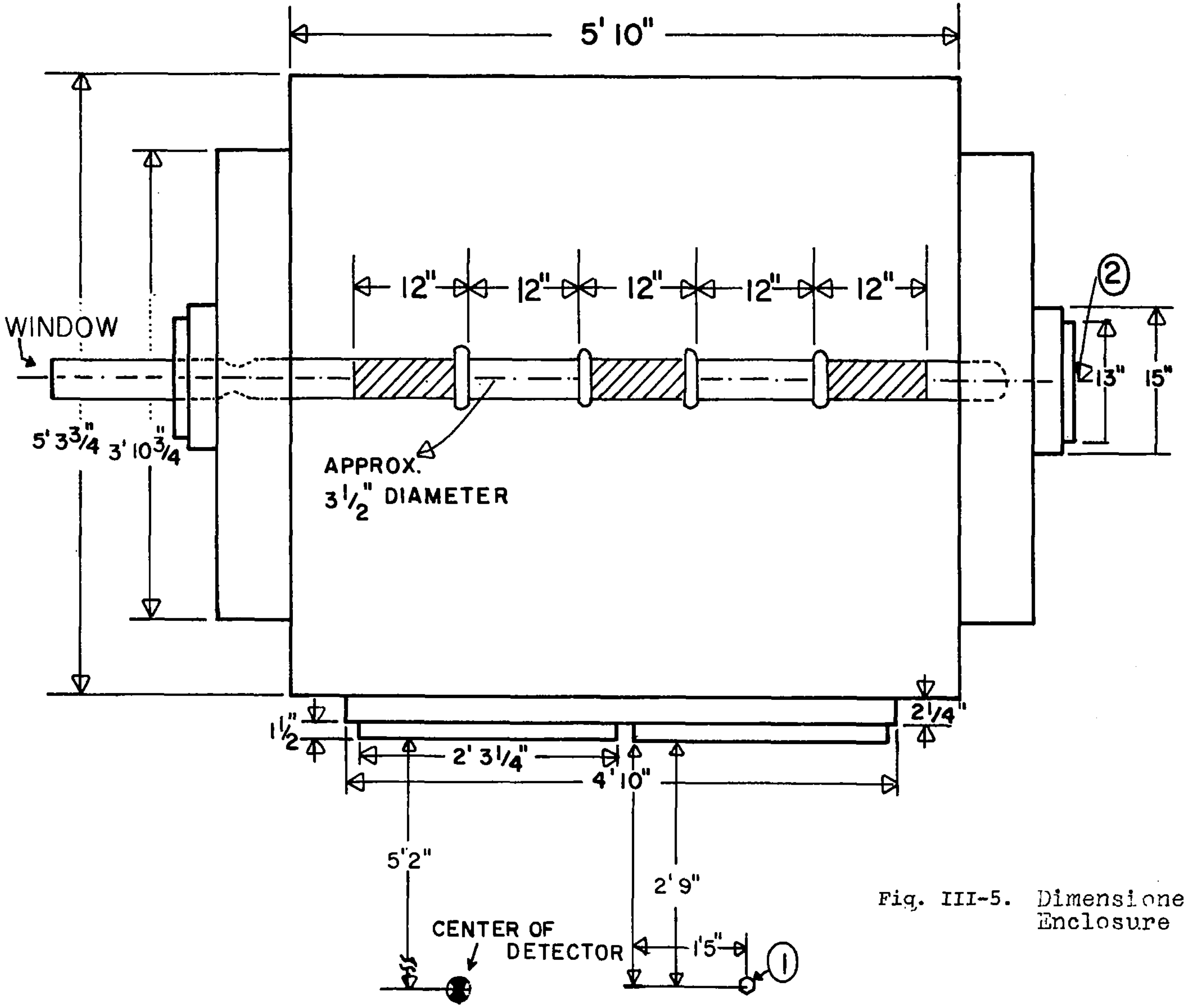

Fig. III-5. Dimensioned Tube Enclosure

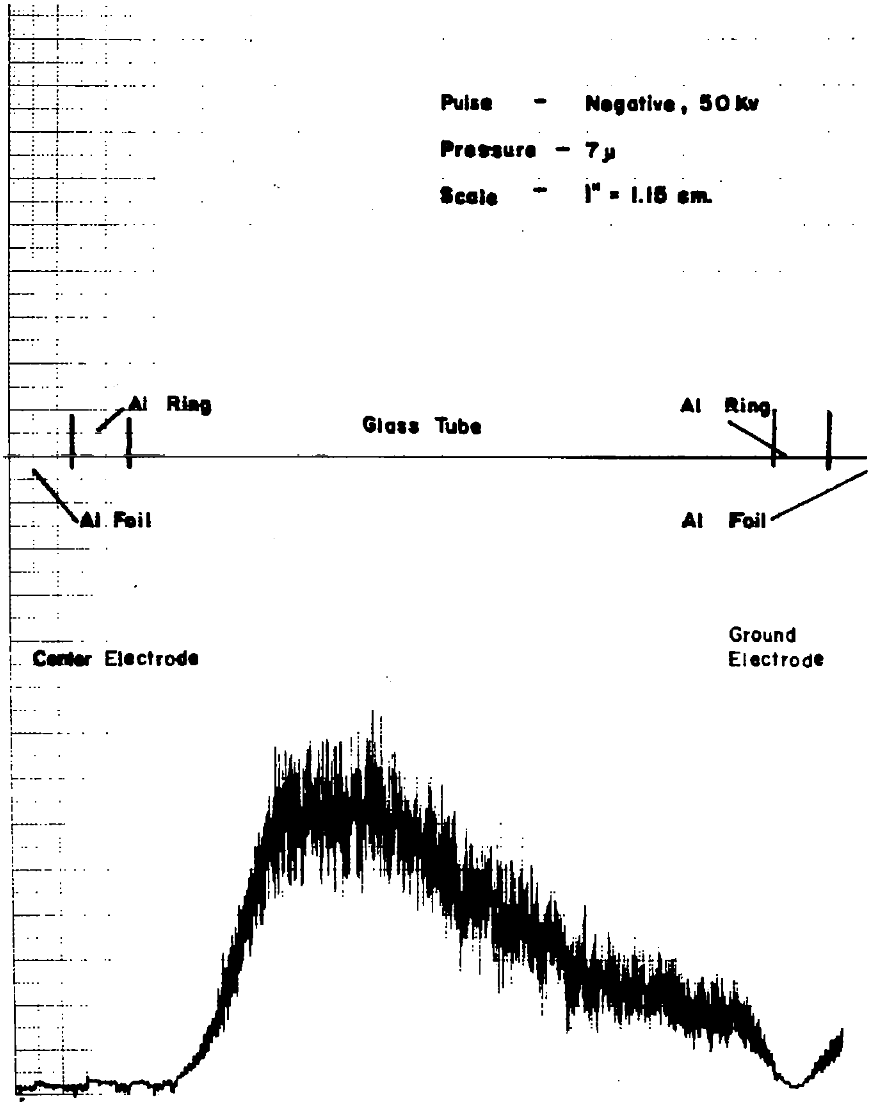

Fig. III-6. X-ray Output Along Tube Axis Center Electrode Negative.

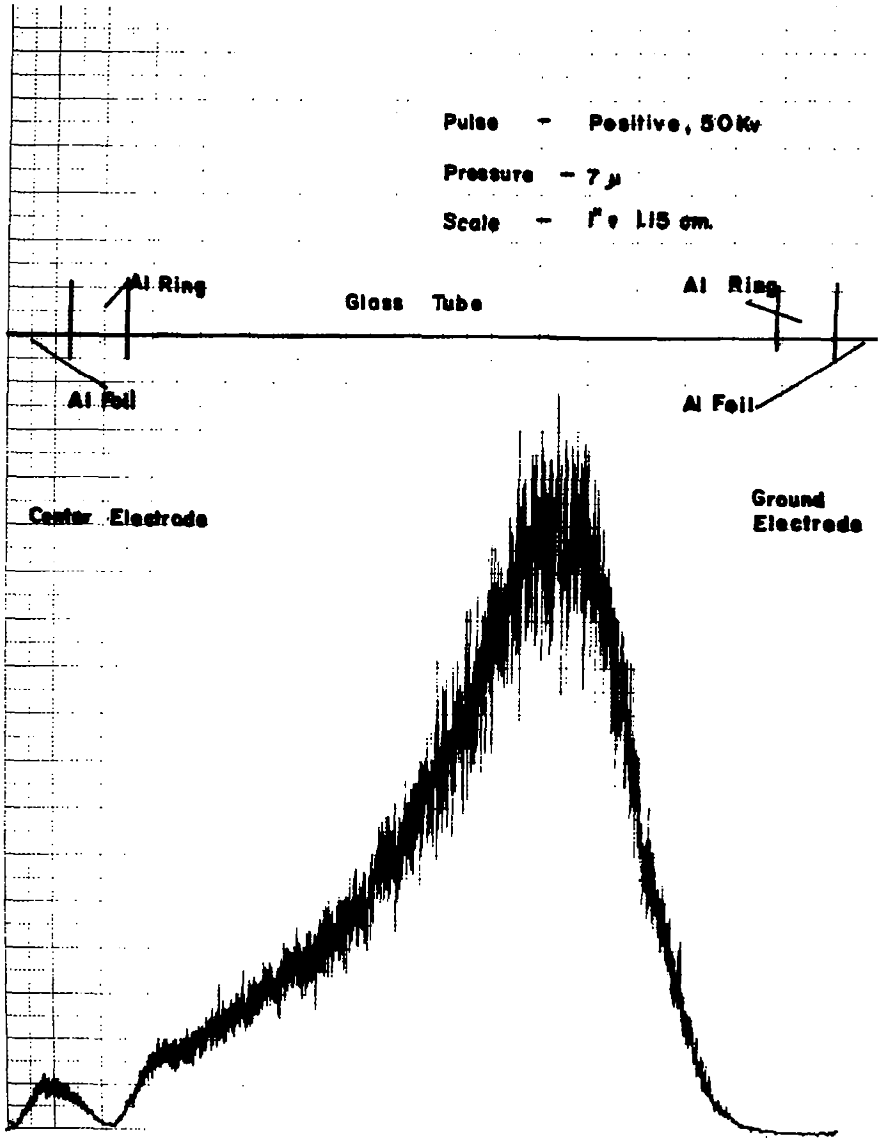

Fig. III-7. X-ray Output Along Tube
Axis Center Electrode Positive.

tion is at a certain distance (d) away from the negative electrode. This distance is a function of pressure, as shown in Figure III-8. The higher the pressure, the closer it is to the negative electrode. Observations of the x-ray emission were also made end-on and typical x-ray positives obtained are shown in Figure III-9. The x-ray films were placed on the tube x-axis 1, 3 and 5 feet away from the window. The exposure which shows an intense inner core was 1 foot away while the ones which show an unexposed inner core were further away. If one would assume that the x-rays come from a layer on the inner surface of the tube (or from the crescents close to the inner surface of the tube), one can explain Figure III-9. This is done in Figure III-10 and Figure III-11. The distance of the x-ray film is plotted here in feet, in axial direction while the size of the pattern is plotted in mm in radial direction. In this way one can triangulate back to the x-ray emitting layer. The location of this layer agrees with the side on scans of Figure III-6 and III-7. Its structure, of course, can be seen from the wrap-around in Figure III-3.

Of course, if an agreement with the side on scans exists then also a switch in polarity must show up in the end-on x-rays. This is, indeed, the case and the difference can be seen by comparing Figure III-6 to III-7. Indeed, the x-ray emission is moved closer to the negative electrode.

B. X-ray Emission from the Low Voltage H-F Discharge

Since the x-ray emission from this discharge is considerably reduced in intensity, no clear determination of its structure could be made. However, from the above described results, one can roughly estimate the shape and structure of the expected x-ray exposures.

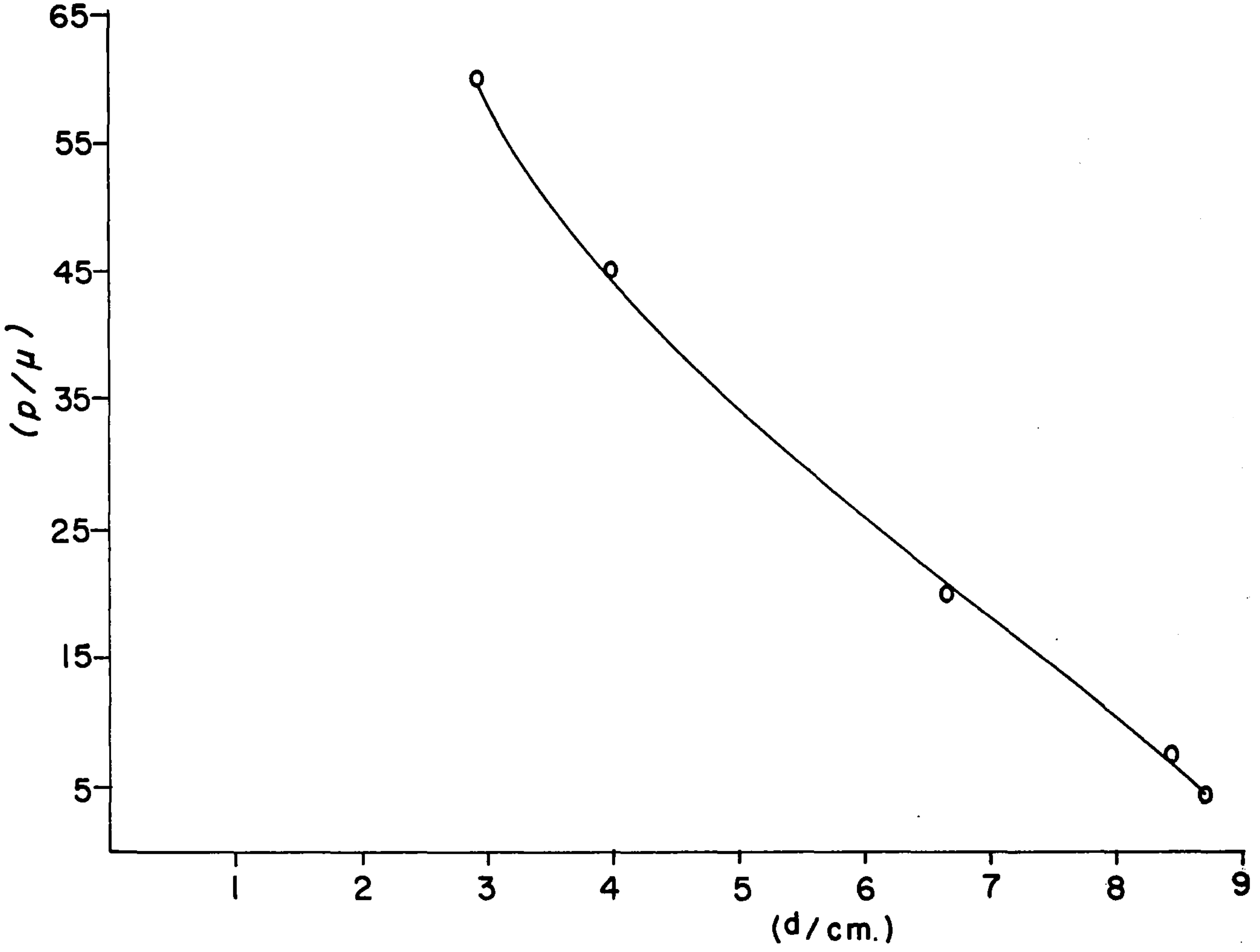

Fig. III-8. Relation between Pressure p and Distance d from Negative Electrode to Position of Maximum X- Radiation

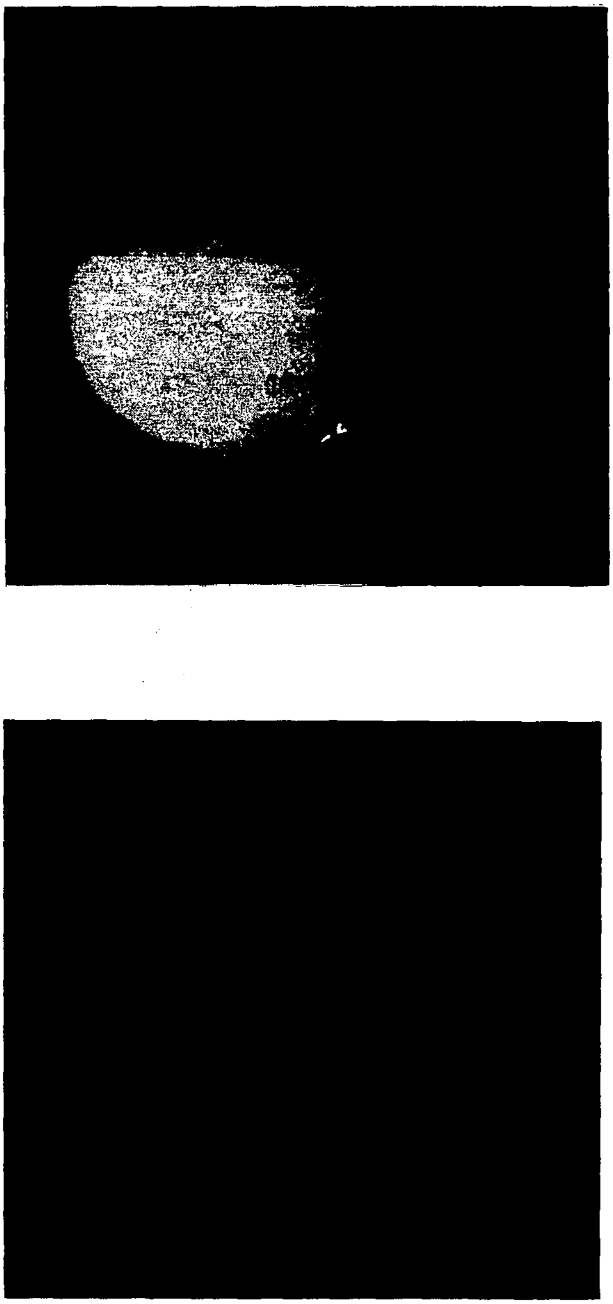

Fig. III-9. End View X-Rays from Older ENRAD-like Device.

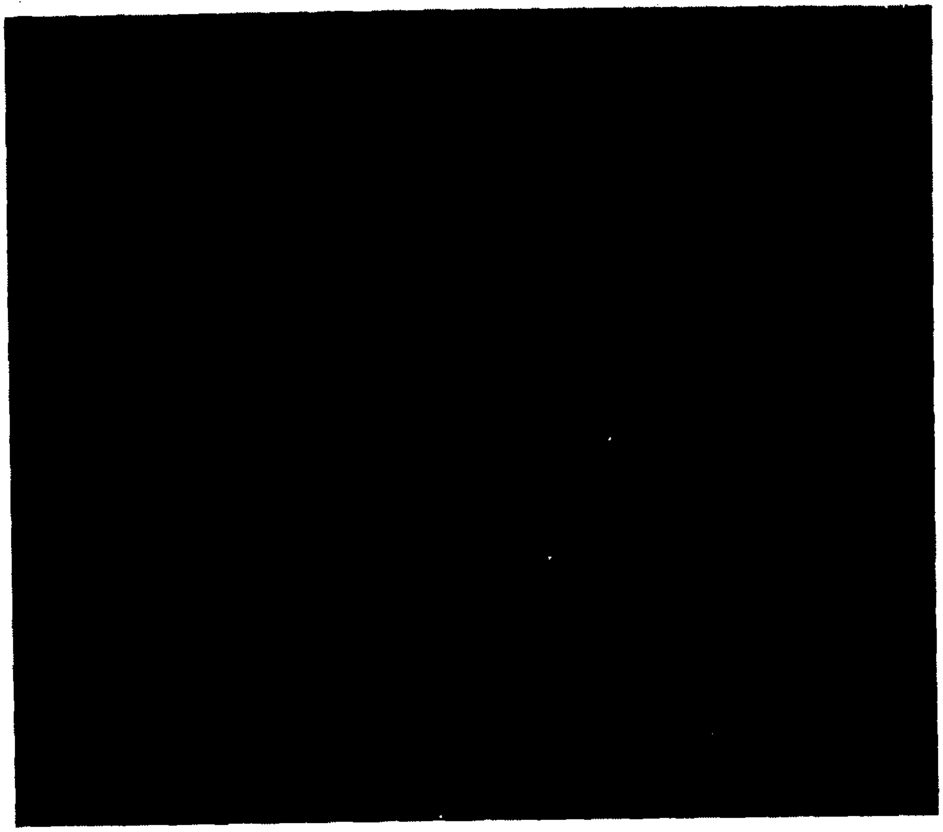

Fig. III-9. Cont. Shows a Shadowgraph of a Film Holder.

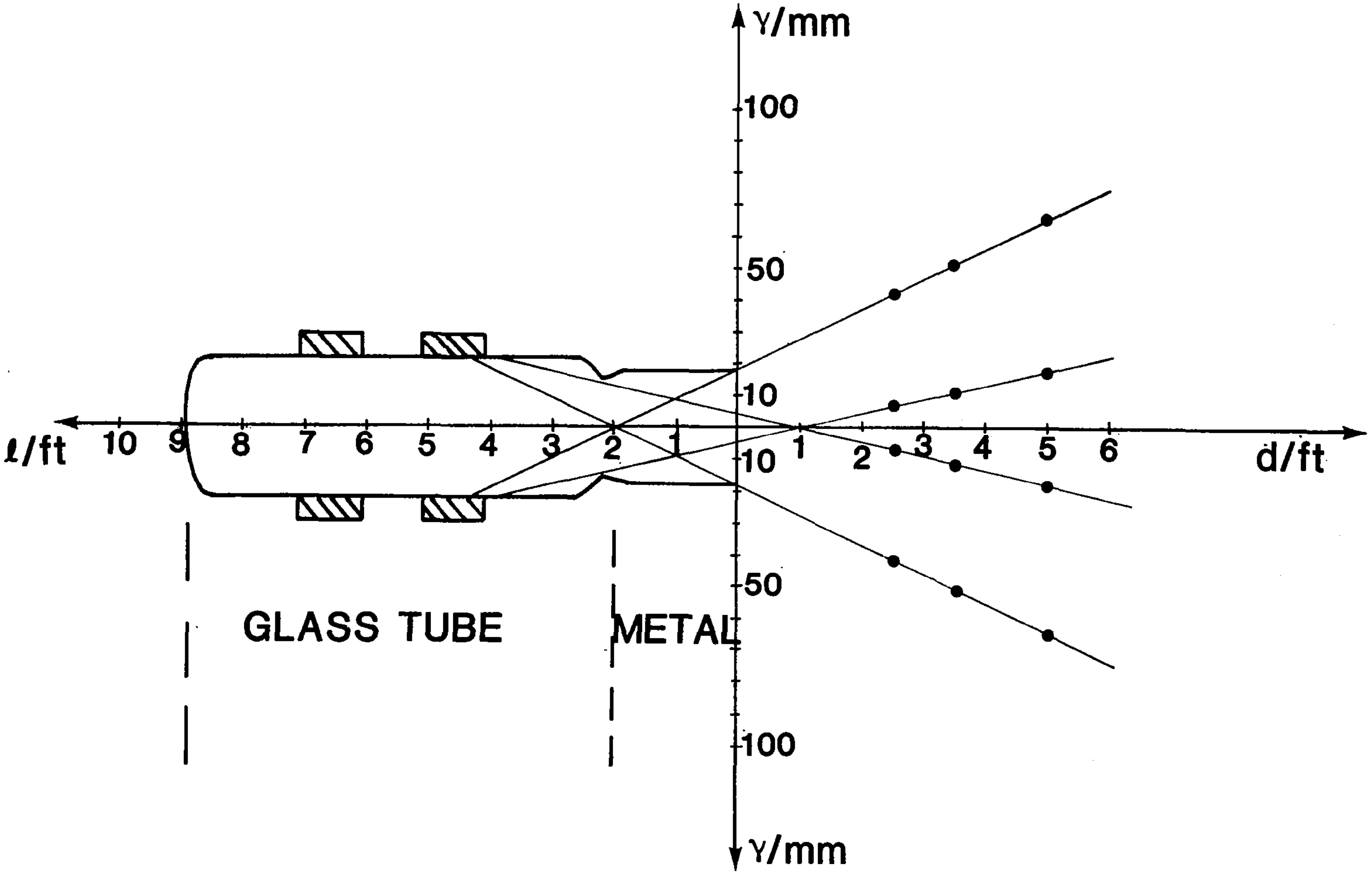

Figure III-10 X-ray Geometrie (50 kV pos. pulse polarity at 7 μ pressure)

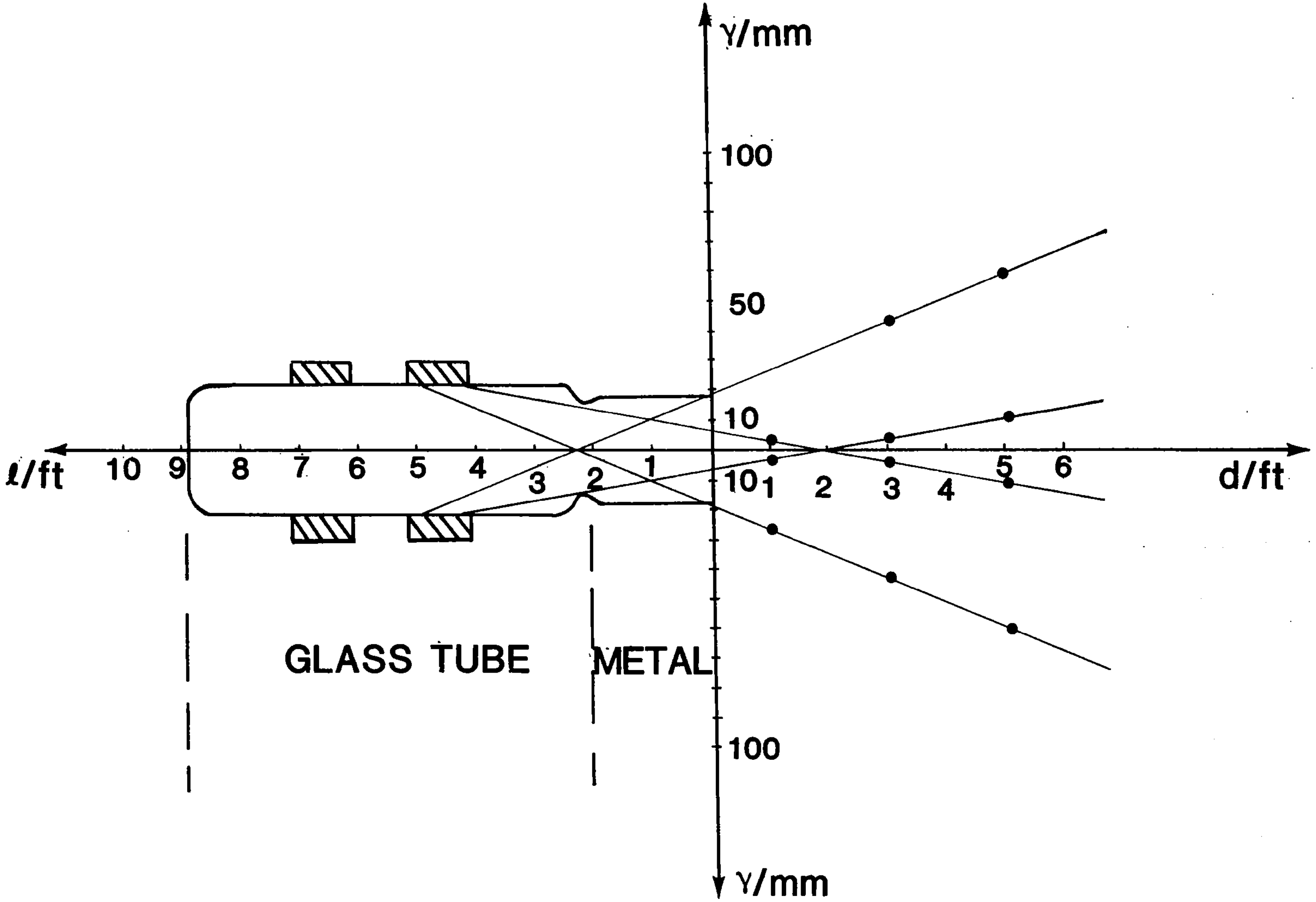

Figure III-11 X-ray Geometrie (50 kV neg. pulse polarity at 7μ pressure)

Since x-ray films are a good dielectric, it was not possible to wrap the discharge tube. The RF would heat the x-ray film and melt it. Therefore, a film was placed next to the tube (parallel to the tube axis) without bending it about 1 cm away from the surface of the tube. The resultant exposure (negative) is shown in Figure III-12 which has to be compared to the wrap-around (Figure III-3). Since the exposure is very faint, only superficial conclusions can be drawn. Figure III-12 was taken with a caviton in the center of the discharge tube. There is, indeed, a region of increased x-ray emission in the center of Figure III-12. The other two maxima at the electrode must correspond to the (smaller) maxima on the positive electrode, which appear in FiguresIII-6 and III-7.

For the end-on exposures, one would not expect a pattern as in Figure III-9, since the discharge tube was all glass and did not have the stainless steel neck which was responsible for the inner core and outer zone definition, as seen in Figure III-9. Therefore, one really could only expect a diffuse disk at best or just a general fog if the radiation is isotrop. In contrast to this expectation, the exposures shown in Figures III-13 through III-17 show a distinct structure. There is, indeed, a central blob which could be caused by a collimated beam in Figure III-13. The exposures are--as can be seen--reproducible only to some degree, they vary in intensity and location. Also the streaks intersecting the crescent in Figure III-15 vary from exposure to exposure. The small crescent of Figure III-14 may correspond to the most heavily exposed portion of the blob of Figure III-13. The fact that there are two crescents on Figure III-16 is understandable, since these are long range exposures (usually 8 hrs.) and the discharge may have been turned off once and restarted or the pressure may have changed. This may cause the beam to deviate somewhat and so cause the double exposure.

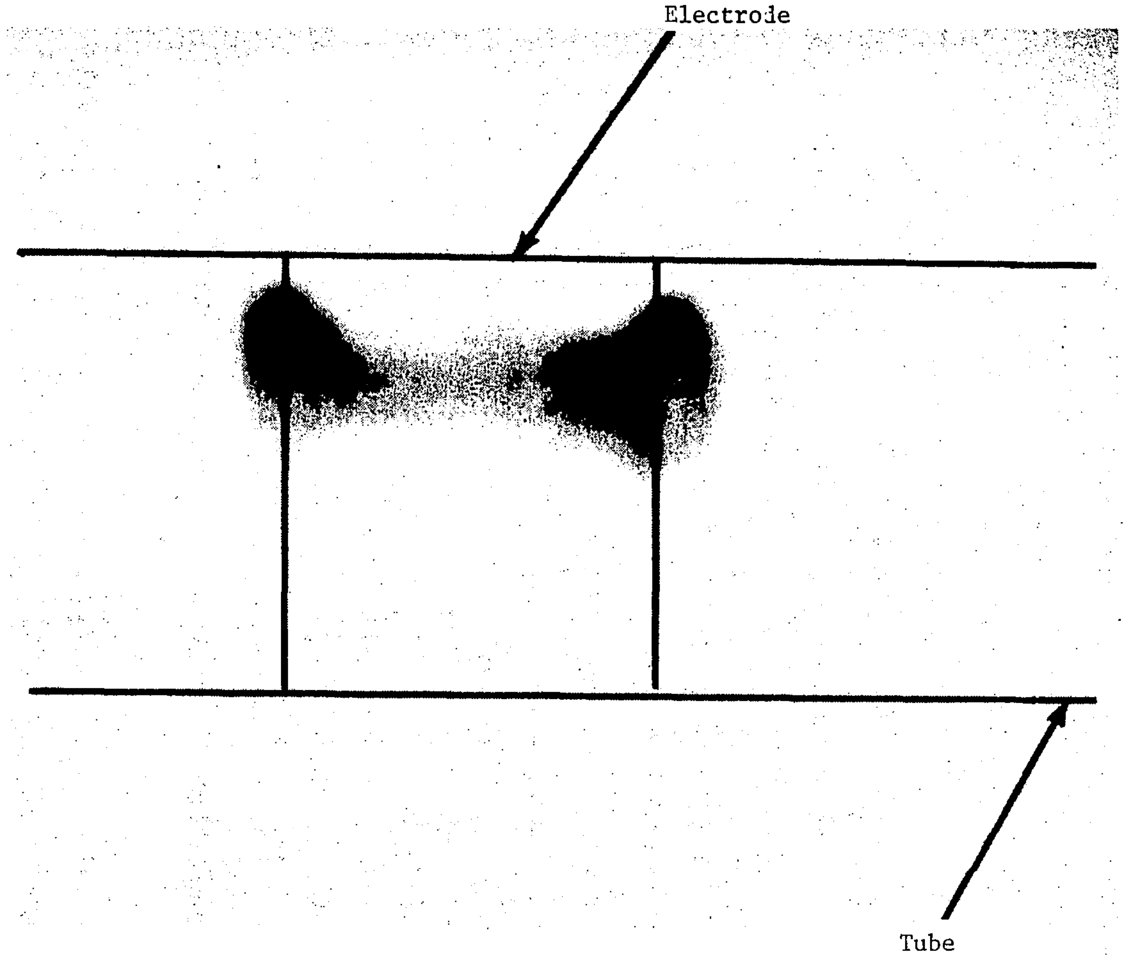

Figure III-12 X-ray from electrode region of ENRAD device.

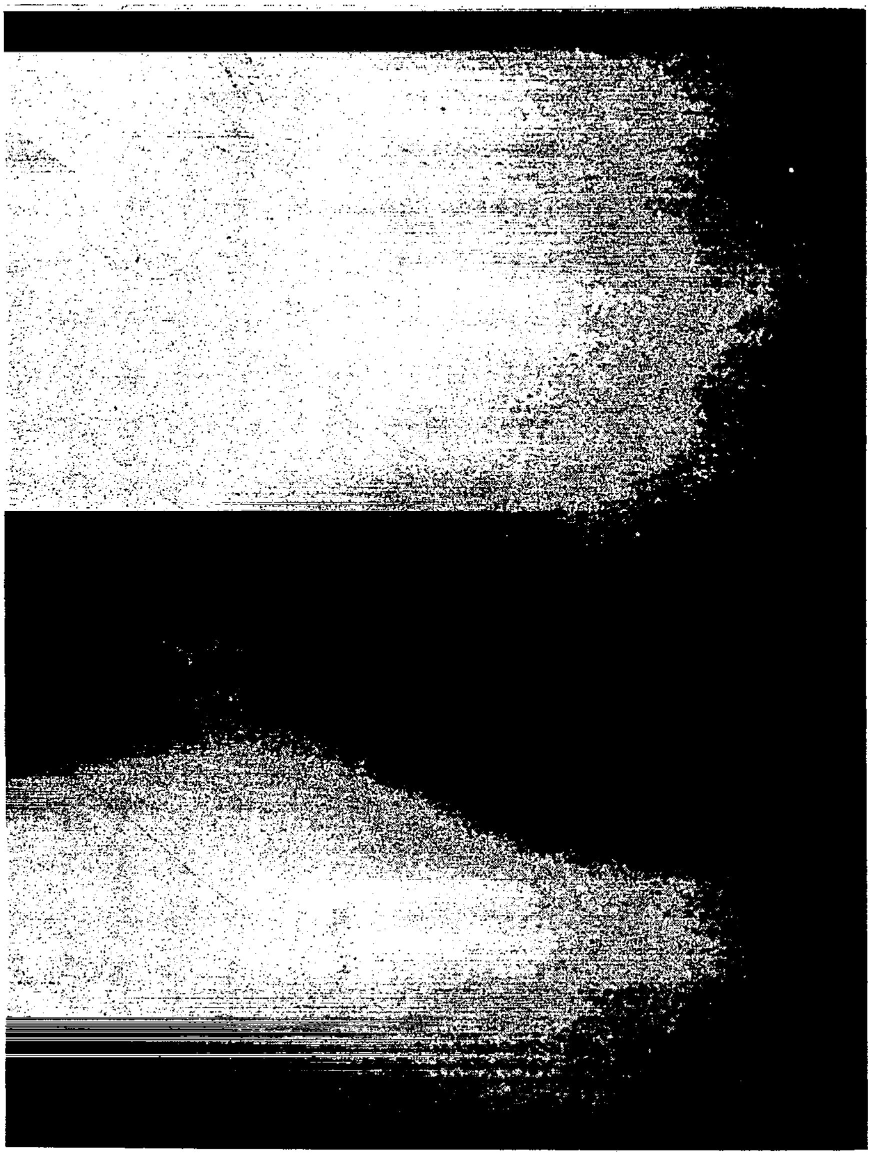

Figure III-13. End-on X-ray Output from RF Discharge.

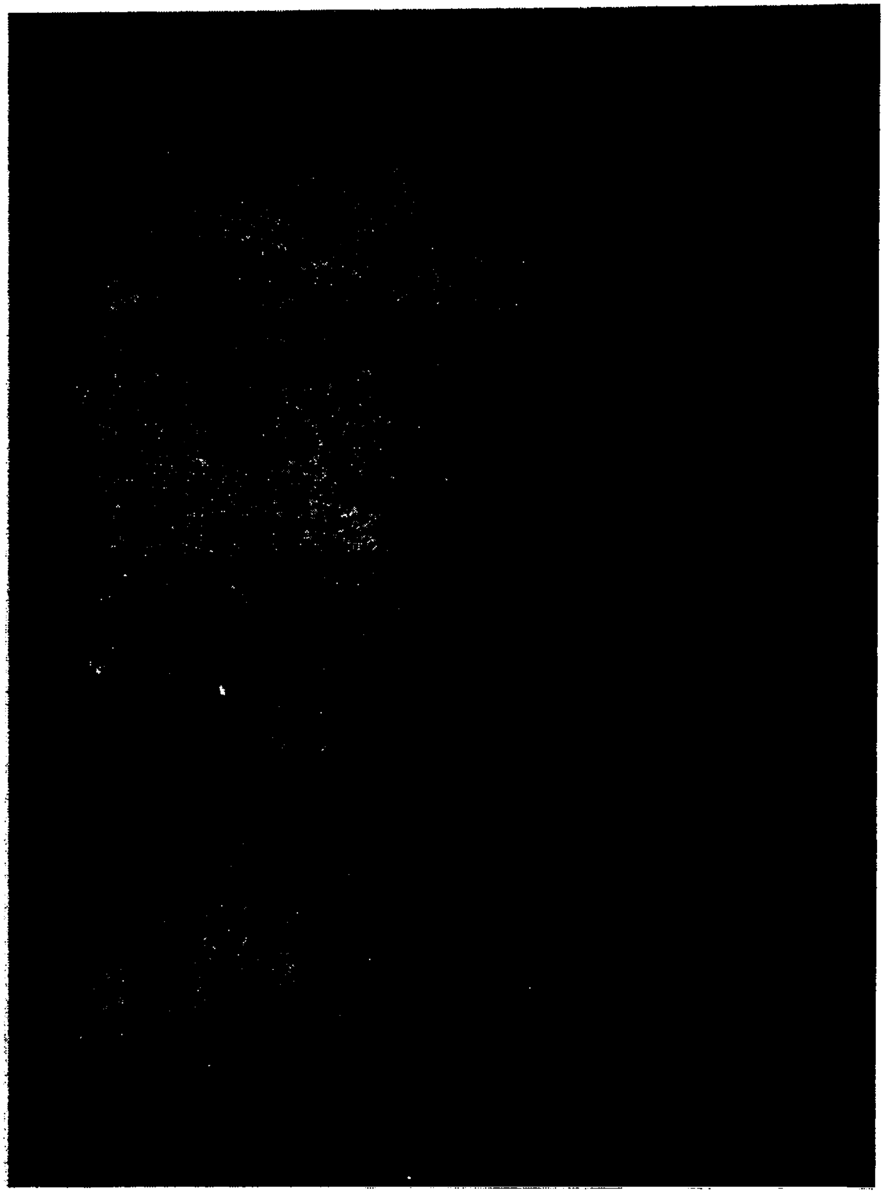

Fig. III-14. End-on X-ray Output from RF Discharge.

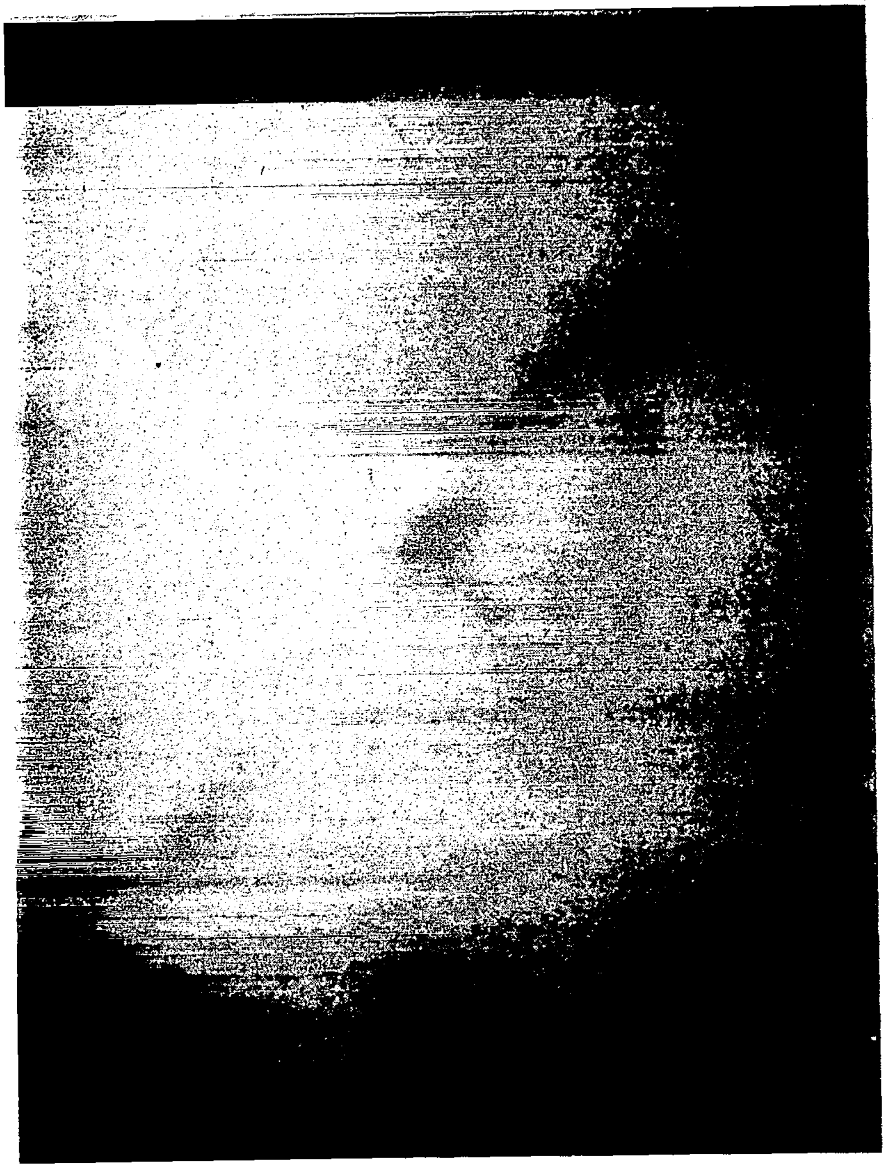

Fig. III-15. End-on X-ray Output from RF-Discharge

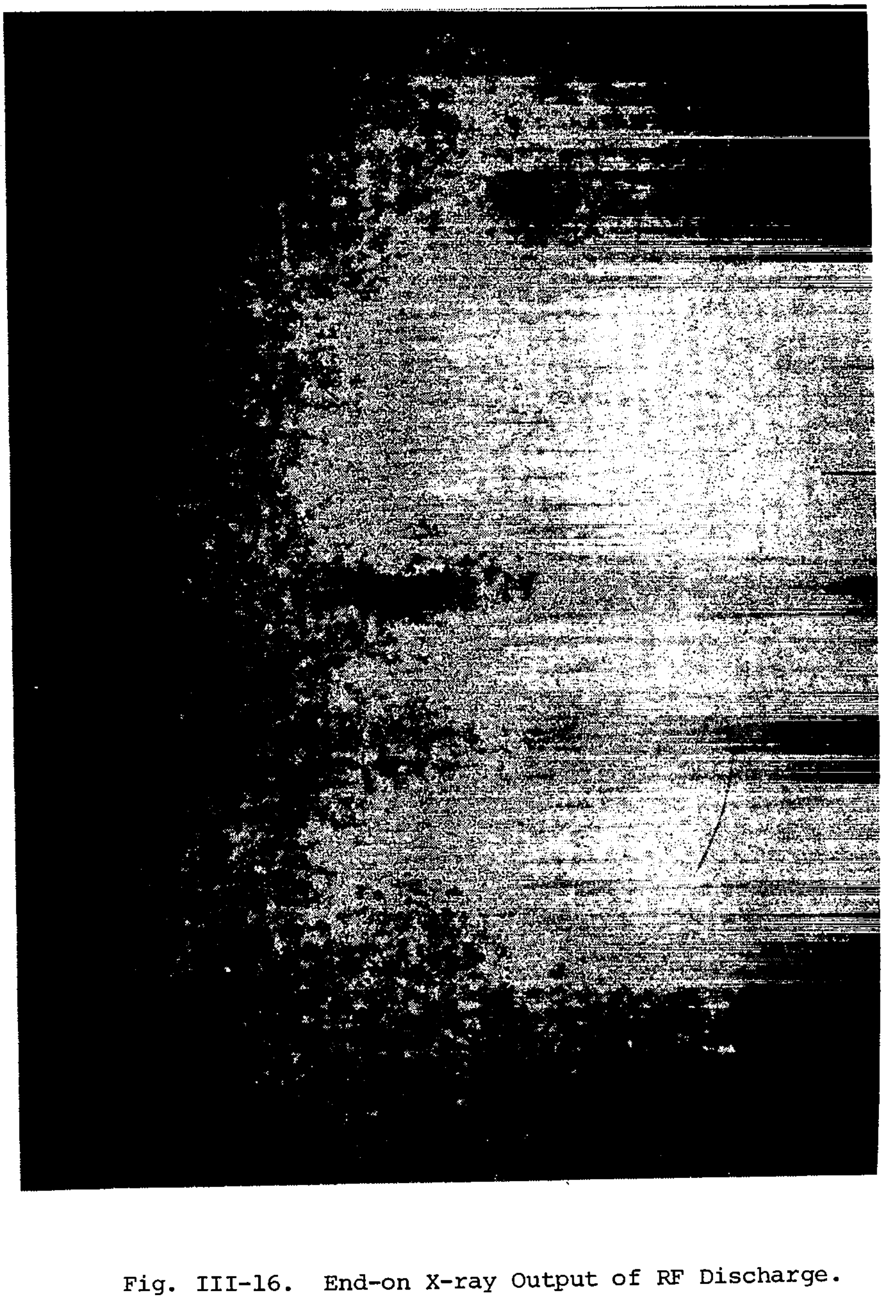

Fig. III-16. End-on X-ray Output of RF Discharge.

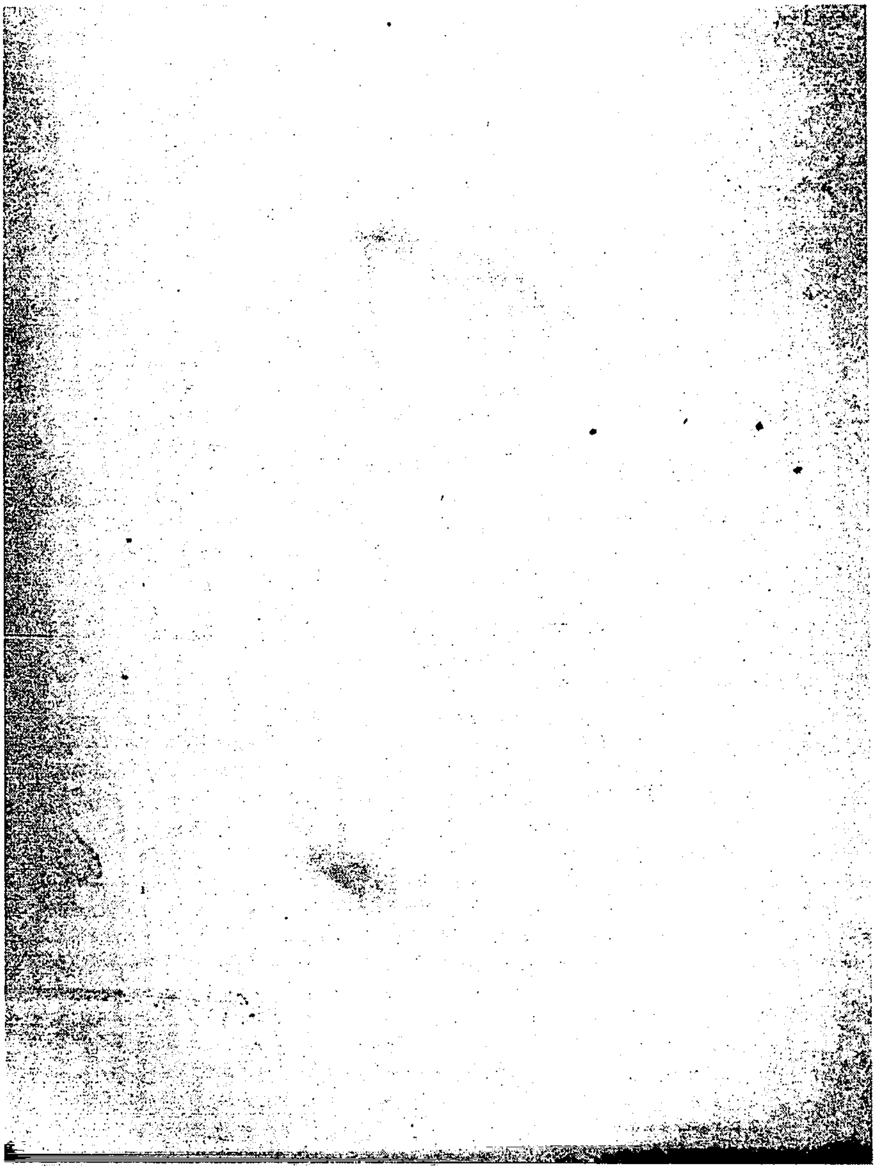

Figure III-17. End-on X-ray Output of RF Discharge.

The fact that the exposures are not in the center of the figure indicate that the beam does not come out straight but is (unpredictably) deviated to begin with.

Whatever the case may be, if the exposures shown in Figures III-13 through III-17 are caused by x-rays, these x-rays must be emitted in a preferential direction.

An attempt to measure the intensity of suspected x-ray emission was made. A Victoreen model 440 RF/A survey meter was placed next to one of the electrodes. The 440 RF/A is a highly sensitive ionization chamber with a broad energy response from 12 keV to 1.2 MeV. It is designed to perform x-ray dose rate measurements in high RF-fields. It is suited for soft x-rays, however, its response time is under these conditions as long as 12 seconds. Reproducible readings in the range of 1 mR/h to 3 mR/h were obtained. However, the long response time does not allow any cross correlation with actual operation parameters.

Also TLD chips were placed next to the tube. These chips were exposed for three hours and then counted and compared with control chips that had not been exposed. The conclusion was that the chips must have been exposed to a radiation field of 3.3 mR/h.

Also, an attempt was made to observe the x-ray pulses individually. For this reason a NaI-scintillation detector was placed close to one electrode. The output was displayed on an oscilloscope, and is shown in Figure III-18. Since the x-ray pulses come randomly, the camera shutter had to remain open for several seconds. During this time the discharge went through several million cycles. Power lines inside (the RF-shielded building) picked up the radiowaves and leaked it into the oscilloscope. However, the discharge is very repeatable. E.g., the traces in Figure II-13 are also second long exposures, which means also several

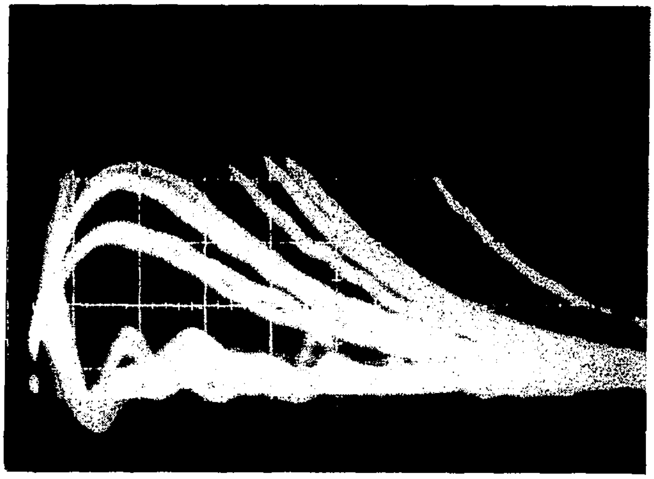

0.5 μsec/div

Fig. III-18. Individual X-ray Pulses.

million repetitions. Therefore, the traces coming from electrical interference can be seen as a band at the lower part of Figure III-18. The individual x-ray pulses are seen in the upper part of the picture.

2. Spectroscopic Studies

a. Experimental Arrangement

The system used for study of optical emission coming from the plasma is shown in Figure III-19. It consists of a 1 m Czerny-Turner grating spectrograph/spectrometer and an optical imaging system. For spectrometer operation, the scanning of the grating is accomplished by a stepping motor. Photoelectric registration is accomplished by an EMI 8575 photomultiplier tube and a picoammeter. The particular Czerny-Turner mount used is convertible to photographic registration by rotation of an auxiliary mirror into the spectrograph position.

The Czerny-Turner mount is equipped with a 1200 line/mm grating blazed for 4000Å (1st order). Demonstrated resolving power for this instrument is better than 0.1Å at 4000Å using 1st order.

The slit width used to achieve this resolution is 16 μm. For reasons of speed of observation in the studies described in the following, larger slit widths were used for photoelectric registration (up to 50 μm).

Slit illumination was accomplished with a 1:1 imaging system, placing the image of the plasma into the entrance slit plane allowing spatial resolution of the observed plasma structures.

b. Survey Spectra

Figure III-20a shows a photographic spectrum of the emission of the ENRAD device operating in hydrogen. The drive frequency was 1.35 MHz and the pressure was 0.6 torr. Since a slit width of 25 μm was used a long exposure time was required (6 hrs.).

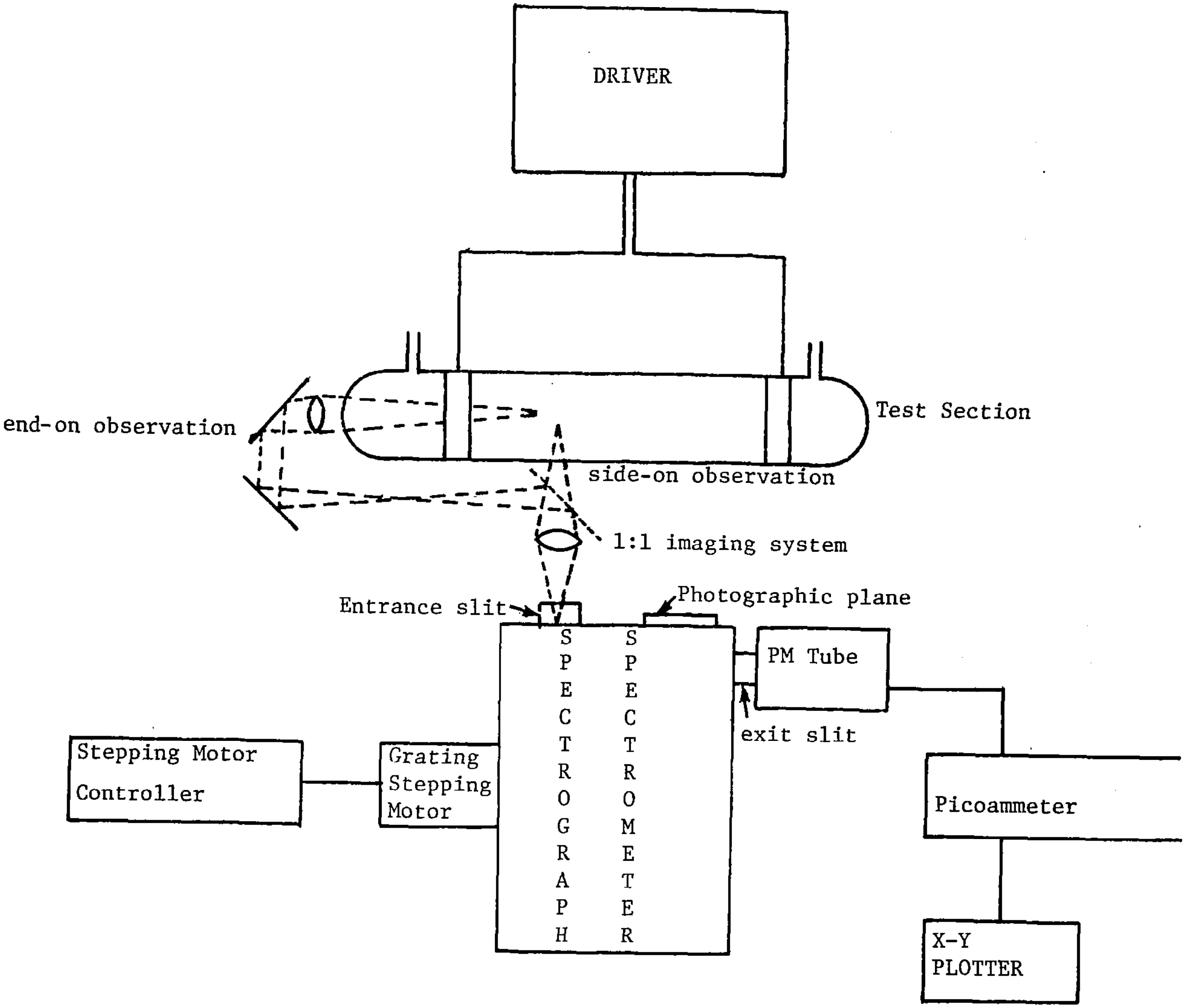

Figure III-19 System for the study of ENRAD optical emission.

Figure III-20b shows the spectrum of the emission of the ENRAD device operating in deuterium under the same condition. Both spectra were taken using side-on observation. They show expected features like the H_a,H_β and H_γ lines in the hydrogen discharge. D_α, D_β and D_γ can be seen in the deuterium case. In addition, features resulting from the emission of the hydrogen molecule are very prominent.

The Stark broadening of the hydrogen lines is very moderate. Based on the observed half widths, the electron density has to be less than 10^{12} electrons/cm^3. From this, it has to be concluded that even at the relatively low gas pressure under which the discharge is operated, the plasma is only partially ionized. This conclusion is corroborated by the presence of substantial H_2-emission. Usually in fully ionized hydrogen plasmas, molecular bands are weak or non-existent. For comparison, a spectrum of a hydrogen d-c arc is shown. (Figure III-21) This arc was operating at about 15 000°K which means it was almost fully ionized. There are no molecular bands visible and the Stark broadening of hydrogen lines is very prominent.

As pointed out before in the ENRAD device, electron formation takes place in the volume rather than in the vicinity of an electrode as is the case at discharges having internal electrodes. These latter discharges develop cathode and anode fall regions, which are vital for the maintenance of the discharge. In the cathode fall region acceleration of the electrons leaving the cathode takes place, requiring large electric fields (the major portion of the applied voltage is dropped across the cathode fall region). These fields are partially balanced by an electron cloud adjacent to the cathode fall region - the space charge. Here a high electron density and consequently considerable Stark broadening can be expected, while in the positive column, the electron density is moderate.

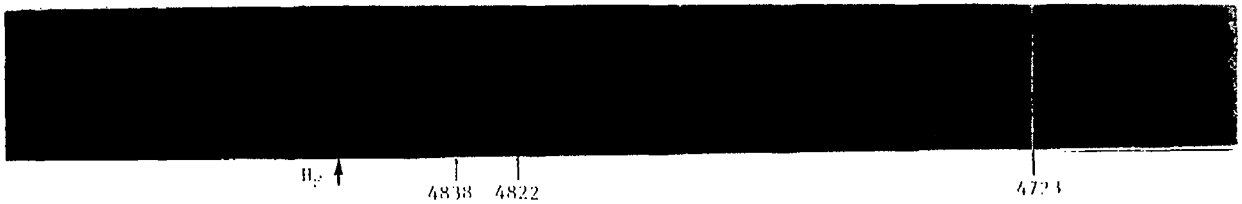

Figure III-20a Hydrogen Spectra from ENRAD device.

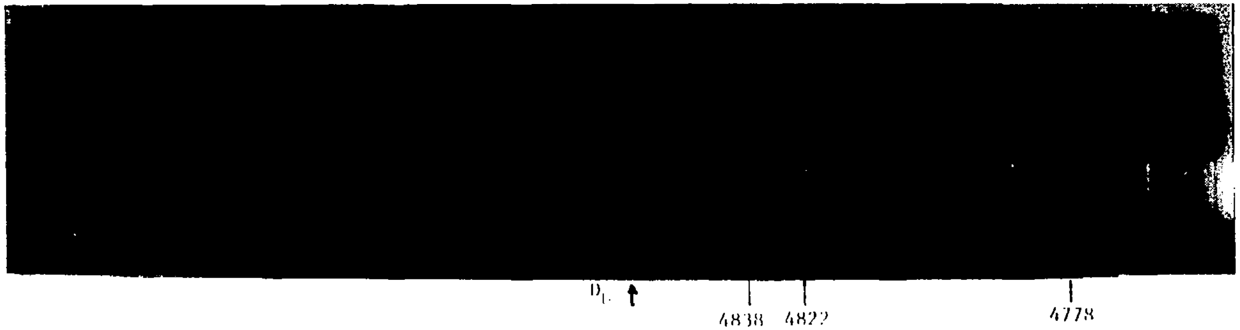

Figure III-20b Deuterium spectra from ENRAD device

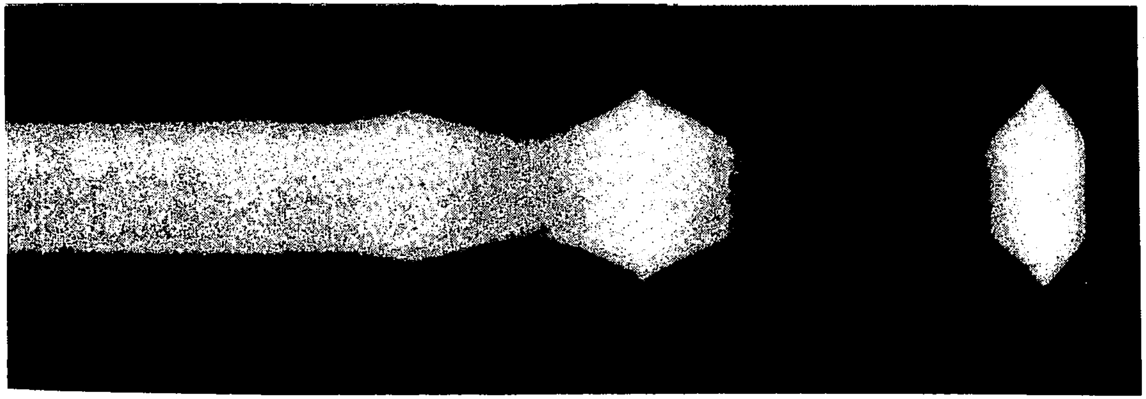

Figure III-21 Hydrogen D.C. arc at 15000 K

Figure III-22 is a spectrum of such a discharge. In the proximity of the electrodes, some of the spectrum lines (those which are subject to Stark broadening) are severely broadened, while only moderate broadening is observed in the plasma columns (the center portion of the lines). The two sample spectra of internal electrode discharges have to be compared to spectra obtained from the ENRAD device. The comparison shows that over the spatial region covered, there are no electron density gradients, especially no fall regions, a fact which was already mentioned as one of the advantages of a RF discharge with external electrodes.

c. Intensity Evaluation

The information contained in spectral emission rests in intensity, wavelength and line width. The latter two were discussed above to some extent.

The intensity of a spectrum line is given by

$$I = An^* \, h\nu \qquad \text{(III.1)}$$

where A is the transition probability, $h\nu$ is the photon energy and n^* is the number of atoms which are excited into the upper level of the line of interest.

If equilibrium exists or is at least locally approximated (local thermodynamic equilibrium, LTE) the quantity n^* can be computed using the Boltzmann factor:

$$I = n_o \, h\nu \, \frac{g}{U} \, e^{-\frac{E_x}{kT}}, \quad n_o = \frac{P}{kT} \qquad \text{(III.2)}$$

where n_o is the total particle density (p: pressure) g is the statistical weight (degeneracy); U is the partition function, E_x is the excitation energy, and kT is the thermal energy.

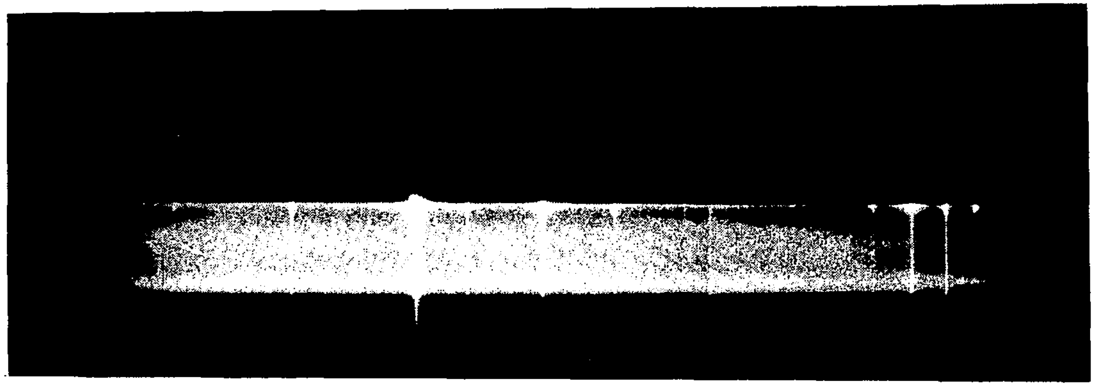

Figure III-22 Sectrum showing Stark broadening in electrode region.

If the relationship for the intensity of a spectrum line

$$I = A\, h\, \frac{c}{\lambda}\, n_o\, \frac{g}{U}\, e^{-\frac{E_x}{kT}} \qquad \text{(III.3)}$$

is rewritten in logarithmic form

$$\ln \frac{I\lambda}{gA} = \ln \frac{hcn_o}{U} - \frac{E_x}{kT} \qquad \text{(III.4)}$$

Using this relationship, one can relate the observable intensity to the excitation energy in a straight-forward way. If the factor $\frac{I}{gA}$, where the intensity is the only quantity which needs to be measured, is plotted on a logarithmic scale versus the excitation energy, a straight line with the slope $-\frac{1}{kT}$ should be obtained. Such a plot is usually referred to as a "Boltzmann Plot."

Any deviation from the straight line indicates deviation from a Maxwell Boltzmann distribution of states (which is the prerequisite for the validity of the Boltzmann factor). A point laying above the line suggests an overpopulation of the particular state, while a point laying below the line suggests underpopulation of this state.

A resonance phenomenon is a non-random event. Therefore, one would expect that for a resonating laser cavity, at least the point belonging to the upper laser level would not fall on the straight line. The same has to be true for the ENRAD device if it is truly a resonance machine. For this reason, two Boltzmann plots have been taken. One was taken under conditions where the ENRAD device was operated like an ordinary RF discharge, showing no particular plasma structure. The resulting Boltzmann plot is shown in Figure III-23. The deviation of the points from the 3400°K line are probably within the error of measurement. The conclusion is that the plasma is more or less in LTE at a moderate temperature of

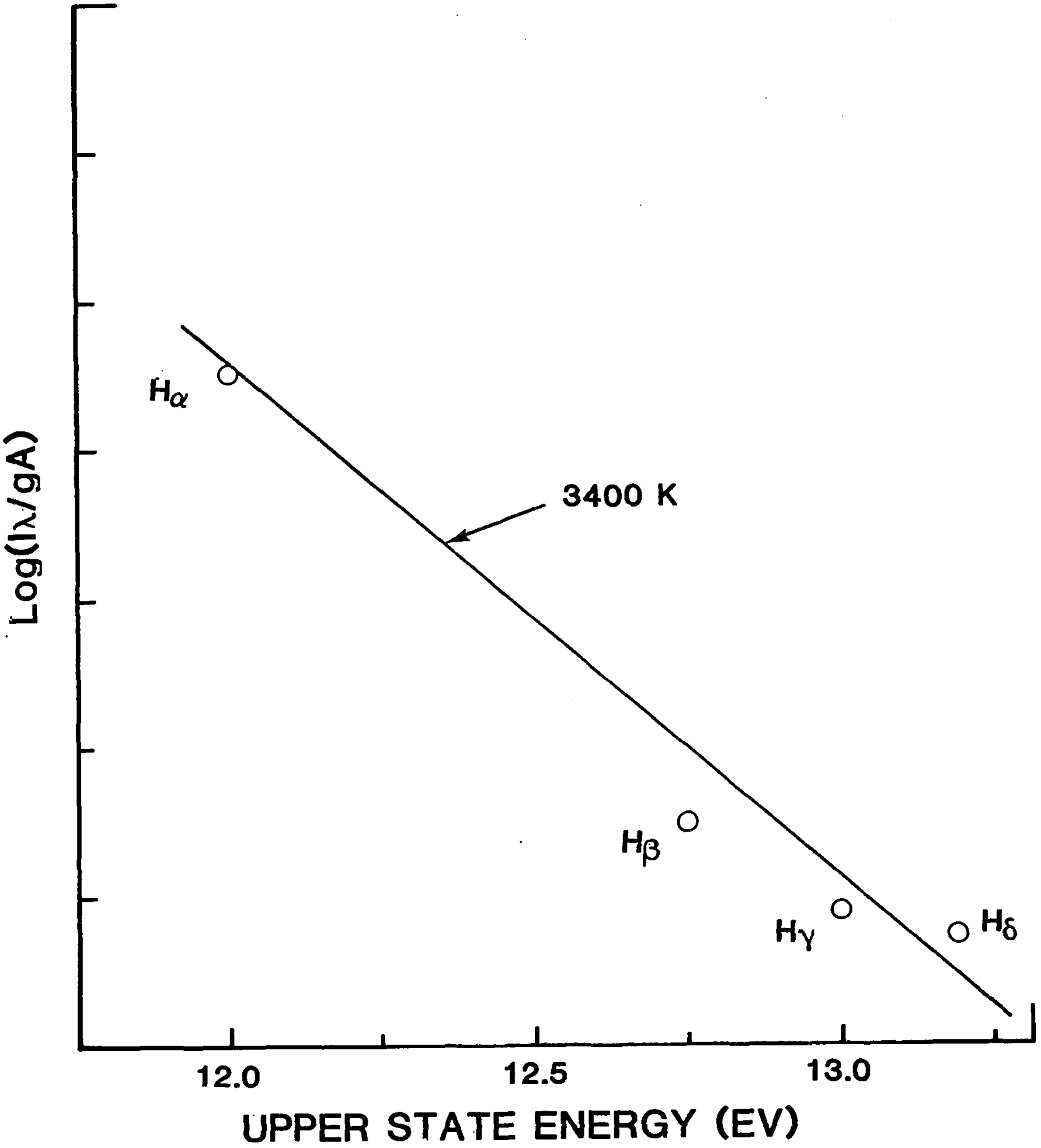

Figure III-23 Boltzmann Plot of the Hydrogen H_α, H_β, H_γ, and H_δ Lines

3400°K. This temperature will produce only a small thermal ionization of the plasma, which is consistent with previous conclusions.

However, if the ENRAD device is operated in resonance conditions, where x-ray and neutron emissions are observed, the Boltzmann plot is changed drastically. Figure III-24 shows such a Boltzmann plot for the deuterium case. A substantial deviation from LTE can be seen. In order to appreciate the magnitude of the deviation, it is convenient to superimpose Figure III-23 and Figure III-24. To be able to do this properly, one should appreciate that the intensities usually used for Boltzmann plots are relative intensities. A closer examination of equation III-4 shows that only relative intensities are required. Therefore, the intercept of the straight line with the ordinate (zero excitation energy or ground state population) is only correct within a constant factor which is different for each gas. Therefore, in order to superimpose both figures, one of them has to be moved parallel to the ordinate until one point of one figure matches the corresponding point on the other. In case of Figure III-25, the point for D_γ (H_γ) were matched. As can be seen from this figure, the deviations are large, covering several orders of magnitude. Although the decision to match the point for D_γ(H_γ) is arbitrary; there is a good argument for why they should be matched in contrast to the points H_α(D_α). The slope of a line drawn from D_γ to D_β is roughly the same as the slope of the Boltzmann Plot for H_2 under non-resonant conditions. (Figure III-23). It is reasonable to assume that both conditions produce about the same electron temperatures (for such electrons which are thermalized). Therefore, the conclusion drawn from Figure III-25 is that D_α is heavily underpopulated when the device is operated with

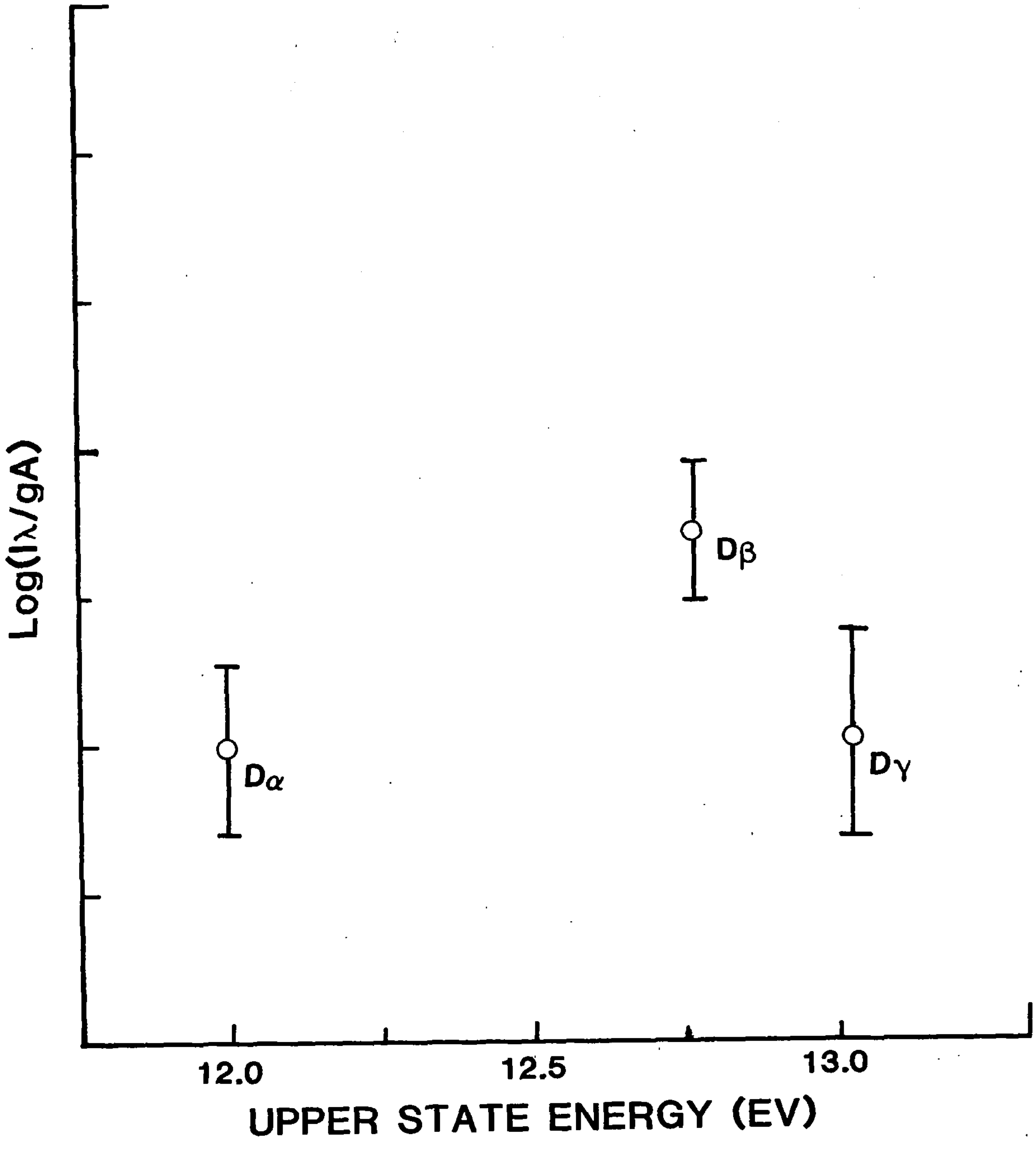

Figure III-24 Boltzmann Plot of Deuterium D_α, D_β, and D_γ Lines cavitons established. If one assumes that the walls of the cavitons are formed by ions interacting with the RF field, the observed radiation has to come from excited atoms, which are freshly recombined ions. Since the cross sections for recombination into higher laying states are larger than into lower laying states, it is understandable that the higher laying D_β and D_γ upper line levels are thermalized before the upper D_α-line level, which explains why this level is underpopulated.

d. Doppler Shifts

If the ENRAD device indeed produces directed ion velocities--namely a beam impinging on the caviton walls--this fact should be detectable by measurements using the Doppler effect. However, if the high ion velocity is random (temperature), a Doppler broadening of the Balmer lines should be detectable. If the beam should exhibit some spread in energy without being randomized in direction (or only randomized to a small degree), a broadened Doppler shifted line is expected.

To demonstrate an existing Doppler shift side-on and end-on light was superimposed on the spectroscopic plate, without moving the peak between exposures. The optical arrangement for doing this can be seen in Figure III-19. A blue shift for the end-on radiation is clearly visible in the photographic spectrum depicted in Figure III-26. The size of the shift is about 1Å, which translates into 40 eV directed motion.

The end-on observation spectrum shows also a feature at a part of the D_β line which corresponds to the part of the plasma which is in the vicinity of the wall. This feature is an additional broadening, which is shaded towards the blue. However, the information available does not allow a distinction whether this feature is an additional Doppler shift or a Stark broadening.

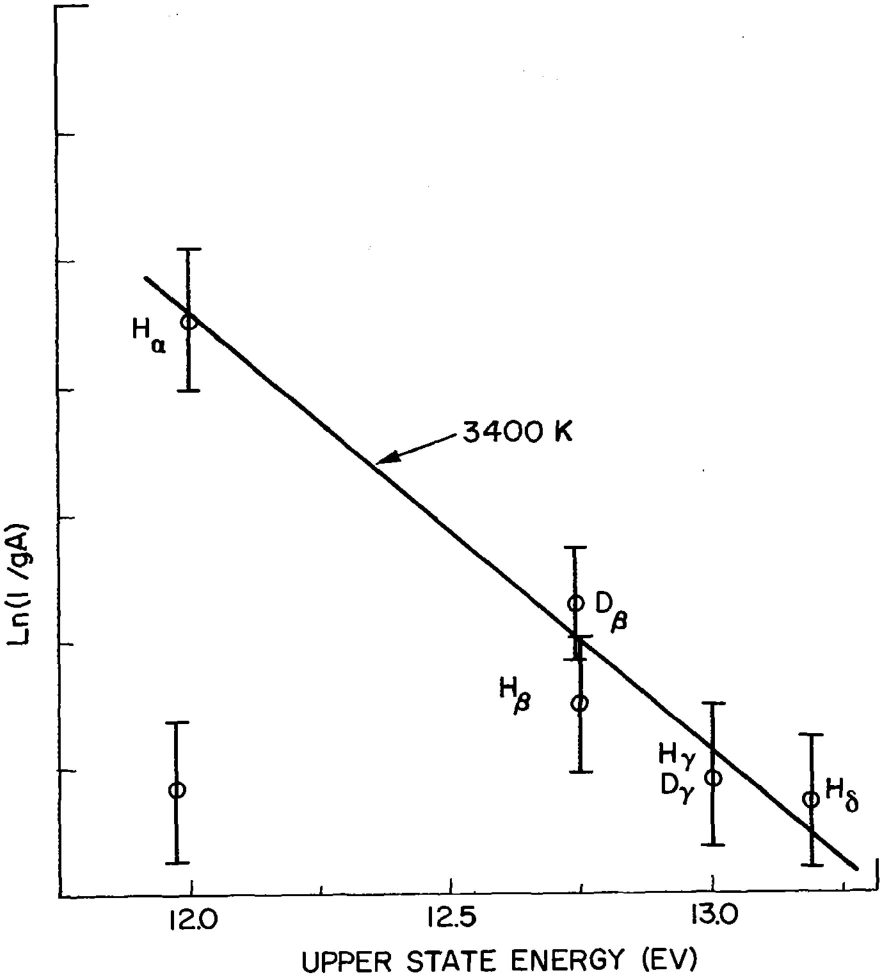

Fig. III-25. Combined Boltzmann Plots of Hydrogen and Deuterium Showing Magnitude of Inversion.

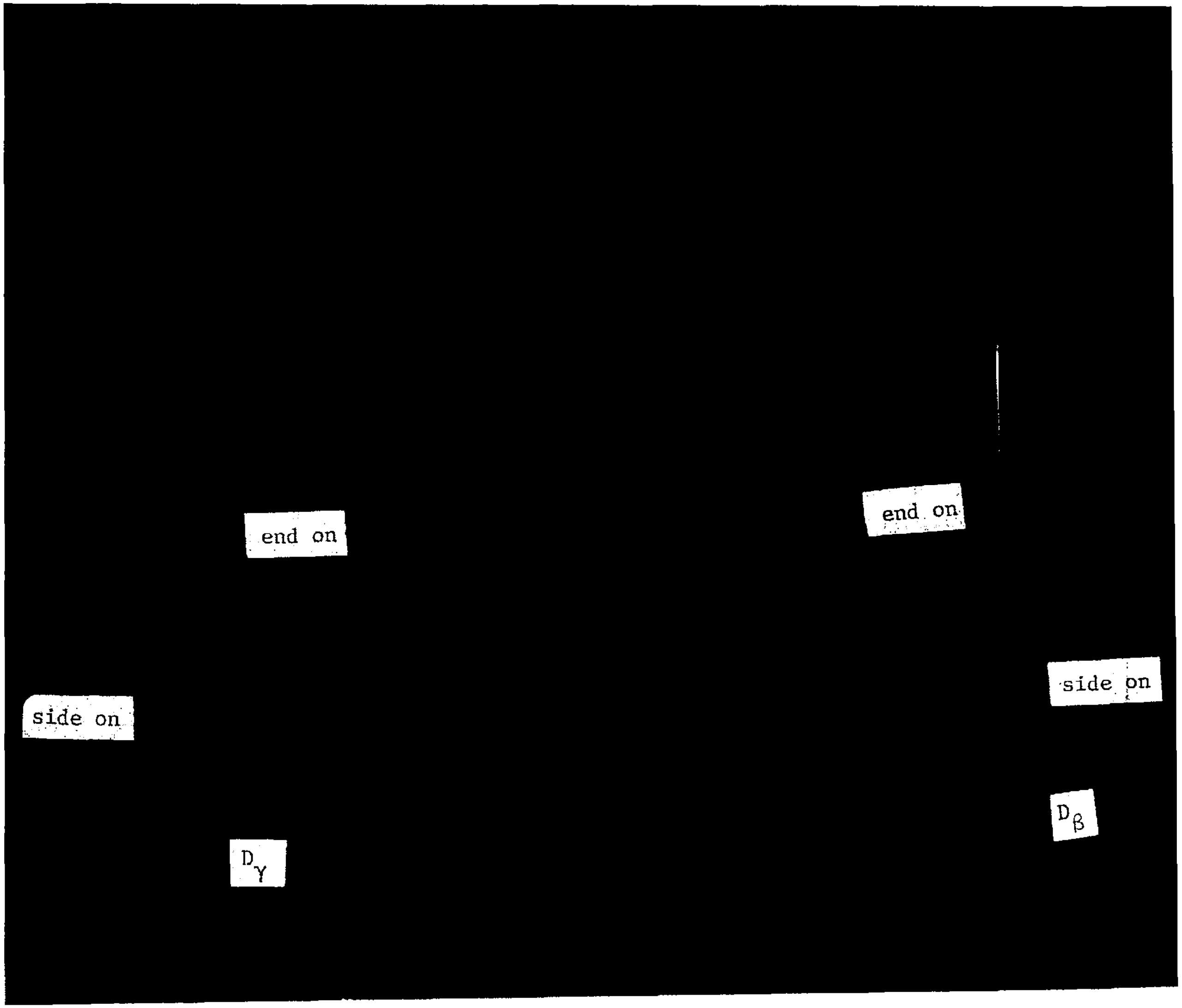

Fig. III-26. Doppler Shift for D_β and D_γ Side On vx End On

Blue →

3. Neutron Emission

In the following we will show that the ENRAD device emits neutrons when operated in deuterium and when cavitons are present.

The results presented here were obtained under this effort only. Since the neutron emission is quite unexpected for such a low voltage discharge, we felt it was necessary to have the neutron emission verified by a researcher not involved in this project. This independent measurement was done by Dr. William H. Ellis, University of Florida, and is reported in Appendix A.

Figure III-27 shows the system used to study the emission of neutrons from the deuterium plasma structures. The detector is a BF_3 tube operating in the proportional counting mode. The tube and associated electronics are RF shielded and extensive tests were performed to guarantee that the RF interference did not influence the counter system. The system was then calibrated so that an exposure of $3.6 \times 10^6 \pm 20\%$ neutrons would result in 2000 counts or 1800 ± 350 neutrons per count. The same moderator was used for calibration and all tests.

The system was filled to 300 torr of deuterium and pumped down to 50 microns within 10 minutes. During the 10 minute cycle, the neutron detector was turned on and counts were accumulated.

Table III-1 gives the results of the various runs with the neutron counting system. With D_2 gas, statistically valid results show that neutrons are being produced by the plasma. These neutrons are expected to result from the

$$ {}_1D^2 + {}_1D^2 \rightarrow {}_2He^3 + {}_0n^1 \qquad \begin{array}{ll} E_{He}: & 820\text{ keV} \\ E_n: & 2450\text{ keV} \end{array} $$

nuclear reaction.

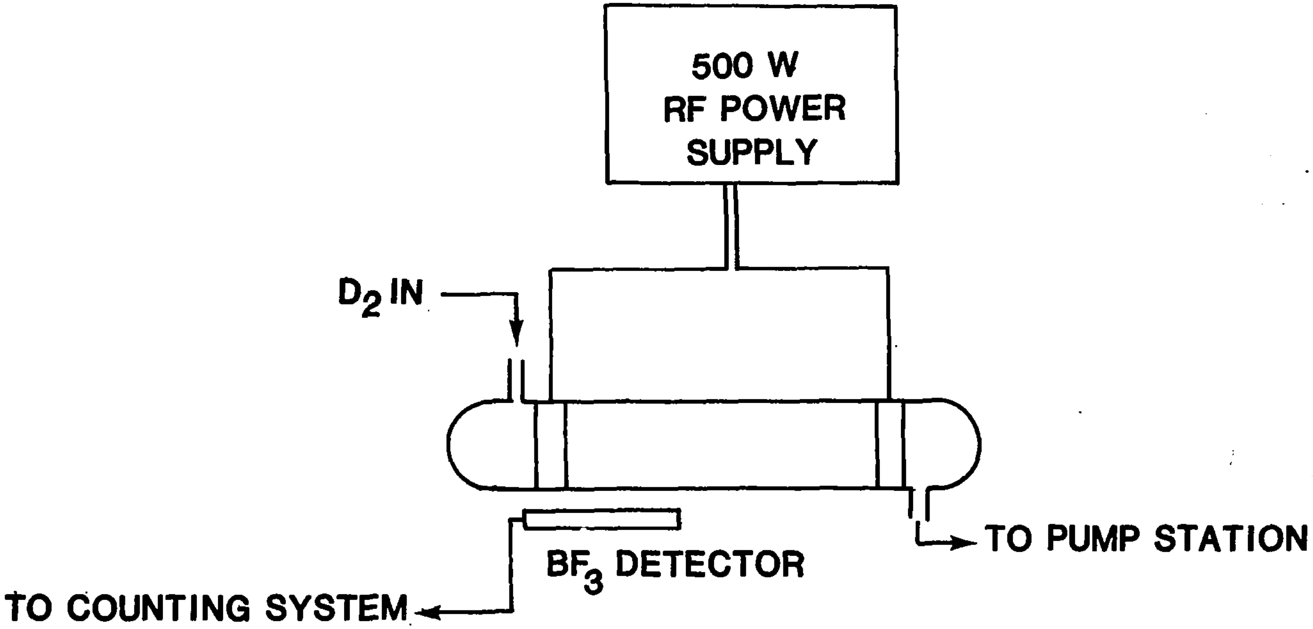

Figure III-27 System for the study of neutrons from ENRAD device.

TABLE III-1

Gas	Counts		Net Counts	
D_2 with moderator	115.20	17.25	78.45	20.03
D_2 w/o moderator	37.67	7.23	-	
H_2 with moderator	42.50	4.95	5.75	15.73**
H_2 w/o moderator	30.00	3.87	-	
*Air with & w/o moderator	40.5		-	
*Evacuated Tube with & w/o moderator	33.0		-	
Background	36.75	10.78		

*Average of * items)

**Not statistically valid

Neutron emission from the ENRAD is low. Therefore, to verify that the detection system was not influenced by RF interference, an alternative technique of neutron detection, namely neutron activation, was performed.

A gold coin enclosed in a paraffin moderator was irradiated for 24 hours. The pd (pressure x interelectrode distance) was such that 6 pair of disks were formed. The gold coin was counted immediately after irradiation. The result was a corrected count rate of 80 CPM. Figure III-28 shows the decay curve for the foil. The slope of the decay curve computed to be a half-life of 2.7 days which is the half-life of gold. This indicated the BF_3 neutron counter was functioning correctly.

The emission of neutrons by the ENRAD device has several parameters which were measured. The first parameter measured was the neutron count vs frequency. Figure III-29 shows a plot of the data for frequencies between 1.20 and 1.45 megahertz. The pressure (with a constant d) varied during the taking of the data. It varied from a high value sufficient to produce a diffused discharge to a low value capable of producing the degenerated disk discharge within 15 minutes. The data does not indicate that the shape of the fitted curve needs to be a straight line, but may be a resonance shape with a peak about 1.34 megahertz.

Another parameter measured was the location of the maximum neutron emission. The results indicate that the location for maximum neutron emission spreads from around the mid-point in the discharge to the grounded electrode. The rotational position about the ENRAD axis had a homogeneous neutron emission.

The last parameter measured was the amount of neutron emission vs percent nitrogen admixture. It was found that .5% nitrogen admixture to the deuterium increased the neutron output without destroying the plasmoid

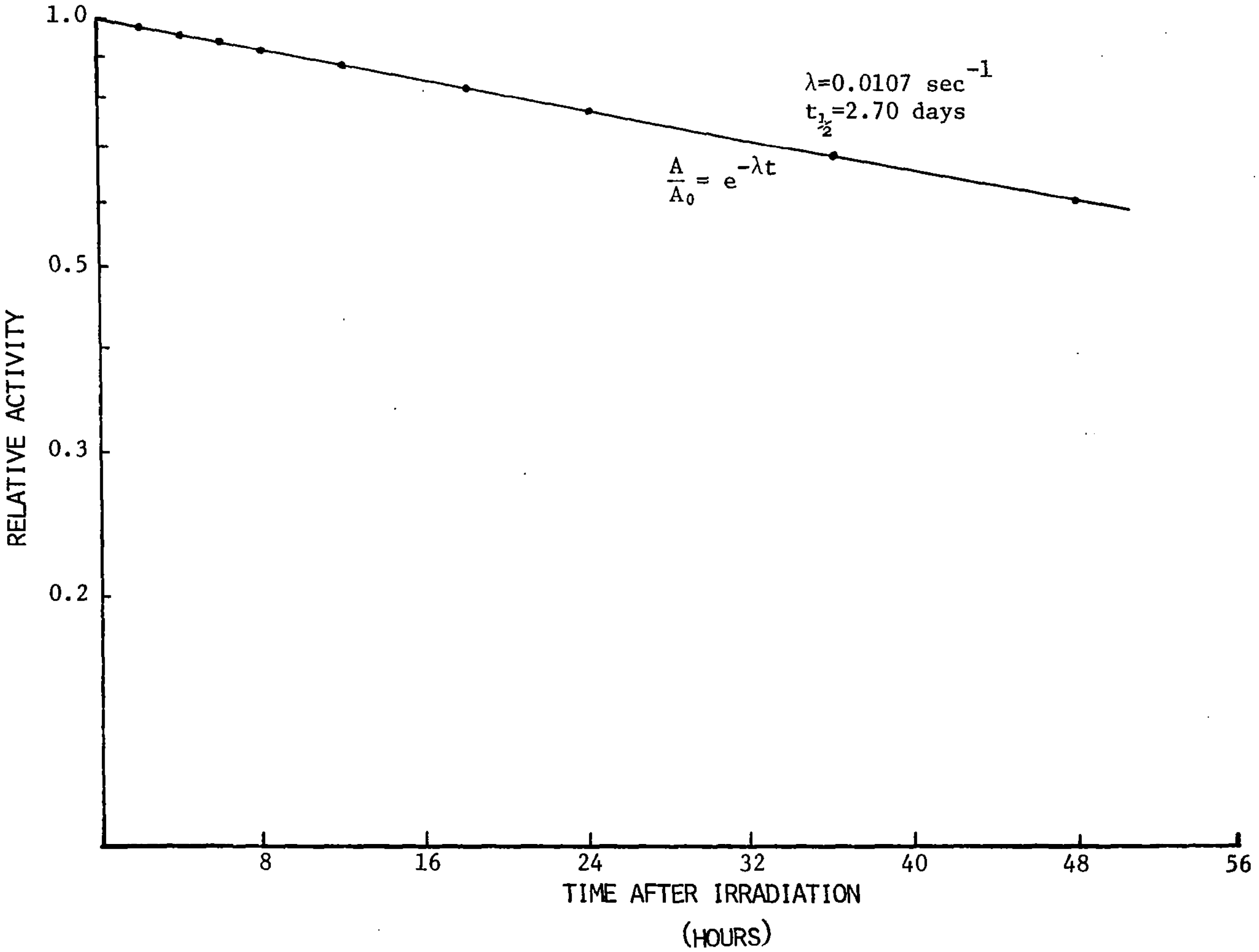

Fig. III-28. Decay curve for exposed gold piece

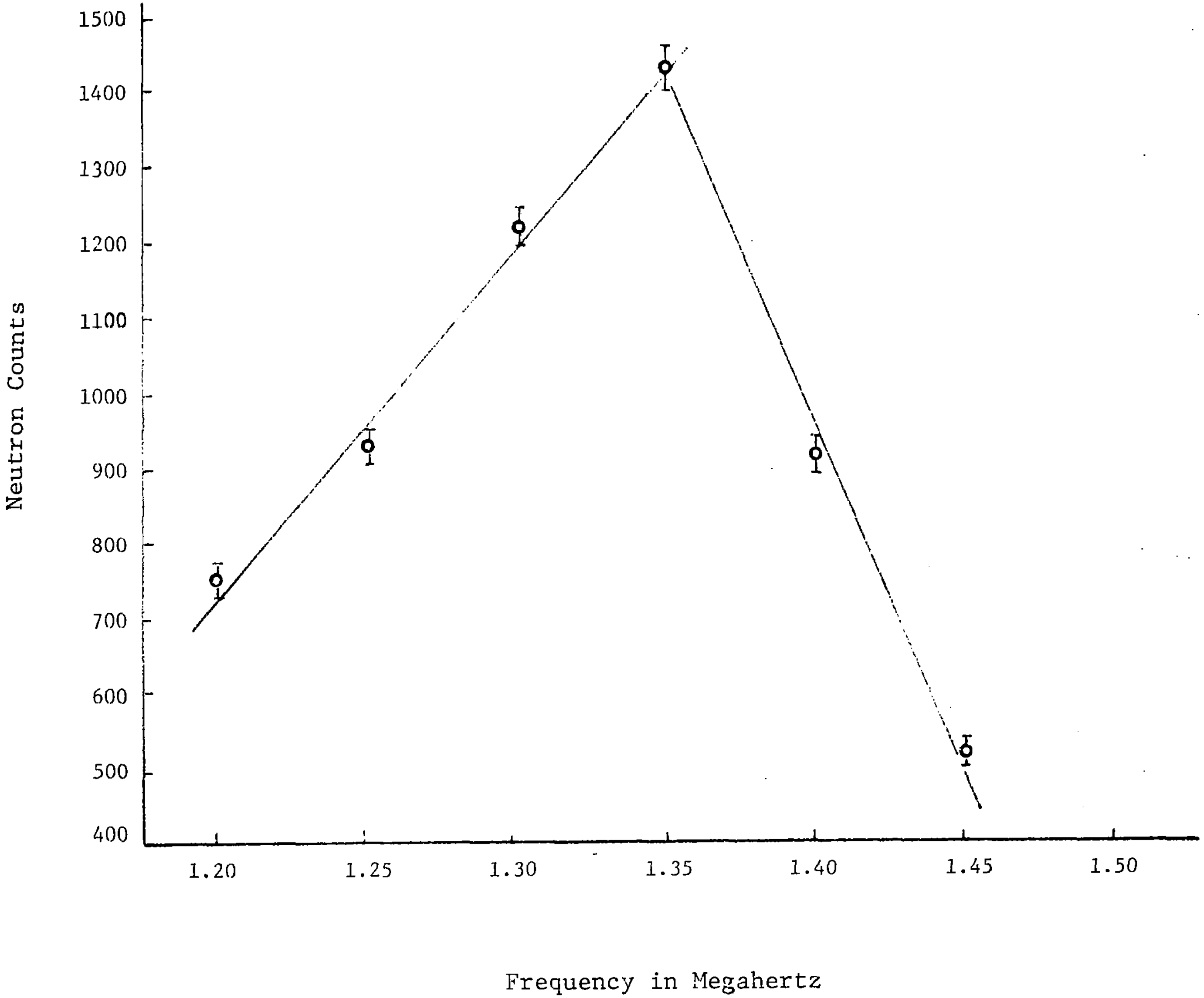

Fig. III-29. Neutron Counts vs Frequency disks. Figure III-30 shows a plot of this data. As the admixture went to zero, the neutron count rate stabilized at approximately 300 CPM.

The admixture altered the stability of the plasmoid disks. An instability manifested by flickering between n and n + 1 disk pairs was observed. With an admixture of nitrogen, the flickering between n and n + 1 disks could be maintained for several seconds. This is not to say that during the instabilities the neutron output increased, since the neutron counting system does not resolve short times (the order of seconds). However, these results could be an indication that the neutrons are generated by instabilities.

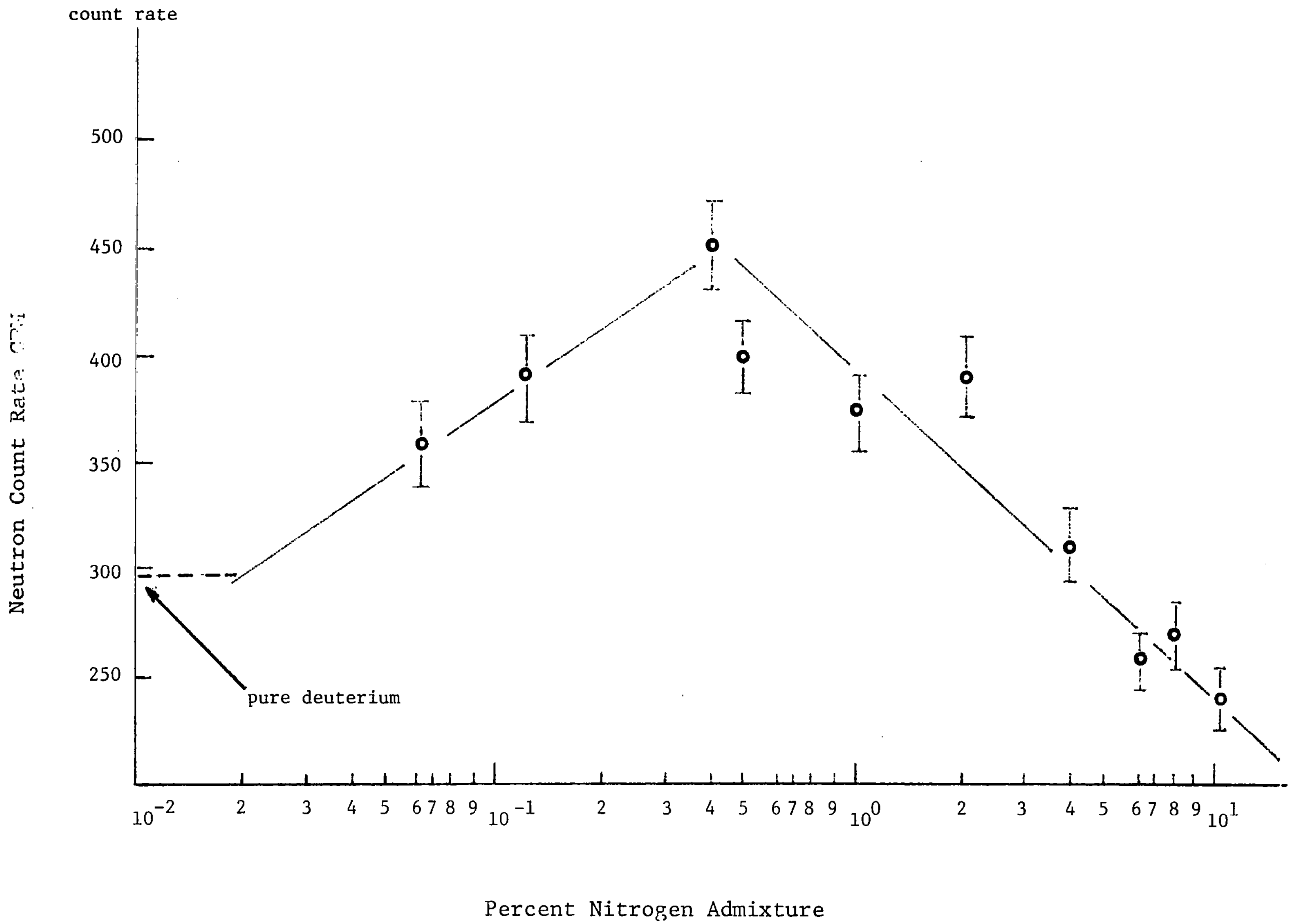

Fig. III-30. Neutron Count Rate vs Percent Nitrogen Admixture

IV. EXPERIMENTAL OBSERVATIONS OF CAVITONS

1. Probe Measurements

Cavitons have been observed before by others at lower pressures. In reference IV-1 the time averaged charge densities around such cavitons are reported. These measurements are made with an ion beam probe. Although the RF discharge used in reference IV-1 had electrodes, while ours is electrodeless, certain similarities exist, e.g., they also report observation of a dark sheath. Figure IV-1 shows some of their results. The striking feature is the charge walls surrounding the cavitons.

We like to compare these (very sophisticated) measurements to some old measurements of our own made with a Langmuir probe (Figure IV-2 and IV-3). The Langmuir probe disturbs the plasma to some extent. Also, the interpretation of the probe data assumes a Maxwellian electron distribution. For these reasons our probe measurements have to be regarded as somewhat crude and they are only reported here because of their similarities with the measurements in reference IV-1.

Figure IV-2 shows the results for 1.5 x 10^{-2} torr. At this pressure only degenerated cavitons (see also Figure II-11) exist. The electrode to which those cavitons attach is located at 12 cm. An indication of a surrounding charge wall is visible. The electrons in this wall region cannot be expected to have a Maxwellian velocity distribution, since they are accelerated towards the wall. The Langmuir probe evaluation process, therefore, overestimates their temperature.

Figure IV-3 shows the results for 6 x 10^{-1} torr. The electron density shows now a minimum in the center and moderate walls towards the electrode. Results in Figure IV-2 (1.5 x 10^{-2} torr) have to be compared with the 1.0 x $1.^{-4}$ curve in Figure IV-1 and the result in Figure IV-3 (6 x 10^{-1} torr)

Figure IV-1 Charge Density Walls Around Cavitons. After Ref. (IV-1).

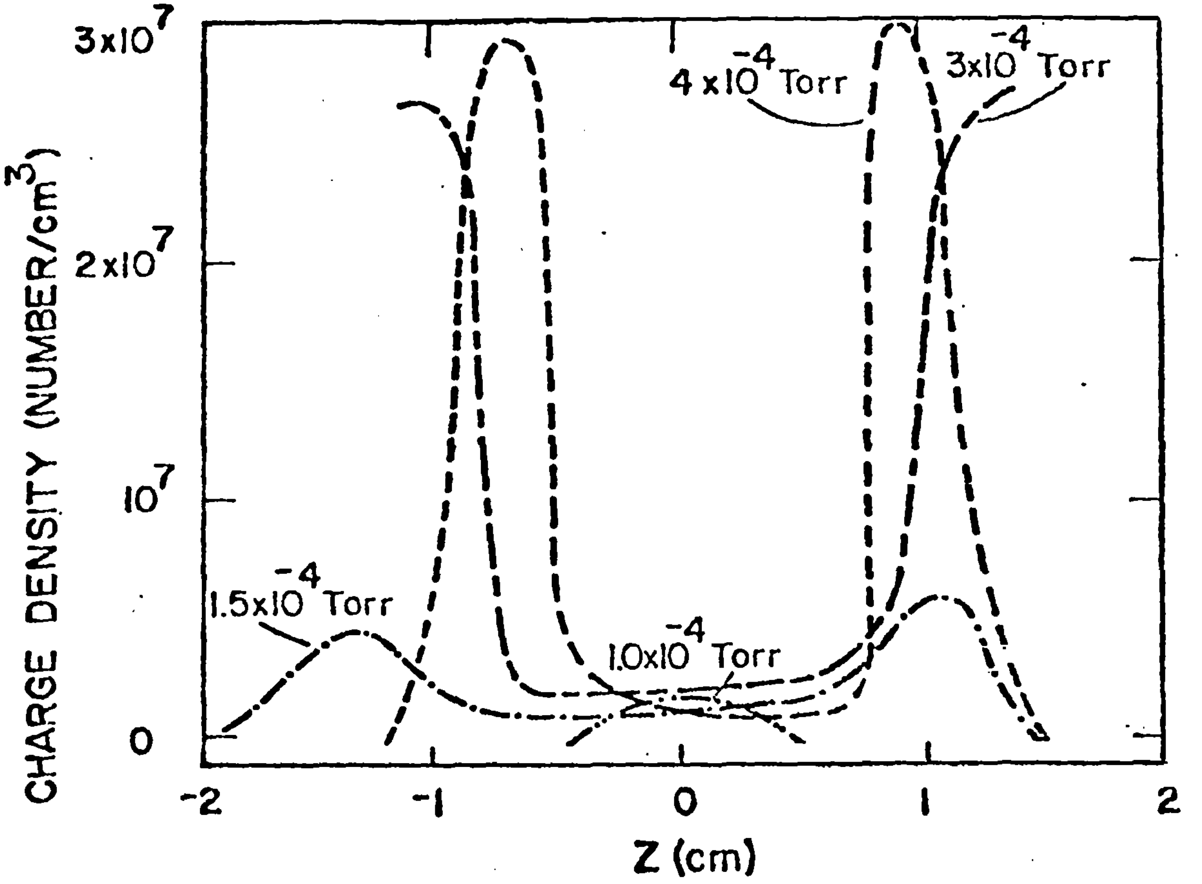

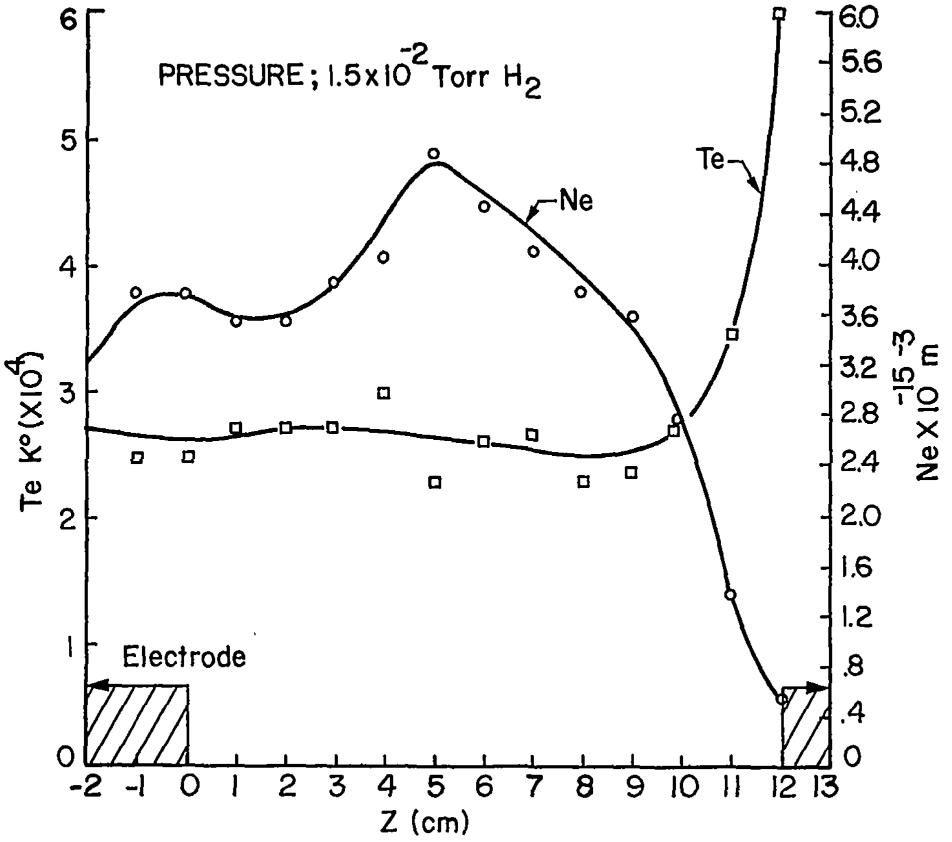

Fig. IV-2. Electron Density and Temperature. from Langmuir Probes (Electrodes at 0 and 12 cm).

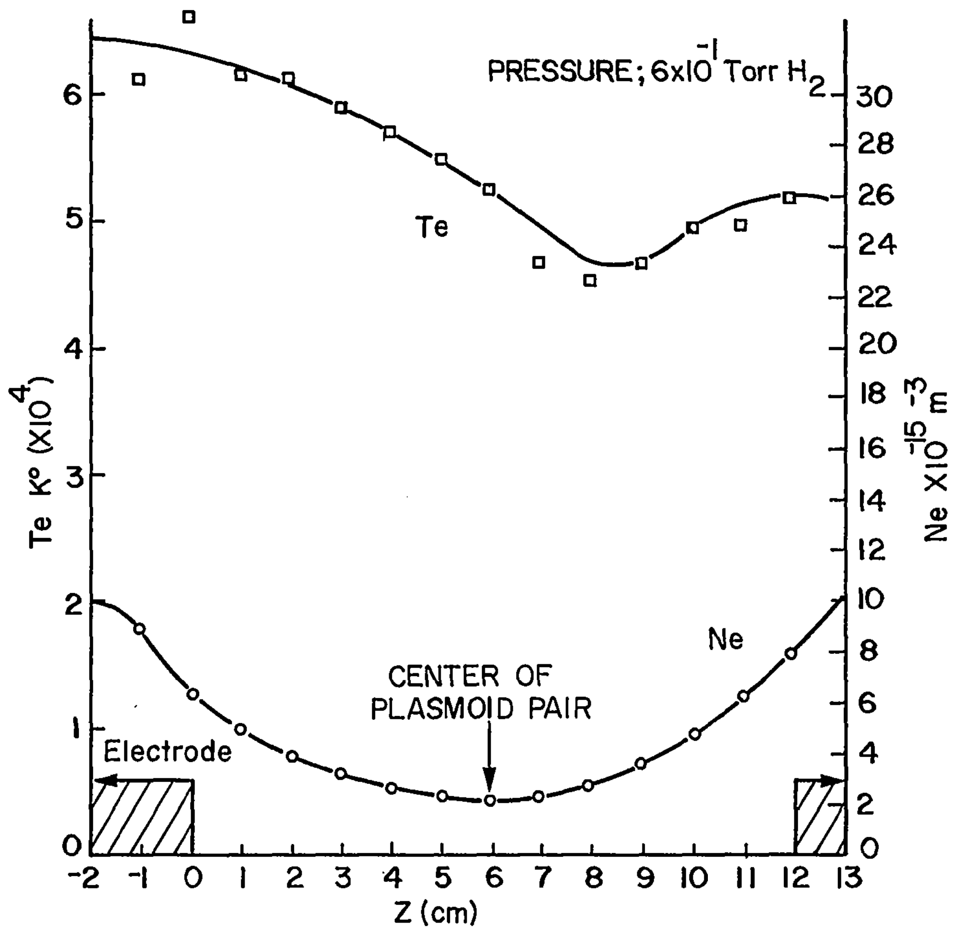

Figure IV-3. Electron Density and Temperature. From Langmuir Probe (Electrodes at 0 and 12 cm.).

have to be compared with the 3 x 10^{-4} torr curve in Figure IV-1. Obviously, the Langmuir probe measurements cannot bring out the steep walls of the caviton as good as the ion probe does, but the indications are there.

The conclusion to be drawn from these measurements is that the caviton is surrounded by steep charge density gradients caused by "digging in" of the applied RF field. In our discharge the cavitons are actually visible. The structure seen must consist of excited atoms, which form a density wall around a dark space in which at least no excited atoms exist. The ions and electron are, of course, not visible but the probe measurement indicates existence of similar density walls as the visible ones. The Langmuir probe measurements do not have sufficient spatial resolution to prove that both kind of walls are located at the same distance from the electrodes. Geometry and pressure of the discharge of reference IV-1 are too different for allowing quantitative comparison.

2. Collimated X-Rays

The original goal of the effort was to show existence of coherent x-rays. We have shown evidence of emission of x-rays in a preferential direction. However, this does not necessarily mean these x-rays are coherent.

In the following an attempt is made to explain the mechanism of generation of collimated x-rays for the case of the degenerated cavitons.

Both devices--the high voltage pulsed dc discharge and the low voltage RF discharge--produced at least collimated x-rays. This in indicated by the result shown in Figures III-3 and III-13 through III-16.

Since Figure III-3 is always reproducible, while Figure III-13 through III-15 show a wide spread in phenomena, the discussion on collimated x-rays is limited to the pulsed dc device in the following.

It is claimed that Figure III-3 could only be obtained by exposure to an x-ray source which emits in a preferential direction.

Figure III-3 was obtained by wrapping an x-ray film around the discharge tube. It is now first attempted to explain the obtained exposure by x-rays generated by impact of electrons on the glass tube. Referring to Figure IV-4, assume that the electric field has a configuration which forces the free electrons to impact on an area of the glass tube adjacent to the negative electrode. Assume further that the field has an infinitely steep gradient toward the right side of the impact point "A," which means no electrons impacting at the right side of point A and many electrons are impacting on the left side of point A.

In this case, point A can be considered as a point source for isotropic x-ray bremsstrahlung. (Only if the impact energies were in the MeV range non-isotropic radiation could be expected.) The darkening of the x-ray film, at the right side of point A, is of interest.

Neglecting scattering for the moment and dealing only with absorption in the glass tube, the intensity of the bremsstrahlung at point $x = 0$ on the x-ray film is

$$I = I_o e^{-kd}$$

where I_o is the intensity emitted at point A, while k is the absorption coefficient of the glass and d is the thickness of the glass wall.

The intensity of the x-ray exposing the film at the right side of point A $(x>0)$ is given as a function of x by

$$I\ (x) = I_o\ e^{-k(\sqrt{x^2+d^2})}$$

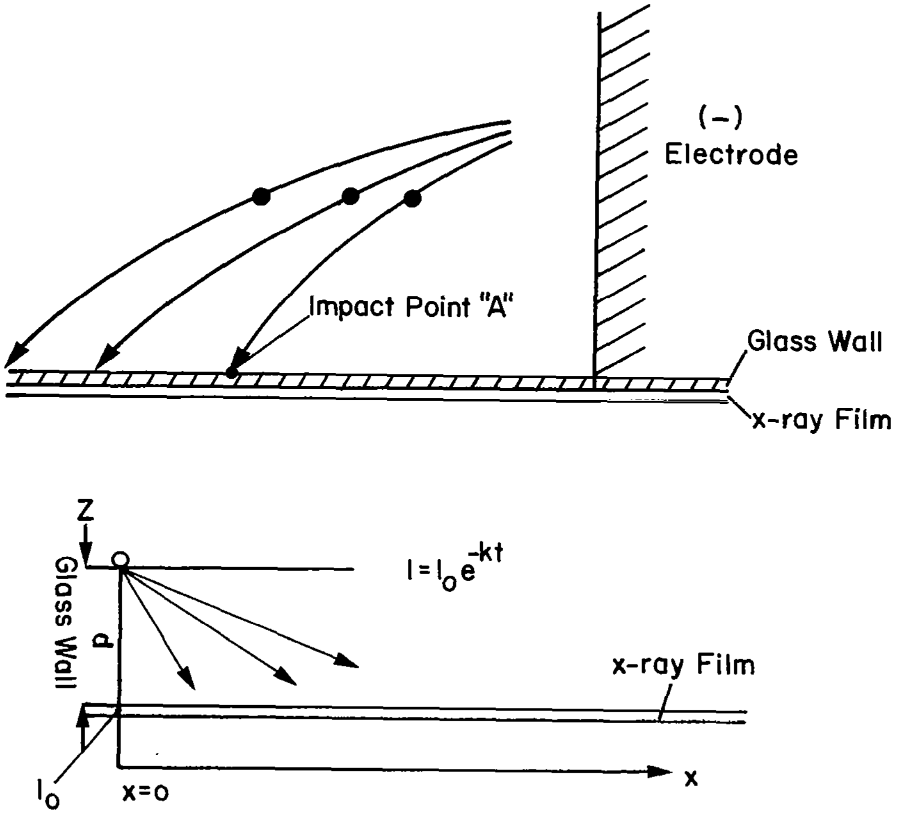

Fig. IV-4. Bremsstrahlung from Impact on Glass Wall.

The sensitivity of the photographic material (in the "straight" portion of the sensitivity curve) is logarithmically related to the energy exposing the film.

Therefore, the ratio between number of exposed grains (density) on the left side to the number of those on the right side is at best

$$\log \frac{I_{(x)}}{I_o} = -k\sqrt{(x^2+d^2)}$$

which is a linear dependence and not at all the steep density gradient which is observed. Scattering in the glass was neglected, as well as the fact that the points left of point A are also isotropic x-ray sources and will add to the exposure of the x-ray film at the right side of point A. This will even further reduce the expected density gradient on the film.

The conclusion is that the exposure shown in Figure III-3 cannot possibly be caused by bremsstrahlung generated by impact of electrons on the glass wall.

However, the figure can be explained at least qualitatively by the assumption that a "degenerated caviton" existed under the conditions at which the exposure was obtained. Figure IV-5 shows a number of such degenerated cavitons for the RF discharge, where they are visible. This figure has to be compared to Figure IV-6 (a repetition of III-4) which is an x-ray exposure. By comparing these two figures, it is readily seen that such degenerated cavitons must be responsible for the observed collimated x-ray radiation.

A possible mechanism could be bremsstrahlung (or cyclotron radiation) which is caused by electrons vibrating back and forth across the boundary line of the caviton. In order to produce x-rays under such conditions,

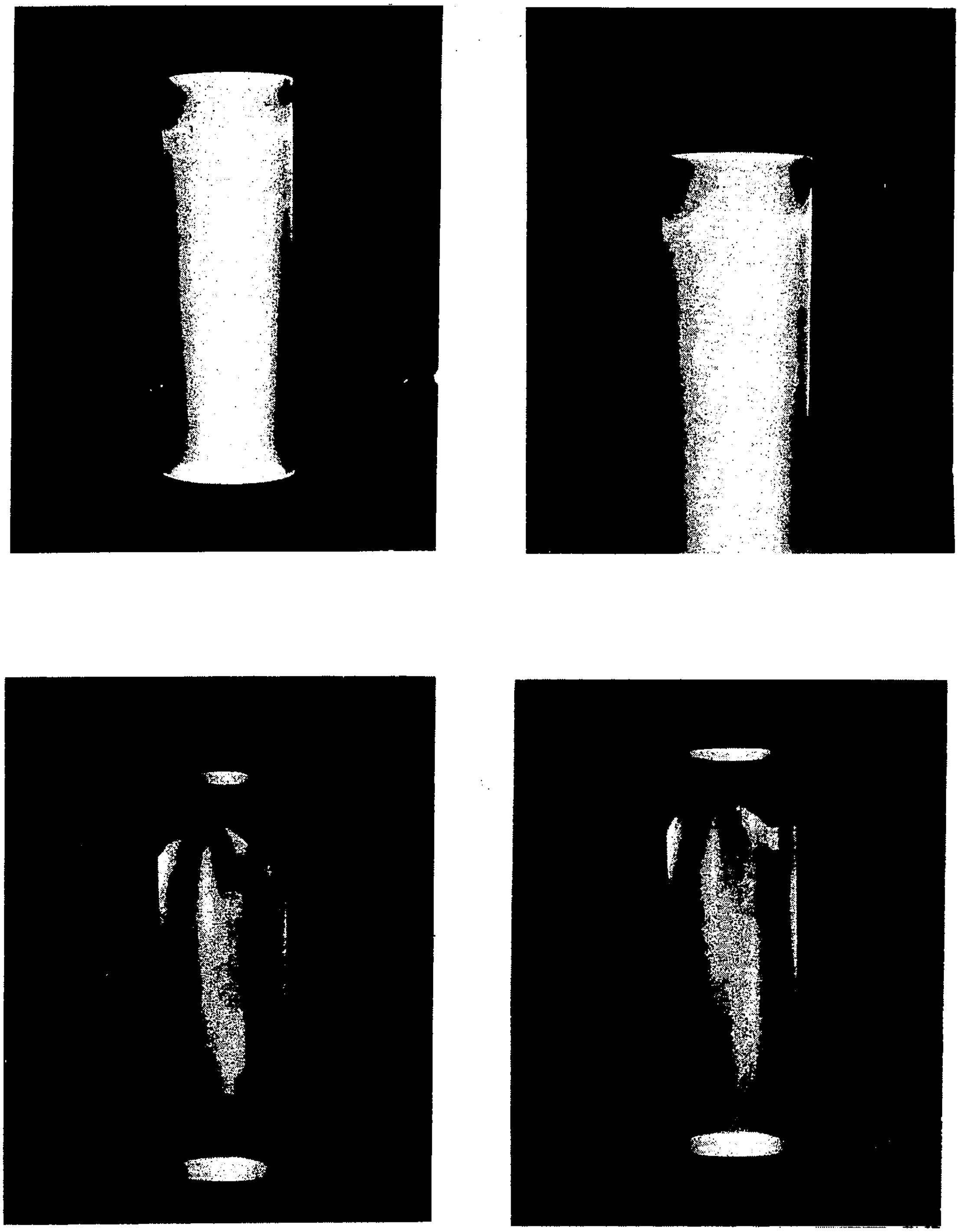

Fig. IV-5. Visible Degenerated Cavitons.

Figrue IV-6 Three dimensional sketch of X-ray pattern around the tube.

we would have to assume very strong field gradients at these boundaries. But, if such strong gradients exist, the generated x-rays would have to be collimated and even coherent to some extent, since all participating electrons are vibrating parallel to each other.

V. DESCRIPTION OF THE STATIONARY DISK-SHAPED ENRAD RESONANCE-PATTERNS IN TERMS OF CAVITONS

1. Derivation of the Fundamental Nonlinear Equation

In order to analyze the developed caviton, its stationary states, and their stability, we start from a set of three equations:

$$\frac{\partial \delta n_e}{\partial t} + \nabla[(n_o + \delta n_o)\vec{v}_e] = 0 \qquad (1.1)$$

$$(n_o + \delta n_o)\frac{\partial v_e}{\partial t} + (n_o + \delta n_o)\frac{e}{m}\vec{E} + \frac{T_e}{m}\nabla\delta n_e = 0 \qquad (1.2)$$

$$\nabla\cdot\vec{E} = -\ 4\pi e\ \delta n_e \qquad (1\text{-}3)$$

Here we have divided the electron concentration m into three components

$$n = n_o + \delta n_o + \delta n_e, \qquad (1.4)$$

where n_o is the average concentration of electrons balanced by the average ionic concentration in the discharge tube, δn_o is a very slow fluctuation, neutralized by an identical fluctuation in the ionic concentration (also including a large time-independent part defining the caviton), and δn_e is the fast fluctuation which cannot be followed by the ions. We have considered both δn_e and the velocity $\vec{v}_e$ of the electrons small and we have neglected terms quadratic in them. The first equation is the equation of continuity for the fast (jitter) motion, the second is the equation of motion expressing the momentum balance, with a field (drift) term and a pressure (diffusion) term included in addition to the linearized inertial term (T_e in energy units). Equation 1.3 is Poisson's equation. We neglect $\partial\delta n/\partial t$, i.e., consider δn time-independent.

We take the divergence of equation 1.2 and subtract the time-derivative of equation 1.1:

$$-\frac{\partial^{2}\delta n_{e}}{\partial t^{2}} + \frac{e}{m}\nabla\cdot[(n_{o} + \delta n)\vec{E}] + \frac{T_{e}}{m}\nabla^{2}\delta n_{e} = 0 \qquad (1.5)$$

Using equation 1.3 we obtain:

$$\nabla\cdot\left[\frac{\partial 2_{t}}{\partial t^{2}} + \frac{4\pi e^{2}}{m}(n_{o} + \delta n)\,\vec{E} - \frac{T_{e}}{m}\,\nabla(\nabla\cdot\vec{E})\right] = 0 \qquad (1.6)$$

A solenoidal part of the rectangular bracket does not make sense physically in our case. Neither does a harmonic potential part. Therefore we are looking for a solution satisfying the equation:

$$\frac{\partial^{2}E}{\partial t^{2}} + \frac{4\pi e^{2}}{m}(n_{o} + \delta n)\,\vec{E} - \frac{T_{e}}{m}\,\nabla(\nabla\cdot\vec{E}) = 0 \qquad (1.7)$$

We separate out the fast part of the variation in E(t):

$$\vec{E} = \frac{1}{2}\,\vec{E}_{o}(t)e^{-i\omega pt} + \text{c.c.}, \qquad (1.8)$$

where $E_{o}(t)$ is a slowly varying amplitude with a negligible second derivative implied, and c.c. is the complex conjugate of the preceding term. The average ponderomotive force of the electric field $\vec{E}(t)$ on the plasma of electrons and ions can be described by an average potential energy[1] (see also section 7).

$$U = e^{2}\left|E_{o}\right|^{2}/4m\omega^{2} \quad \frac{e^{2}}{2m\omega^{2}}\,\langle E^{2}\rangle\,, \qquad (1.9)$$

where the average <> is a time average. Denoting by T_{i} and T_{e} the ionic and electronic temperatures in energy units, we expect a Boltzmann distribution of the plasma density

$$n_{o} + \delta n = n_{o}e^{-U/(Ti + Te)} \qquad (1.10)$$

It is convenient to introduce the dimensionless field amplitude $A \equiv e\vec{E}_{o}/[2\omega\sqrt{m(T_{i} + T_{e})}]$. We obtain

$$2i\omega_p \frac{\partial \vec{A}}{\partial t} - \omega_p^2 \vec{A} + \omega_p^2 e^{-|A|^2} \vec{A} - \ell_D^2 \omega_p^2 \nabla(\nabla\cdot\vec{A}) = 0. \qquad (1.11)$$

The electron plasma frequency $\omega_p = (4\pi ne^2/m)^{1/2}$ and the Debye length $\ell_D = \sqrt{T_e/(4\pi ne^2)}$ define the dimensionless variables $\tau \equiv \omega_p t/2$ and $\bar{\rho} = r/\ell_D$. This yields the fundamental equation

$$i \frac{\partial A}{\partial t} + \nabla_\rho(\nabla_\rho\cdot\vec{A}) + (1 - e^{-|A|^2}) \vec{A} = 0 \qquad (1.12)$$

the stationary (steady state) solutions of this equation will be analyzed in the next section.

This equation is known as the nonlinear Schrodinger equation, which describes both the temporal evaluation and the stationary states of normalized field amplitude A.

As we shall see in the next section, Equation 1.12 admits stationary localized solutions similar to bound stated encountered in quantum mechanics. We will call these stationary localized states of the electric field "cavitons."

2. Stationary Solutions of the Fundamental Equation: Cavitons as Dynamic Equilibrium Configurations

Consider first the one-dimensional case

$$i \frac{\partial A}{\partial t} + \frac{\partial^2 A}{\partial z^2} + (1-e^{-|A|^2}) A = 0. \qquad (2.1)$$

This equation admits stationary solutions in which the dynamic pressure of the trapped electromagnetic field is balanced by a variation of the electron thermal pressure. These solutions, known as cavitons, are a special case of solitons, and have the form

$$A(z,\tau) = \mu(\xi)e^{ikz + i\omega\tau}, \ \xi \equiv z - 2k\tau. \qquad (2.2)$$

Equation 2.1 becomes now

$$\frac{d^2\mu}{d\xi^2} + (1 - e^{-\quad ^{2}} - w)\,\mu = 0; \quad w = \omega + k^2. \tag{2.3}$$

For the case of the small-amplitude ($u^2 << 1$) Langmuir soliton (caviton), we expand the exponential in series. We obtain in lowest order an equation studied by Zaharov[1], which presents a cubic nonlinearity

$$\frac{d^2\mu}{d\xi^2} + \mu^3 = w\mu. \tag{2.4}$$

This equation admits an exact solution

$$\mu(\xi) = C \operatorname{sech}(|C|\xi/\sqrt{2}); \quad w = |C|^2/2, \tag{2.5}$$

where C is an arbitrary complex constant. Indeed, equation 2.4 is satisfied if we substitute this "soliton" solution. Note that for any value of w in equation 2.3 or 2.4 only one solution is possible with the form seen in Figure 2.1. As we shall see, the situation is different, and more interesting in three dimensions, where the spherically symmetric solutions which are regular (finite) in the origin constitute a discrete set, with quantized radial slopes of the allowed solutions at $r = o$. Spatial dependence of the normalized field amplitude of the one-dimensional caviton. The dotted line is the low amplitude limit C sech $(C\xi/\sqrt{2}$. The full line is obtained by numerical integration with the use of the Runge-Kutta procedure. Spatial variation of the plasma density for $|C|^2 = 2$ in Figure 2.1. The spatial dependence of the plasma density in the one-dimensional caviton is calculated[2] in stationary conditions by using equation 1.10. The results are plotted in Figure 2.2 for the large-amplitude caviton with $|C|^2 = 2$ whose field is represented in Figure 2.1. Note that only 13.5% of the plasma density is left in the center of the caviton. For higher amplitude solutions this percentage will further decrease exponentially,

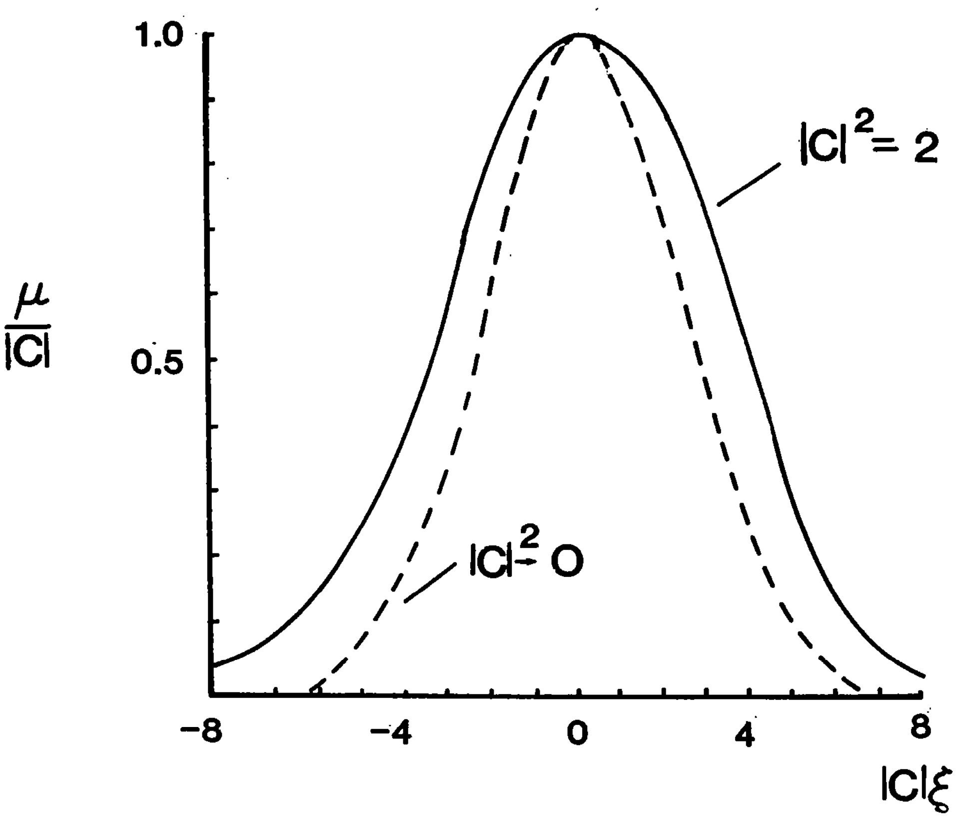

Figure 2.1 Spacial dependence of the normalized field amplitude of the one-dimensional caviton. The dotted line is the low amplitude limit C sech $(C\xi/\sqrt{2})$. The full line is obtained by numberical integration with the use of the Runge-Kutta procedure.

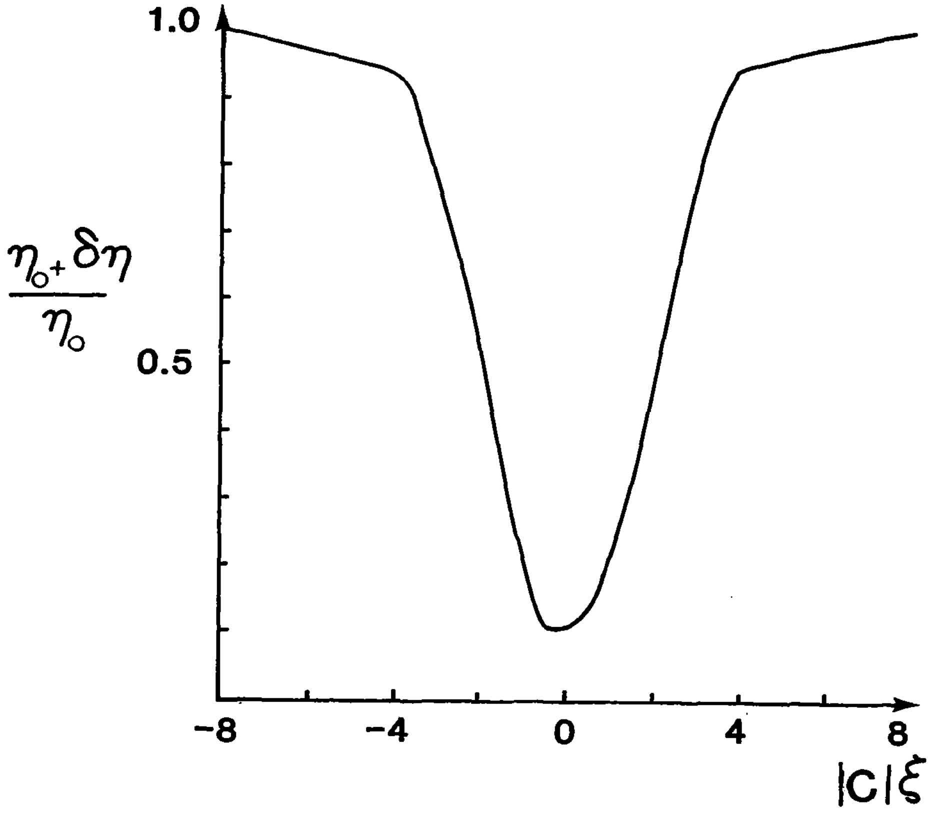

Figure 2.2 Spacial variation of the plasma density for $|C|^2 = 2$ in Figure 2.3/

according the equation 1.10 and 1.9, until a good vacuum is left in the caviton.

We consider now the three-dimensional, spherically symmetric Langmuir caviton. Equation 1.12 becomes

$$i\,\frac{\partial A}{\partial t} + \frac{1}{\rho^2}\frac{\partial}{\partial \rho}\left(\rho^2\,\frac{\partial A}{\partial_\rho}\right) - \frac{2}{\rho^2}\,A + \left(1-e^{-|A|^2}\right)A = 0$$

With the boundary conditions: A bounded for $\rho = 0$ and $A \to 0$ for $\rho \to \infty$, one obtains a discrete set of solutions with n = 1,2,3... modes or zeros of A between $\rho = 0$ and $\rho = \infty$.

The result of a numerical calculation[3] for the fundamental mode and the first "excited" mode are represented in Figure 2.3. The electric field points in the radial direction but vanishes in the origin and, for the case of nonfundamental caviton states, also on the nodal spheres.

For $\rho \to \infty$ the solution in Figure 2.3 decreases like spherical Bessel functions of order unity. The characteristic length of the high-field region is

$$L = \ell_D\,\omega_p/\omega = \left(\frac{T}{4\pi n_o e^2}\;\frac{4\pi n_o e^2}{m}\right)^{1/2}\omega^{-1} = \frac{T}{m}/\omega.$$

This means that the size of the caviton is independent of the surrounding plasma density n_o. For the electrons $T \cong 2000°K \cdot 1.38.10^{-16}$erg = 2.76 10^{-13} erg = 0.1725eV and with m = $0.9.10^{-27}$g we obtain $1.75.10^{7}$cm/s w^{-1}. This yields L = zcm for a frequency of 1.34 MHz which corresponds to the largest neutron output of ENRAD. The observed width of the dark space in ENRAD is approximately 1 cm, i.e., of the same order of magnitude as a Langmuir caviton.

The antinodal regions in Figure 2.3 correspond to spherical plasma-depletion layers similar to Figure 2.2, and the nodal spheres contain the

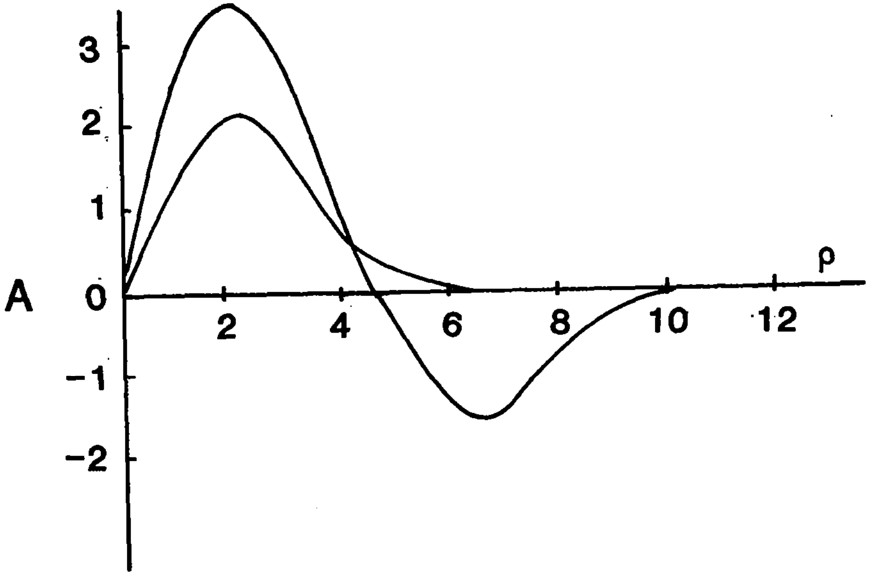

Figure 2.3 The normalized electric field $(\beta/2)^{1/2}E$ versus $\rho = \omega_r/\omega_o\lambda_D$, of the ground state and first excited electrostatic mode with spherical symmetry and with $\omega^2/\omega_p^2 = \frac{i}{2}$. The electric field is radial.

normal plasma concentration n_o. The similarity of spherical Langmuir soliton states to electronic states in atoms is particularly interesting.

The normalized electric field $(\beta/2)^{1/2}E$ vs. $\rho = \omega r/\omega_p \ell_D$, of the ground state and first excited electrostatic mode with spherical symmetry, and with $\omega^2/\omega_p^2 = 1/2$. The electric field is radial; $\beta^2 = e^2/k\pi m_e{}^2(T_e + T_i)$.

3. Electromagnetic Field Configuration and Plasma Generation in ENRAD

At the ENRAD operating frequencies of 0.5-1.7 MHz, the vacuum electromagnetic wavelength is 600m-176m. The distance between the ENRAD electrodes is between 5 and 50 cm, which is much smaller. Therefore, we can approximate the electric field configuration between the electrodes with a statis electric field.

Let the axis of the discharge tube be the z axis and the axial point 0, equidistant to the electrodes, be the origin of a system of rectangular (x,y,x) and cylindrical (r,θ,z) coordinates as shown in Figure 3.1.

First we obtain the electric field E in the vicinity of the origin 0 in the median plane z = 0 by summing the contributions of corresponding elements of arc dl' and dl" on the circumberence of the two electrodes of radius a = 10 cm, carrying a charge σ per unit length.

$$\vec{E} = \sigma \int d\ell \left[\frac{\vec{r}-\vec{r}'}{|\vec{r}-\vec{r}''|^3} - \frac{\vec{r}-\vec{r}''}{|\vec{r}-\vec{r}''|^3} \right] = - \sigma R \int \frac{d\ell}{(\vec{r}'^2+\vec{r}^2-2\vec{r}\cdot\vec{r}')^{3/2}}$$

$$\vec{E} = \frac{a\sigma\vec{R}^{\,2}}{(a^2+R^2/4)^{3/2}} \int_0^{\pi} d\theta \left[1 - \frac{3}{2}\, \frac{r^2-2ra\cos\theta}{a^2+R^2/4} + 7.5\, \frac{a^2r^2\cos^2\theta}{(a^2+R^2/4)^2} \right]$$

$$\vec{E} = \frac{-\,2\pi a\sigma\vec{R}}{(a^2+R^2/4)^{3/2}} \left[1 + \frac{\rho r^2}{a^2+R^2/4} \right] ; \quad \rho \equiv \frac{3.75a^2}{a^2+R^2/4} - \frac{3}{2}$$

Here we have used the equality $|\vec{r}-\vec{r}'|^3 = |\vec{r}-\vec{r}''|^3$ valid for $\vec{r}$ in the median plane, and $\vec{r}'-\vec{r}'' = \vec{R}$. The coefficient δ can be calculated for the distances 5 cm < R < 50 cm used in ENRAD. We obtain

R	5cm	$a\sqrt{6}$ = 24.5 cm	50 cm
ρ	2.03	0	-0.983

Consequently, the field distribution in the median plane z = 0 is characterized by a maximum in the origin for R > $a\sqrt{6}$ = 24.5 cm and by the pres-

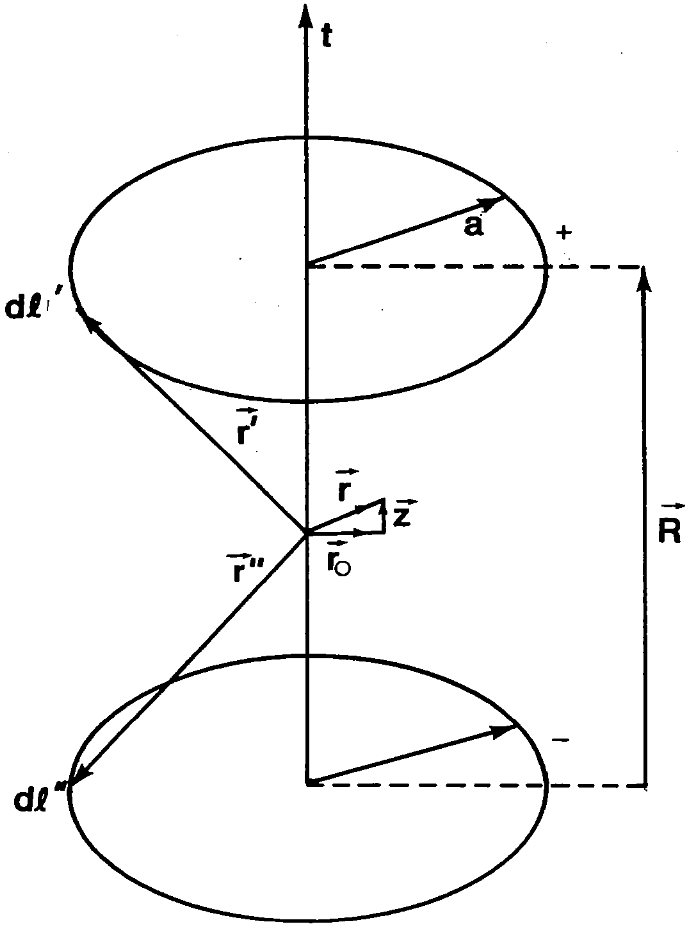

Figure 3.1 Calculation of ENRAD Electric Field.

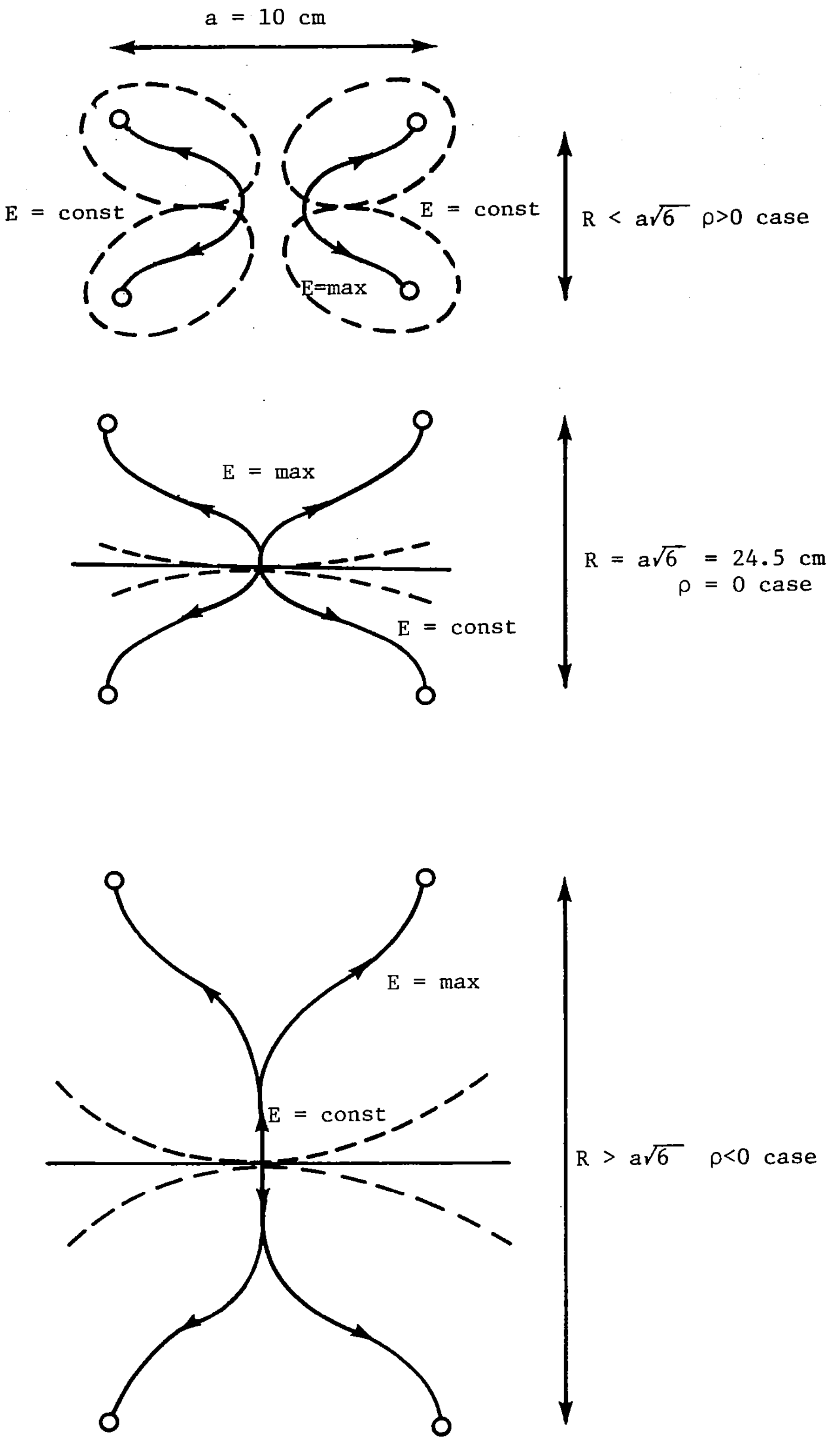

Figure 3.2 Geometrical locus of maximal elective field points in cross-sectional planes perpendicular to the axis of the ENRAD-device.

ence of a maximal circle with a minimum in the center 0 for $R > a\sqrt{6}$. For $R = a\sqrt{6}$ the field maximum in 0 is flat and of higher order, since all second derivatives of the field vanish.

The dependence of $E(r,z)$ on the cylindrical coordinate z and the radial field component can be determined in the vicinity of the origin by performing a more complete expansion of the first form in equation 3.1 or by using $\nabla \times E = 0$ and $\nabla \cdot E = 0$ with equation 3.3. Both methods yield, to second order,

$$E_z = -\frac{2\pi a\sigma R}{(a^2+R^2/4)^{3/2}} \left[1 + \rho\frac{r^2-2z^2}{a^2+R^2/4}\right]$$

$$E_r = -\frac{4\pi a\sigma R}{(a^2+R^2/4)^{5/2}}\,\rho rz$$

In three dimensions, the maximum observed in 0 for $R > a\sqrt{6}$ turns out to be a saddle point, both for E_z and for $\vec{E}^2$. The same holds true for the minimum observed in 0 on the $z = 0$ plane.

The main features of the whole field configuration are represented qualitatively in axial cross section on Figure 3.2 for the three cases considered. The maximal-field points obtained in any plane z = const generate a surface in three dimensional space. The cross section of this surface is represented in Figure 3.2 by full lines, and the median $|\vec{E}| = E|_{z=0,\max}$ = const. surfaces are dotted. The arrows indicate the direction in which $|\vec{E}|$ increases on these lines which are the geometrical locus of the points of maximal electric field lines. For $R \; a\sqrt{6}$ the locus of the maximal-field points is a cylindrically symmetric surface which resembles a rotational hyperboloid with one sheet. For $R = a\sqrt{6}$ the neck width of the rotational surface becomes zero and for $R \; a\sqrt{6}$ the locus consists of two distinct funnel-shaped surfaces connected by a line on their axis.

From the shape of the $|\vec{E}| = \max$ and $|\vec{E}| = \text{const}$ surfaces, we note that in the center of the ENRAD device there is an extended, quasi-homogeneous high-field region, separated from wall and electrode surfaces which are well known plasma recombination regions. Therefore, after the application of the high-frequency field in ENRAD, the highest plasma density is expected in the median ($z = 0$) plane.

The plasma frequency $\omega_p = (4\pi ne^2/m)^{1/2}$ increases together with the electron concentration n in every point after the high frequency field has been applied and after the first breakdown has occurred. In the process of plasma build-up, the increasing plasma frequency values $\omega_p(n)$ will first approach the value ω_o of the applied field in some point P on the median plane $z = 0$. As soon as ω_p approaches ω_o the dielectric constant of the plasma vanishes and since $\varepsilon E = \text{const}$, the electric field in the point P is enhanced (mathematically it approaches infinity). At this moment, a resonance between the electromagnetic wave and the electrostatic plasma oscillations characterized by ω_p occurs in the vicinity of the point P. As we shall see in the next section, this resonance leads to a dramatic enhancement of the electric field in the vicinity of P and to the process of linear conversion of electromagnetic waves into electrostatic (Langmuir) waves.

4. Electrostatic Resonance, Linear Conversion from Electromagnetic to Electrostatic Waves in ENRAD, and the Development of Localized Fields

In order to better understand the resonance process at the point P defined in the previous section, in which ω_p first approaches ω, we first review the elementary derivation of the electromagnetic wave dispersion relation and plasma dielectric constant. By applying the curl and a time derivative, respectively, to the two Maxwell equations

$$\nabla \times \vec{E} = -\frac{1}{c}\frac{\partial B}{\partial t}, \qquad (4.1)$$

$$\nabla \times \vec{B} = \frac{1}{c}\frac{\partial E}{\partial t} + \frac{4\pi}{c}\vec{j} \qquad (4.2)$$

we eliminate the $\nabla \times \; \partial B/\partial t$ term and obtain

$$\nabla \times (\nabla \times \vec{E}) = -\frac{1}{c^2}\frac{\partial^2 E}{\partial t} - \frac{4\pi}{c^2}\frac{\partial \vec{j}}{\partial t}$$

Taking $\vec{j} = ne\vec{v}$ and using the equation of motion

$$\frac{d\vec{v}}{dt} = \frac{e}{m}\vec{E}$$

we obtain with $\nabla\vec{E} = 0$

$$-\nabla^2\vec{E} = -\frac{1}{c^2}\frac{\partial^2\vec{E}}{\partial t^2} - \frac{4\pi ne^2}{mc^2}\vec{E}$$

Substituting $E = E_o e\ i(\vec{k}\ \vec{r} - \omega t)$ we obtain the dispersion relation

$$\omega^2 = \omega_p^2 + c^2k^2$$

and the phase velocity

$$v_{ph}^2 = \frac{\omega^2}{k^2} = \frac{c^2}{1-\omega_p^2/\omega^2} \equiv \frac{c^2}{\varepsilon} .$$

This identifies the index of refraction $\varepsilon^{1/2}$ and the dielectric constant of the plasma

$$\varepsilon = 1 - \omega_p^2/\omega^2 .$$

Similar results obtained by replacing c^2 with 3kT/m in equation 4.5 and 4.7, holds for Langmuir waves (see Section 6). Consider the ENRAD discharge right after the high frequency field has been applied, when the density n of electrons (and ions) starts to increase and the plasma frequency in the z = 0 plane approaches the frequency ω_o of the applied field. Along the discharge tube we have roughly $\vec{E} \cong \vec{E}_z$

$$\vec{D} = \varepsilon\vec{E} = \text{const.}$$

The electric field configuration is close to a static configuration with the field lines directed along the axis, between the electrodes. Assuming that ω_p approaches ω_o in a cross-sectional plane close to the median, we expect an enhancement of the electric field

$$\vec{E} = \frac{\vec{D}}{\varepsilon} = \frac{\vec{D}}{1 - \omega_p^2/\omega^2}$$

in this layer. The enhancement factor is $1 - \omega_p^2/\omega^2$. This enhanced field will further increase the degree of ionization and consequently ω_p will reach the value ω_o. Note that the energy density $ED/8\pi$ is also increased in the resonance layer. Since the amplitude of D is constant, i.e., the same as outside the layer, the swelling in the energy density is proportional to that observed in the electric field amplitude.

The increased electric field in the resonant layer will excite electrostatic (Langmuir) waves. Indeed, the enhanced field $\vec{E}$ will accelerate electrons in the $-\vec{E}$ direction, creating a compression region (accumulation) on the -E side of the resonant layer and a depletion region on the $+\vec{E}$ side. Due to the electrostatic repulsion between the compressed electrons on the $-\vec{E}$ side, and due to the pull of the uncompensated positive ions on the $+\vec{E}$ side, the electrons will rebound after $T_p/2 = \pi/\omega_p$, i.e., after a half-period of the Langmuir wave. Indeed, this electrostatic push-pull is the restoring force of the electrostatic waves in a plasma. Due to the equality $\omega_p = \omega_o$ the applied electric field will have changed its direction from $\vec{E}$ to $-\vec{E}$ in the same time. Therefore, the electrons will be accelerated again during their rebound. The enhanced electric field thus continuously builds up the plasma oscillations by acting on the electrons with the right phase at resonance. The electrostatic oscillation would increase indefinitely in amplitude, like a lossless resonator, if there were no energy-loss processes and non-linear phenomena saturating the amplitude at some very high values, e.g., 2 or 3, orders of magnitude above the applied electric field amplitude level. Such processes are:

A. Generation of Langmuir waves which propagate away from the resonant layer in both directions. The coupling of the electromagnetic field to these waves is given by the excitation of electrostatic waves by the enhanced electric field which is in the resonant layer, part both of the electromagnetic and electrostatic wave. This excitation, described in detail above is limited to the resonant layer, because the resonance condition $\omega_p - \omega_o$ is only satisfied in this layer. The coupling is linear, and therefore we speak about linear conversion from EM to ES waves. The Electrostatic waves generated in this layer propagate down the plasma density gradient adjoining the layer in both axial directions, with increasing group velocity $v_{ges} = c_{se} [1 - \omega_p^2(z)/\omega^2]^{1/2}$, decreasing energy density by the same factor, and decreasing wavelength $\lambda = (2\pi/c_{se})$ $[1 - \omega_p^2(z)/\omega^2]^{-1/2}$, where $c_{se} \cong (3kT_e/m_e)^{1/2}$ is the effective electronic sound velocity. The electromagnetic energy streams into the resonant layer along the field lines of the Poynting vector $(c/4\pi)\vec{E}x\vec{B}$ at the speed of light and leaves the layer at the much lower speed v_g of the order of the electronic thermal velocity, in form of Langmuir waves. Energy flux conservation requires then that the electrostatic energy density in the Langmuir wave must be larger than the electromagnetic energy density by the ratio of these speeds, i.e.,

$$\frac{v_{gem}}{v_{ges}} \quad \frac{c(1-\omega_p^2/\omega^2)^{1/2}}{c_{se}(1-\omega_p^2/\omega^2)^{1/2}} = c/c_{se} \approx 3.10^{10}\text{cm/s}/3.10^{7}\text{cm/s} = 10^3$$

This energy enhancement is equivalent to an additional increase of the electric field amplitude by $1\frac{1}{2}$ orders of magnitude, actually only a factor of 10 in addition to the enhancement due to the $(1-\omega_p^2/\omega^2)^{-1}$ factor. The physical reason for this increase in the energy density is the kinetic energy of the electrons in the Langmuir wave and the electrostatic energy of the charge density accumulations in the Langmuir wave, both contributing equal amounts in average. The actual factor is reduced to 10 due to the competition of other energy loss process, listed below.

B. Charged particle acceleration - to be discussed in detail in Section 8, leads to transit damping[4]: suprathermal electrons are accelerated by passing through the resonant layer with the right phase. In addition, as we shall see in the next section, the ponderomotive force of the enhanced electric field acts on the plasma and digs a cavity leading to the creation of an electrostatic caviton. This large density perturbation corresponds to a localized ponderomotive potential (see section 7) which also contributes to the acceleration of electrons and ions observed experimentally in ENRAD. Fast electrons and ions carry out about equal amount of power, as we shall see.

C. Resistive (ohmic) heating in the walls of the density cavity.

D. Generation of ion-acoustic waves and of other oscillations of the plasma. These processes are based on the coupling between various resonant modes of the plasma. If two modes are involved, of frequencies $_1$ and $_2$ and wave numbers $\vec{k}_1$, and $\vec{k}_2$, the relations $\omega_o = \omega_1 + \omega_2$ and $\vec{k} = \vec{k}_1 + \vec{k}_2$ must be satisfied.

The enhanced electric field present in the resonant layer initiates the linear conversion from EM to ES waves on a short time scale[4] of the order of 10 periods of the electronic plasma frequency ω_p, determined essentially by the inertia of the electrons. The subsequent development of a density minimum in the resonant layer is about two orders of magnitude slower, i.e., of the order of 10 periods of the ion plasma frequency

$\omega_{pj} = (4 n_i e^2/m_i)^{1/2}$, where n is the ion concentration and m their mass.

5. Formation of Cavitons in the Nonlinear ENRAD Regime

The strongly enhanced electric field present in the resonant region with $\omega_p = \omega_o$ exerts a ponderomotive force $F \cong - \nabla <E^2>/8\pi$ per unit volume on the plasma, thereby creating a density cavity in the resonant layer. This density cavity is favorable to the further trapping of electromagnetic field, reducing the convective loss of electromagnetic and Langmuir wave energy. This trapping results in an even higher field inside the cavity, which in turn creates a deeper cavity. This process continues in a self-consistent way until saturation caused by nonlinear phenomena sets in. This final stationary state obtained this way is a combined nonlinear field and plasma state known as caviton, a particular case of solitons well known in many nonlinear physics problems. As we have seen in section 2, the electric field inside the caviton is very similar to the quantum-mechanical wave function defined inside a potential well which corresponds to the density cavity in our case. The splitting of a single caviton with formation of two cavitons when the pressure is slowly raised in the ENRAD discharge is similar to the transition from the ground state to the first excited state of a sequence of energy levels in quantum mechanics. As we have seen on the example of the numerically calculated spherical caviton, this feature is obtained also theoretically on the basis of the nonlinear "Schrödinger" equation derived in section 1. The nonlinearity is due to the interaction of the field with the plasma. The n^{th} excited state has n nodal spheres.

In the case of the ENRAD device, the ground state corresponds to one dark space in the z = 0 plane bounded by a pair of luminous disks. The dark space is the high field region in the caviton and the two disks are the walls of the density cavity, made luminous by the excitation of atoms under the influence of mainly electronic bombardment and also ionic bombardment caused by the high electric field. In fact the luminous disks arise from the plasma distribution partially penetrating into the high field region and adjacent plasma sheets extending into the background gas as in Figure 5.1. In the high field region, inside the caviton, the concentration of exicted ions and neutral atoms is very low, and therefore this region appears dark to the eye.

The excited state of number n represents a sequence of n high-field regions in ENRAD, each of them limited by two luminous disks.

Figure 5.1 is disk-shaped plasma cavitons obtained in the ENRAD device: a) distribution of the squared electric field amplitude; b) distribution of the total plasma and gas pressure, $p = n_e kT_e + n_i kT_i + n_D kT_D + n_{D_2}+kT_{D_2} + N_{D_2} kT_{D_2}$; c) distribution of the light output in the blue and red spectrum areas, and the total luminosity; and d) distribution of the total plasma concentration $n = 1/2(n_e+n_i+n_{D_2}+)$.

Figure 5.1 Explanation of the Observed Color Distribution.

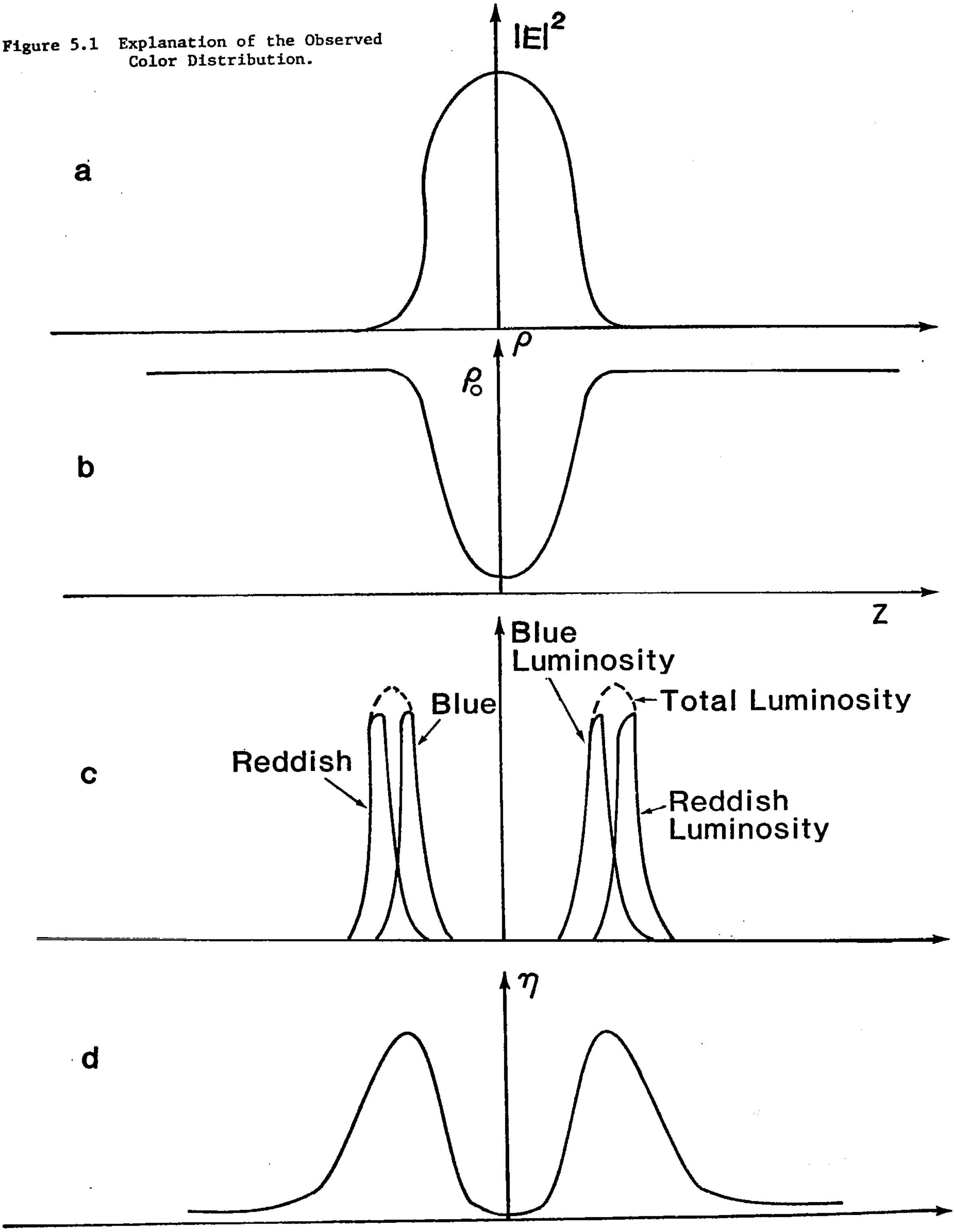

6. Derivation of the Electrostatic (Langmuir) Waves

We have repeatedly used the concept of electrostatic waves and the expressions of their group velocity and phase velocity in the present chapter. The plasma caviton comprises, in essence, a standing, localized wave of this kind. Therefore, we include here a brief derivation of electrostatic waves in plasmas, which may be skipped by the reader who is familiar with the subject.

Starting with the generalized Ohm's law

$$\frac{m}{ne^2}\frac{\partial j}{\partial t} = \vec{E} + \frac{\vec{v}}{c} \times \vec{B} + \frac{1}{en}\nabla p_e - \frac{1}{cne}\vec{j} \times \vec{B} - \eta\vec{j} \qquad (6.1)$$

where $\vec{j}$ is the current density and η is the resistivity, we take $\vec{B} = 0$, and consider small, fast, fluctuations of the electron pressure

$$\delta p_e = \gamma k T_e \nabla \delta n = - 3 \frac{kT}{e}\nabla\rho = - \frac{m}{e} v_{th}{}^2 \nabla\rho, \qquad (6.2)$$

where $v_{th}{}^2 \equiv 3\, k\, Te/m$, and the adiabatic coefficient $\gamma = (s/z + 1)/(s/2) = 3$. The number of degrees of freedom s has to be taken = 1 since the fluctuations are faster than the collision time and the motion is, therefore, adiabatic and one-dimensional. The fast fluctuation ρ of the electronic charge density satisfied the continuity equation for the fast fluctuations

$$\frac{\partial\rho}{\partial t} + \nabla(\delta\vec{j}) = 0 \qquad (6.3)$$

allows us to eliminate $\delta\vec{j}$ from the variation of Equation (6.1) by applying the divergence:

$$\frac{\partial^2\rho}{\partial t^2} + w_p{}^2\rho - v_{th}{}^2\nabla^2\rho + \nu\frac{\partial\rho}{\partial t} = 0 \qquad (6.4)$$

Here ν is the frequency of collisions $\nu = ne^2/m$, and $\omega_p{}^2 = 4\pi ne^2/m$ is the squared plasma frequency. Note that Equation (6.4) differs from Equation (1.5) only by the additional presence of the dissipative collisional term with ν. The corresponding dispersion relation for plane wave solutions substituted into Equation (6.4) is

$$\omega^2 = \omega_p^{\,2} + v_{th}^{\,2}\,k^2 - i\omega\nu \qquad (6.5)$$

Therefore, if we neglect the small dissipative (damping) term are obtain the phase velocity

$$v_{ph}^{\,2}\,(e\;) = \frac{\omega^2}{k^2} = \frac{\omega_p^{\,2}}{k^2} + v_{th}^{\,2} - iv_{ph}\,\frac{\nu}{k} \simeq \frac{v_{th}^{\,2}}{1-\omega_p^{\,2}/\omega^2} \equiv v_{th}^{\,2}/\varepsilon, \qquad (6.6)$$

where ε is the dielectric constant defined in Equation (4.8). The group velocity v_g is given by

$$v_g(e\;) \quad \frac{\partial\omega}{\partial k} \simeq \frac{v_{th}^{\,2}k}{\omega_p^{\,2} + v_{th}^{\,2}\,k^2} = \frac{k}{\omega}\,v_{th}^{\,2} = \frac{v_{th}^{\,2}}{v_{ph}(e\;)} = v_{th}\quad 1 - \frac{\omega_p^{\,2}}{\omega^2} = v_{th}\sqrt{\varepsilon}$$

$$(6.7)$$

Note that Equations (6.5)-(6-7) turn into the corresponding equations (4.6) and (4.7) applicable for electromagnetic waves, if we replace v_{th} by c, the speed of light in vacuum. In particular, the group velocity of electomagnetic waves is

$$v_g(\text{em}) = c\,\frac{k}{\omega} = \frac{c^2}{v_{ph}(\text{em})} = c\quad 1 - \frac{\omega_p^{\,2}}{\omega^2} = c\,\sqrt{\varepsilon} \qquad (6.8)$$

7. Derivation of the Ponderomotive Potential

The concept of the ponderomotive potential used in the previous sections arises in a natural way, if we consider separately the fast motion of the electrons at frequencies of the order of the plasma frequency, and the slow motion in which both electrons and ions participate.

The high frequency (jitter) velocity of the electrons is given by the equation of motion

$$-i\omega\vec{v}_e = -\,(e/m)\vec{E} \qquad (7.1)$$

which produces an additional meansquare velocity

$$<v_e^2> = (e/m\omega)^2 <E^2>. \tag{7.2}$$

This corresponds to an additional pressure contribution p_{eff}

$$p_{eff} = (1/2)\ n_e m<v_e^2> = (1/2)(n_e e^2/m\omega^2)<E^2> = \frac{<E^2>}{8\pi} \tag{7.3}$$

In turn, this effective pressure causes a force $-\nabla p_{eff}$ per unit volume. If we divide by the concentration of electrons n, we obtain the average force per electron

$$m\frac{dv_R}{dt} = -\nabla\frac{e^2<E^2>}{2m\omega^2} = -\nabla\frac{<E^2>}{8\ n_e} \equiv -\nabla U, \tag{7.4}$$

where v_o is the slow component of the electron (and ion) velocity in which the jitter has been averaged out. The form with n in the denominator is applicable in the case of a plasma caviton, for which $\omega^2 = \omega_p^2 = 4\pi n_e e^2/m$. The potential energy U from which the ponderomotive force can be derived is thus identical to equation (1.9)

$$U \equiv \frac{e^2<E^2>}{2m\omega^2} = \frac{<E^2>}{8\pi n_e}, \tag{7.5}$$

also known as the slow pseudopotential, felt only by the electrons. The electrons tend to assume a Boltzmann distribution $n_e = n_o e^{-U/kT_e}$, but the ions pull them back partially, through the amibpolar potential ϕ and a corresponding ambipolar electric field $-\nabla\phi$, which always appears if electrons and ions are acted upon with different forces. The ambipolar potential ϕ restores electric quasineutrality, and we obtain a distribution of the electron and ion concentrations

$$n_e = n_o e^{-\frac{U-e\phi}{kT_e}} = n_i = n_o e^{-\frac{e\phi}{kT_i}} \tag{7.6}$$

From the equality of the two exponents in Equation (7.6) we infer that

$$\frac{U-e\phi}{T_e} = \frac{e\phi}{T_i} = \frac{U}{T_e+T_i} \quad . \tag{7.7}$$

This yields the final form of the spatial dependence of the carrier concentration

$$n_e = n_i = n_o e^{-\frac{T}{k(T_e+T_i)}} \tag{7.8}$$

which has been used in Equation (1.10).

VI. SUMMARY AND CONCLUSIONS

During the effort reported herein, investigation concerning the properties of a radiofrequency discharge of a special configuration, called ENRAD, were made. The results obtained were compared to measurements previously obtained with a pulsed high voltage discharge employing the same configuration.

The observations made during these investigations are summarized as follows:

1. Emission of neutrons by the RF discharge was observed.
2. Indications of some weak x-ray emission were also obtained.
3. A visible plasma structure consisting of pairs of disks separated by a dark sheath was observed.

A model to explain the observed phenomena was proposed. This model describes formation of plasma cavitons caused by "digging in" of the applied RF field. The condition for this to occur is that the applied frequency is equal to the plasma frequency.

The caviton is a plasma region of drastically reduced density surrounded by steep gradients in electric field and charge carrier density. Charged particles trapped inside the caviton can obtain high energies due to these field gradients. They may escape from the caviton and bombard the surrounding high particle density walls. The resulting collisions are sufficiently energetic to cause nuclear reactions to take place. It is concluded that one of these reactions is the DD reaction causing neutrons to be emitted.

There is some experimental evidence these nuclear reactions take place, especially during the collapse of the cavitons. This is concluded from the fact that introduction of small concentrations of nitrogen into the discharge increase the neutron yield.

It is also concluded that in principle these cavitons are capable of emitting collimated, maybe even coherent, x-rays. This could be especially shown for cavitons formed at higher voltages.

The conclusion is that the ENRAD configuration is a plasma containment which is capable of producing nuclear reactions at high particle densities and low temperatures. The applied electric fields are modest.

REFERENCES

II.1 "Breakdown and Maintenance of Microwave Discharges in Argon," by S. Krasik, D. Alpert and A. McCourvey, Phys. REv. 76, 722 (1949).

IV.1 "Measurement of the Time Averaged Potentials in Low Pressure, rf Discharges Using an Ion-Beam Probe," by A. Miller, C. W. Bruce and M.D. Kregel, J. Appl. Phys. 39, 1853-1856 (1968).

V.1 V.E. Zaharov, Zh. Eksp. Teor. Fiz. 62, 1745 (1972) or Sov. Phys. J.E.T.P. 35, 908(1972).

V.2 M. D'Evelyn and G.J. Morales, Phys. Fluids 28, 1997 (1978).

V.3 J. Zitkova Wilcox and T.J. Wilcox, Phys. Rev. Lett. 34 1160 (1975).

V.4 H.C. Kim, R.L. Stensel, and A.Y. Wong, Phys. Rev. Letters 33, 886 (1974); 32, 659 (1974).

V.5 G. Morales and Y.C. Lee, Phys. Rev. Lett. 33, 1016 (1975).

APPENDIX A

Measurement of Activation Caused by Neutrons Emitted by the ENRAD Device

by

Dr. William H. Ellis*
Consultant to RTS Laboratories, Inc.

Fall, 1981

*Address: Department of Nuclear Engineering Sciences
University of Florida
Gainesville, Florida 32611

A series of radioactivity measurements have been performed for a number of high purity gold and indium foils which have been placed into positions around the deuterium gas discharge device for varying periods of time while the device was operated. The objective of the measurements was to monitor the device for neutron emission, which had been reported by others; having been deduced from evidence attributed to neutron interactions in detector media or radioactivation of metallic detector foils or disks (coins) which were subsequently counted.

The detector system used in the measurements, as shown in block diagram form in Figure 1, consisted of well-shielded, high efficiency beta-gamma scintillation detectors with attached instrumentation combined into a beta-gamma absolute coincidence spectrometer. The beta detector was CaF_2 scintillation crystal, while the gamma detector used was a NaI(Tl) scintillation crystal. Beta and gamma ray singles counts (N_β, N_γ) and beta-gamma coincidence counts $N_{\beta\gamma}$ (or counting rates) were measured with single channel and coincidence analyzers, while at the same time, the ungated and gated gamma ray pulse height (energy) distributors were measured with a multichannel pulse height analyzer.

The beta-gamma coincidence system as described, and shown in the figure, was selected to provide a high degree of selectivity for ^{198}Au, through its 100% branching through the beta-gamma cascade and the systems ability to probide a direct value for the ^{198}Au source strength N_D, i.e., $N_\beta \cdot N_\gamma / N_{\beta\gamma} = N_D$.

Radioactivation of pure indium and gold, such as the foils used, would form two general types of radionuclides, depending on the energy group characterizing the neutrons; one for thermal and the other for fast neutrons.

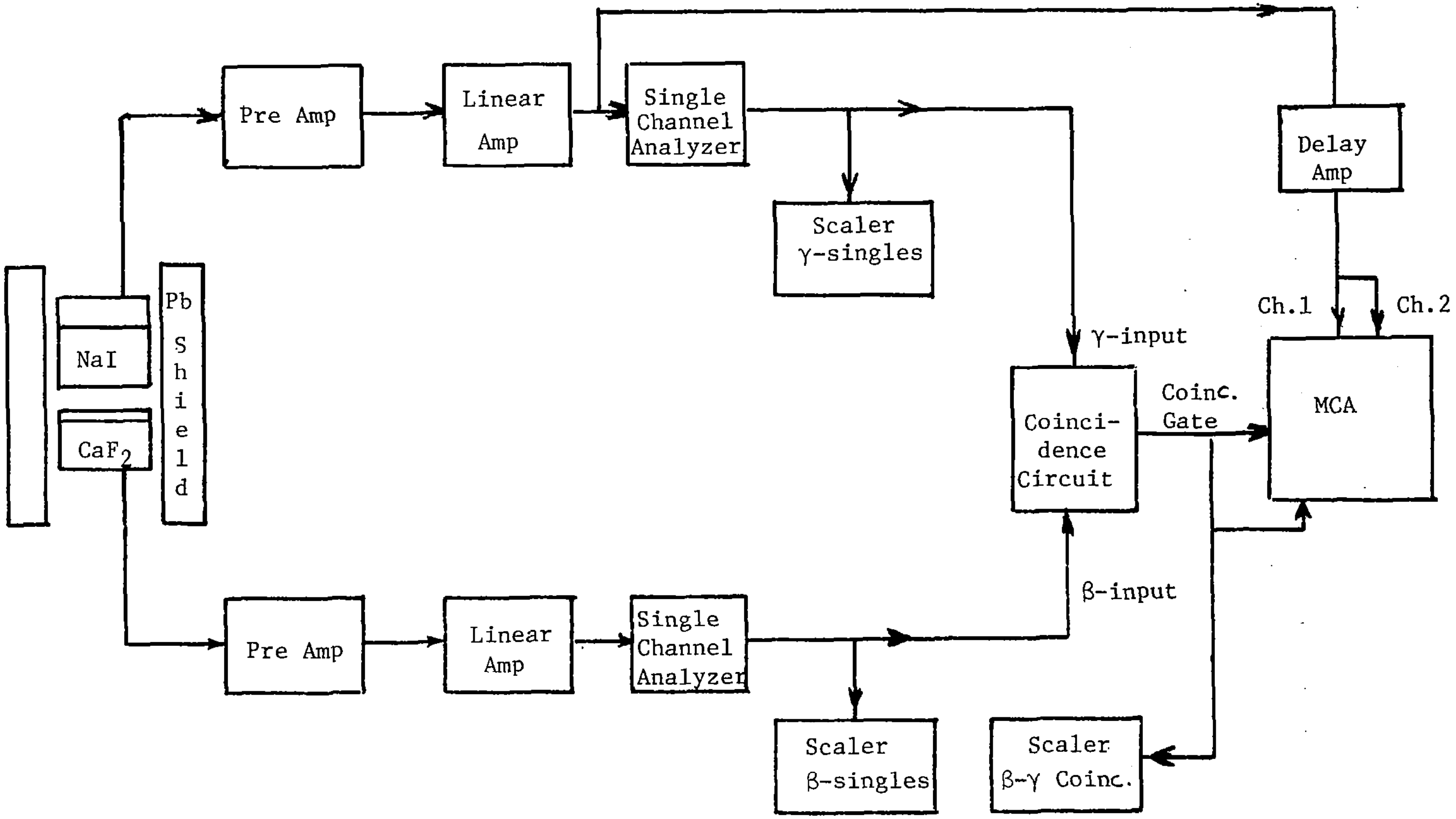

FIGURE 1 BLOCK DIAGRAM OF ELECTRONICS USED WITH THE β-γ-SPECTROMETER

The thermal neutron group, in general, form γ or negatron decay species, through the (n, γ) reaction, while the fast neutron group form either electron capture (EC) or positron decay radionuclides by the (n, 2n) reaction.

The principal (n, γ) species formed for In and Au are the 54-minute ^{116m}In and the 2.7-day ^{198}Au radionuclides. The former emits several gamma rays following its negatron decay with energies (% branching) at 4.7 (36%), 819 (17%)m 1090 (53%), 1293 (80%) keV, while the latter exhibits only one gamma ray at 411 keV (100%).

The (n, 2n) fast neutron induced reaction products for In would be derived from

(4.23%)^{113}In(n, 2n)^{112m}In(20.7 min) IT(156 keVγ)

^{112}In(14.4 min., β^-(44%), β^+(22%), EC (34%)

511 keVγ (44%)
617 keVγ (6%)

and

(95.77%) ^{115}In(n, 2n)^{114m}In(50-day) IT(96.5%)(191.6 keVγ's)
EC(3.5%) 724, (58 keVγ's)

^{114}In(72 sec.) β^- (98%), β^+ (.004%), 1299 keV (.2%)

Gold (n, 2n) reaction products are those of ^{196}Au and ^{196m}Au:

(100%)^{197}Au (n, 2n) ^{196m}Au (9.7hr) IT (175 keVγ)

^{196}Au (6.1 day) β^-(6%)-426 keV γ-ray EC (93%) 688.7
(26%), 355.7 (67%) keVγ's
β^+(5 x 10^{-5}%)

A common component introduced into gold coins is copper, which forms and (n, γ) 12.8 hour ^{64}Cu positron activity (β^+ 19%) by means of thermal neutron absorption. The fast neutron group would also produce the same positron activity, but would, in addition produce 9.76-minute ^{62}Cu, i.e.,

(30.9%)^{65}Cu (n, 2n)^{64}Cu (12.8 hr.) β^-(38%) - no gamma rays; EC (43%) -
1340 keVγ (.5%); β^+(19%) - 511 keV
annihilation gamma.

(69.1%) ^{63}Cu (n, 2n) ^{62}Cu(9.76 min.) β^+ (97%) - 511 keV annihilation gamma.

Thus, in general, positron annihilation observed in the decay of pure indium is possible but for gold it would have to be due to activated impurities, one of which could be copper, which could be produced with either thermal or fast neutrons. The shorter lived copper radionuclide ^{62}Cu(9.7m) would be indicative of fast neutron activation since it can be produced only by the fast neutron (n, 2n) reaction.

The first radioactivity measurements were made with a gold coin, several gold foils and several indium neutron detector foils, which had been placed around and near the discharge device for approximately 12 hours of operation. The gold, having a lifetime of 2.7 days, would allow for longer counting times, while the indium foils with a lifetime of 54 minutes, should provide higher counting rates for shorter activation periods.

For the first measurements the discriminator for the CaF_2 beta ray detector was adjusted high enough to exclude output pulses due to ^{198}Au gamma ray interations in the thin CaF_2 detector. This assured only beta-gamma gold coincidence counts could occur. Even though a low level background due to ^{137}Cs gamma rays was observed in the ungated singles gamma spectrum, the gated (coincidence) spectrum, however, was essentially free of effects due to the ^{137}Cs gamma rays.

A series of background counts for comparison were obtained prior, during, and after the initial measuremtns. The Au and In foils were counted before and after their exposure to the operating deuterium discharge. After a delay due to cross-town transport, the In foils were counted first due to their shorter lifetime (54 min.), with the longer lived ^{198}Au (2.7 days) being held for later counting. The first counts were for 10-minutes, however the total counts obtained were marginal for satisfactory statistical evaluation. To improve counting statistics, the In foils were combined (as were the Au foils later) and the counting interval was extended to 40 minutes. The counting schedule is summarized in Figure 2. The obtained results are plotted in Figures 3, 4, and 5, along with the background counting results.

The first of the indium foils counted, In #002, exhibited counting rates approximately equal to the average values of the background. However, the next two foils counted, numbers 001 and 003, both exhibited counting rates considerably (significantly) above the background average values. Also, when these foils were combined with #002 and counted for a period of 40 minutes, the counting rates observed were again above the considerably average background values.

When the smoothed (3-point) spectra, obtained simultaneously with the counting rate data, as well as that of the background are viewed, each is observed to exhibit spectral features at approximately channels 38 and 75, where the latter peaked feature has previously been shown to be due to the 662 keV gamma ray from a ^{137}Cs contribution of the counter-shield system. (See Figure 6) Based on using the ^{137}Cs peak as an internal standard, the centroid, or central channel of the peak distribution, of the other peaked features is shown to fall at approximately 340 keV. In addition to these features, which appeared in the background spectrum, indium foils numbered 001 and 003 exhibited additional features centered at approximately channels 46-48 and 55-56, respectively, while the combined foil 40-minute spectrum exhibited the peak at channels 46-48. (See Figure 8)

A separate measurement performed with an indium foil which had been activated by exposure to a thermalized 5 Ci Pu-Be source yielded a peak centroid for the 417 keV gamma ray of ^{116m}In(54 min.) at channel 46. A gamma ray spectrum acquired with a ^{22}Na source yielded a peak centroid for the 511 keV positron annihilation peak at approximately channels 74-76. (See Figure 8)

FIGURE 2

FOIL DETECTOR COUNTING SCHEDULE

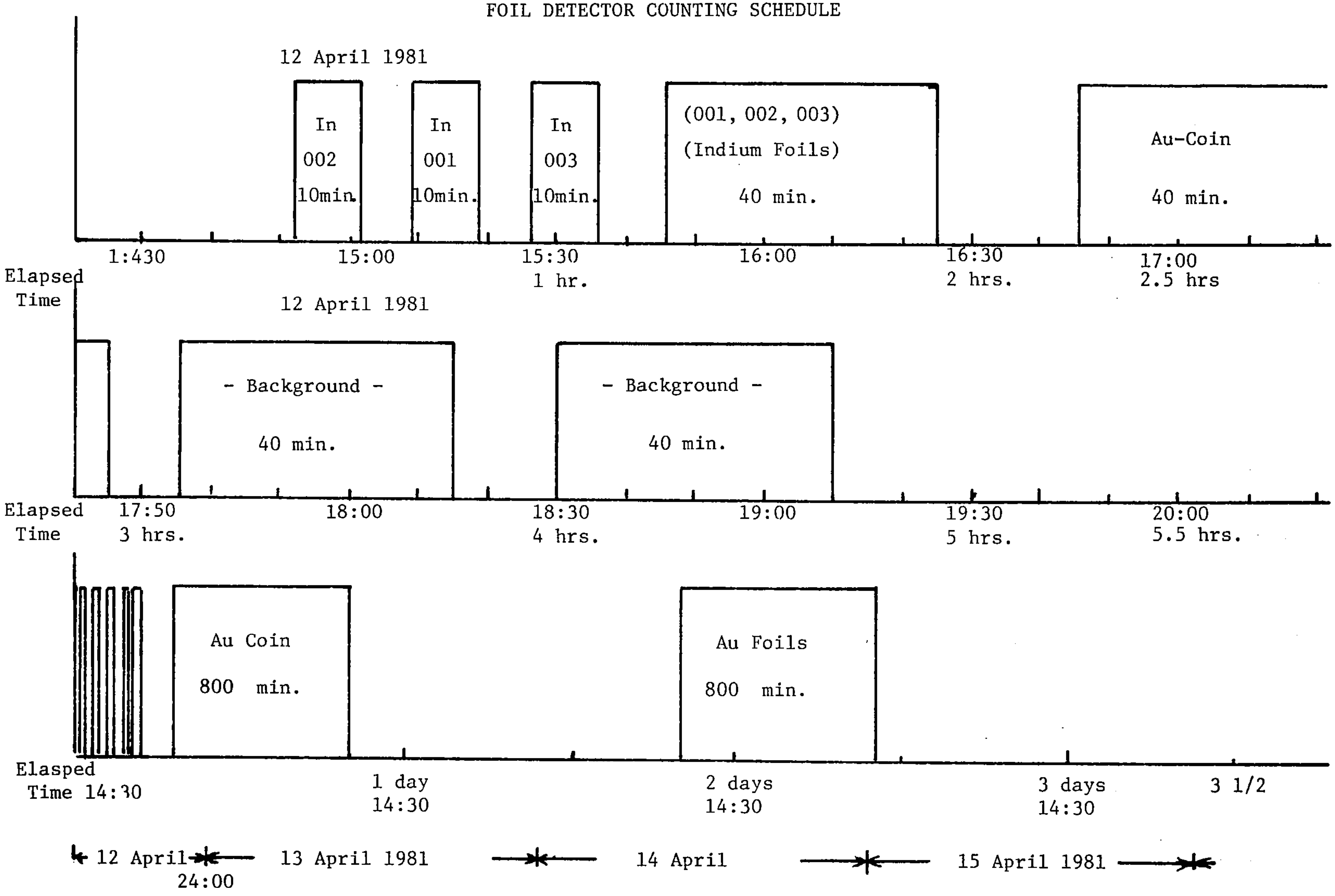

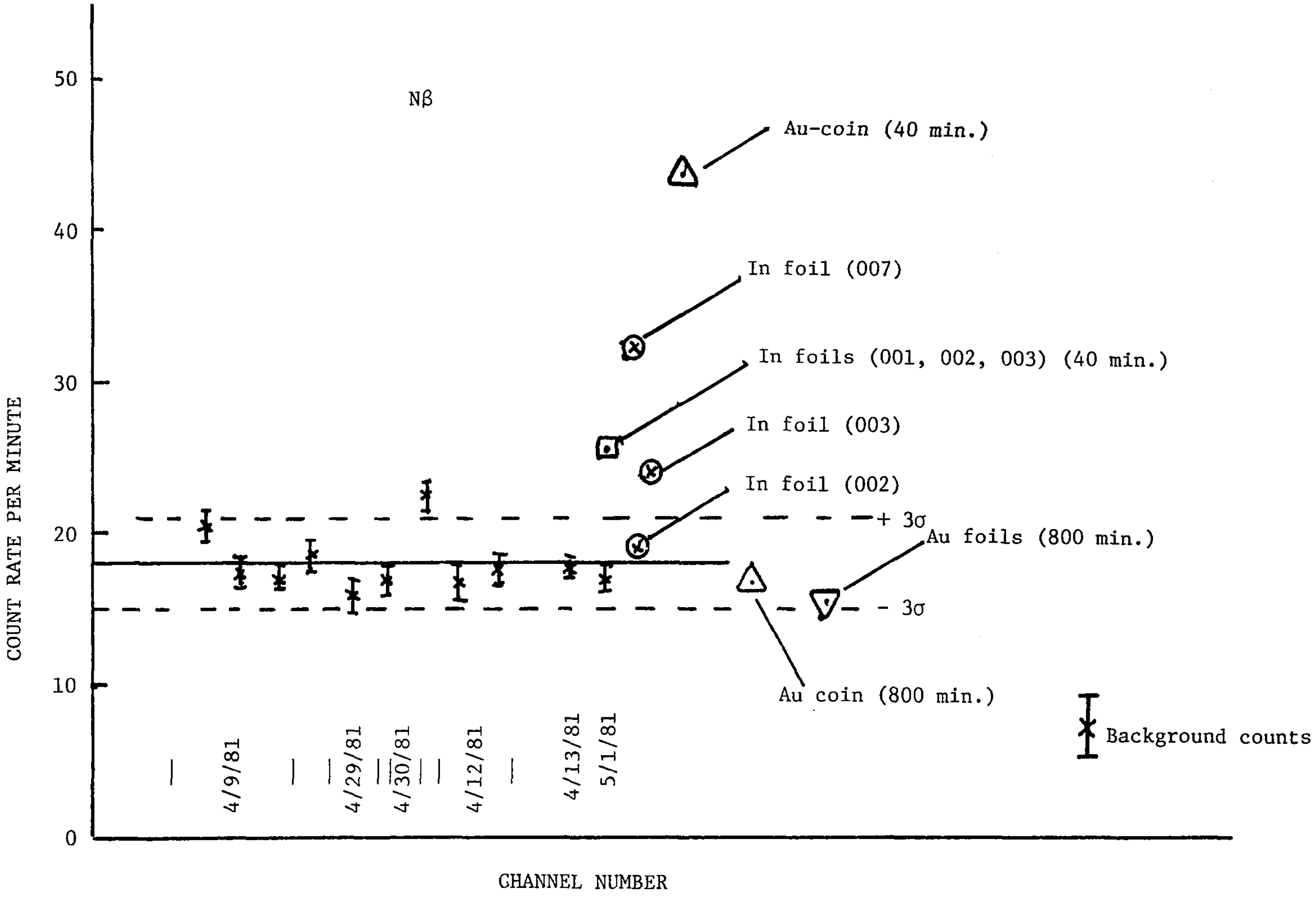

FIGURE 3 RESULT OF N_β COUNTING

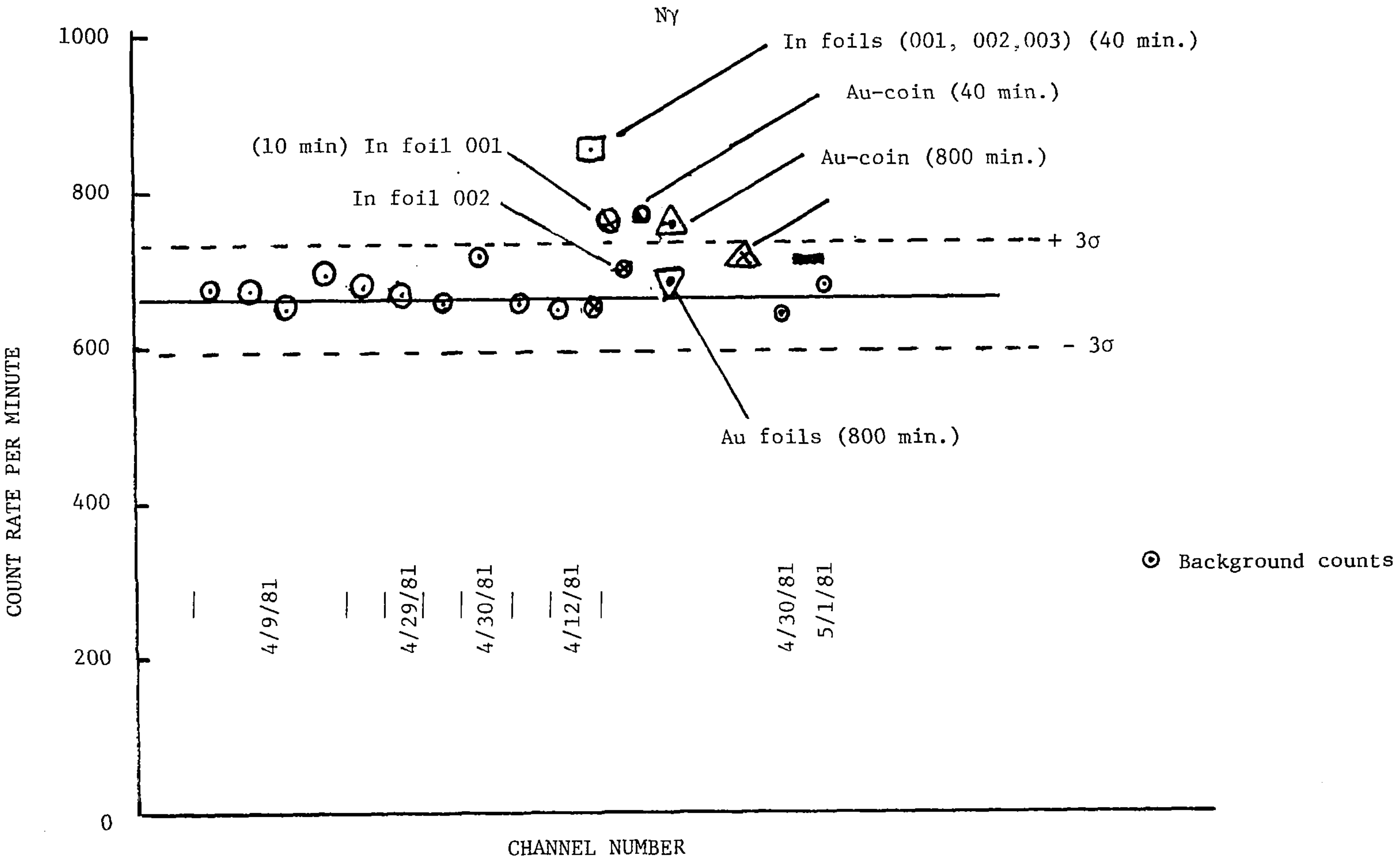

FIGURE 4 RESULT OF N_γ COUNTING

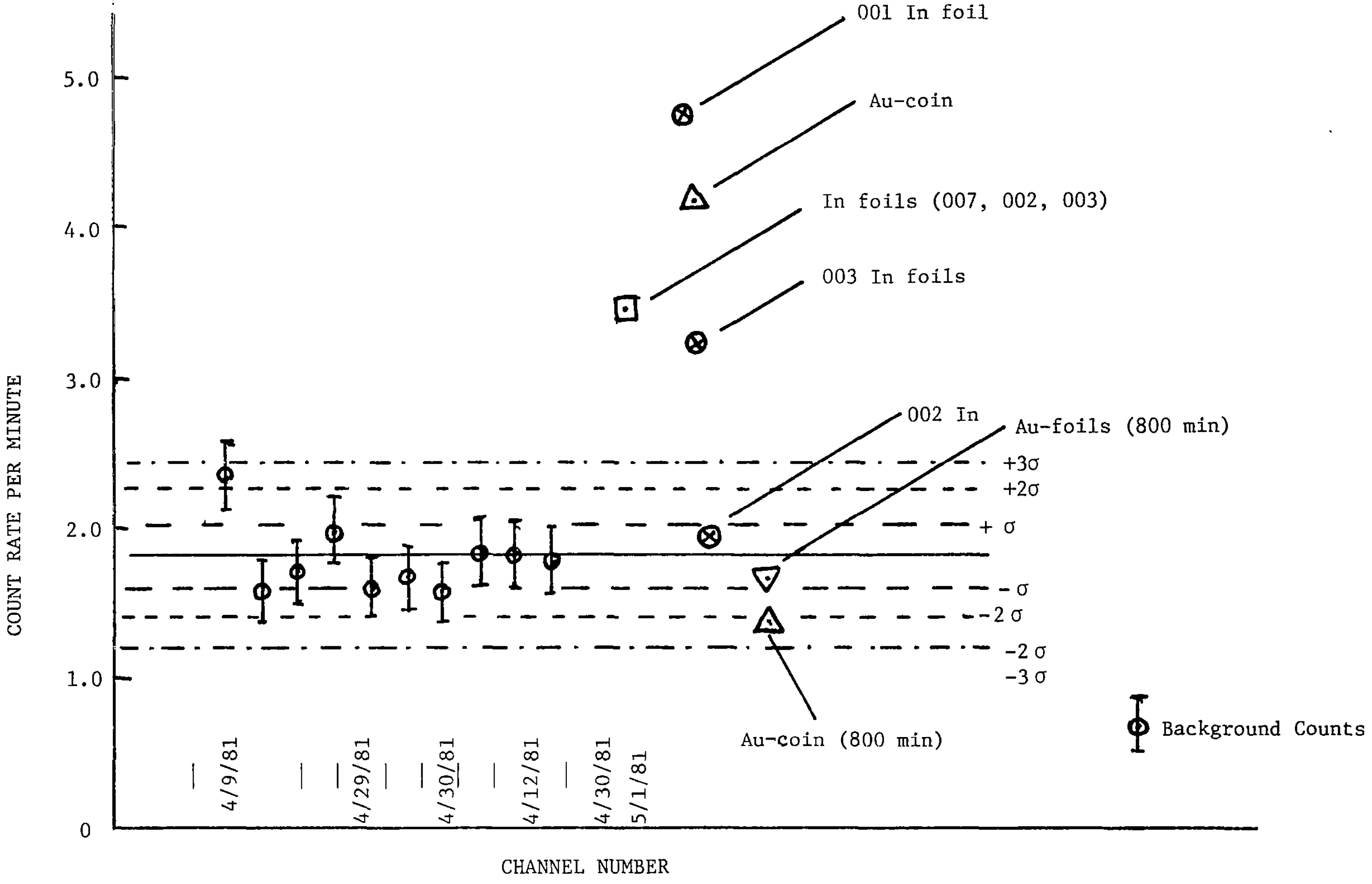

FIGURE 5 RESULT OF $N_{\beta\gamma}$ COUNTING

FIGURE 6

10 Minute Count of In Sample #1
3 pt - Smoothed
4/12/81

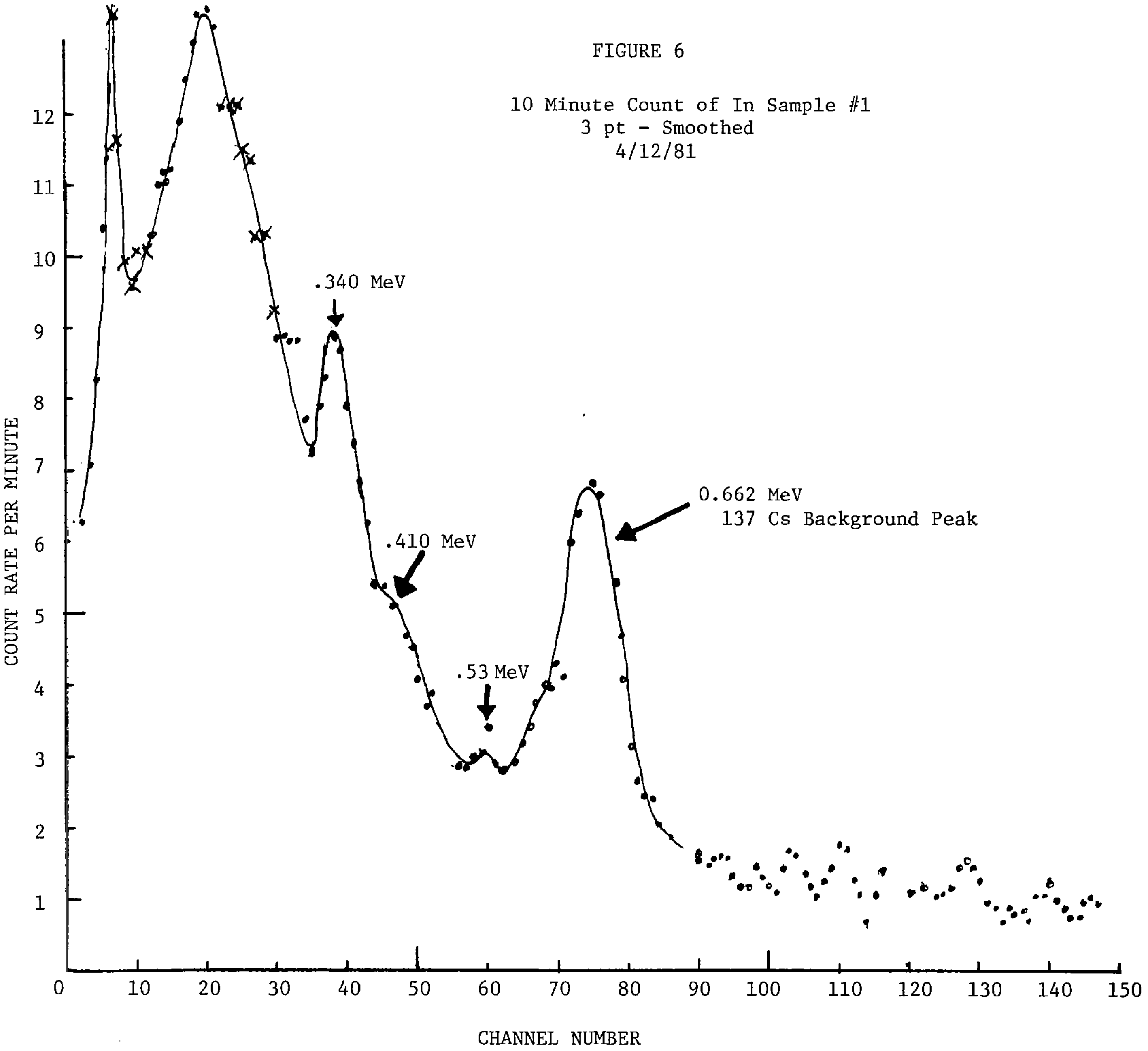

FIGURE 7

GATED/UNGATED SPECTRUM INDIUM FOILS
4/12/81

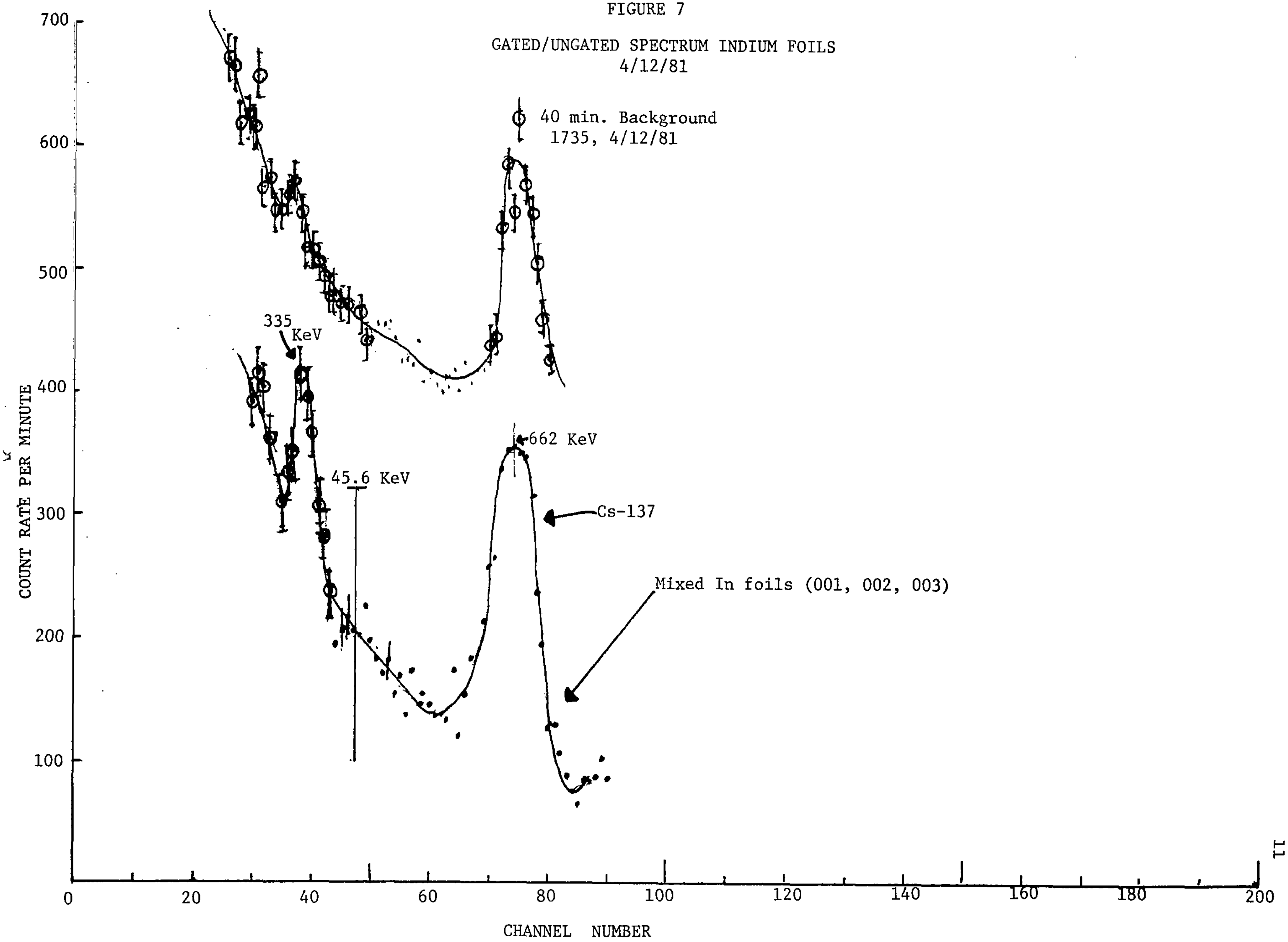

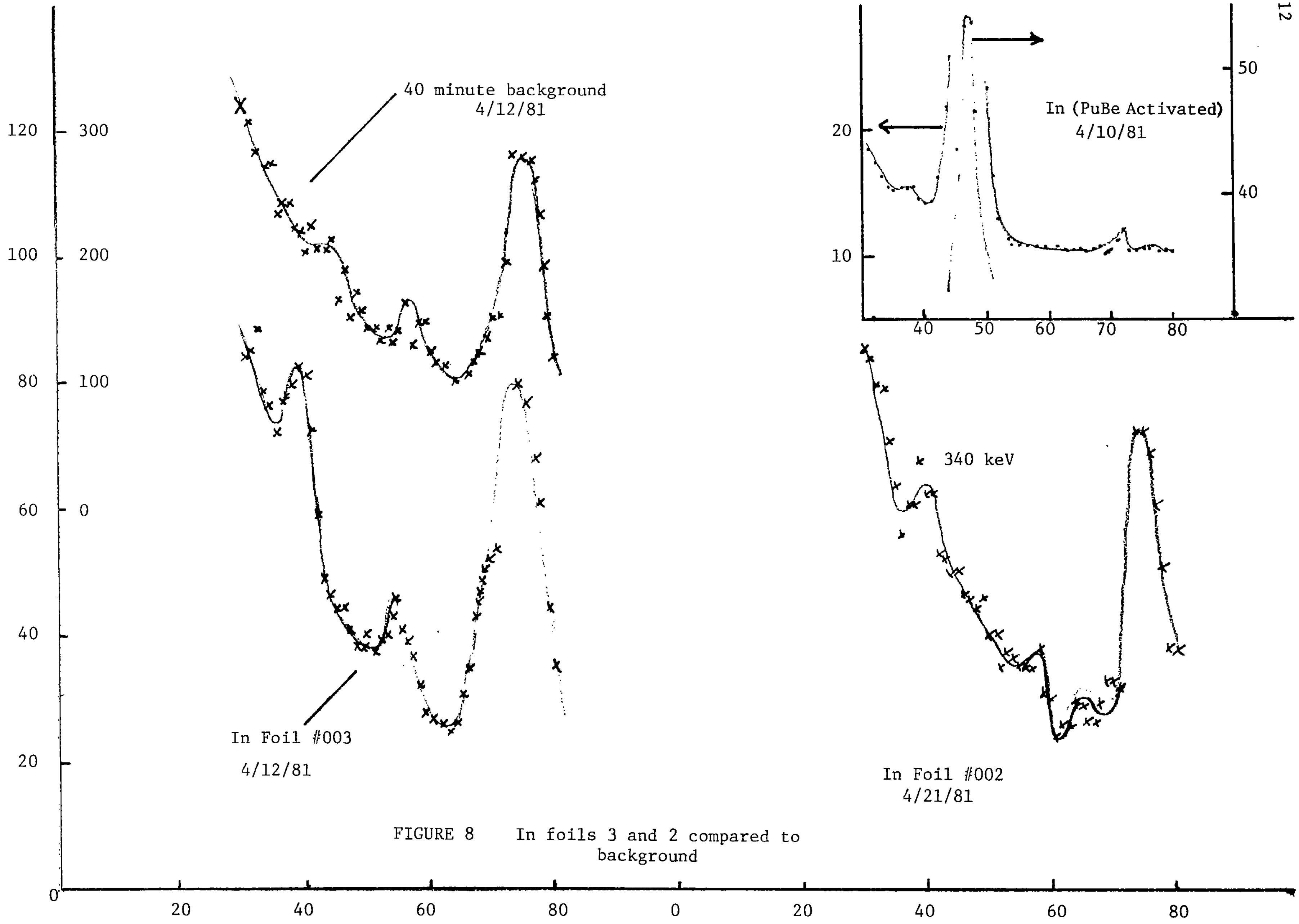

FIGURE 8 In foils 3 and 2 compared to background

As summarized in Table I, it was observed that indium foil # 002 exhibited neither counting rates greatly different from background nor spectral features not found present in the background gamma ray spectrum. However, indium foils numbered 001 and 003, whose counting rates were significatly greater than background also exhibited spectral features that were not found present in the background. Foil # 001 exhibited two such features, one in the channel range of the 417 gamma ray peak of ^{116m}In and the other in the range of the 511 keV positron annihilation peak. Yet, only the latter appreared in the spectrum of foil # 003, while only the former appeared distinctly in the spectrum for the combined foils. Further, it should also be noted that the 54 minute ^{116m}In activity is produced predominantly by thermal and/or epithermal energy neutrons, while positron activity is most frequently associated with charged particle or fast neutron ((n, 2n)) induced reactions or high energy gamma ray induced electron-positron pair formation.

The counting rate obtained for the 40-minute measurement of the gold coin (which was started after two (2) hours and eighteen (18) minutes waiting time) was 2.4, 1.29 and 2.31 times larger than the average values measured for the background for the beta, gamma and beta-gamma counting systems, respectively. However, for the later and longer counts, i.e., 800 minute count (Au coin waiting time was T_w = 7 hrs. + 16 min.) the counting rates observed were approximately equal to or less than background and had values that were within 3σ of the background counting rate, indicative of little or no sample contributed radioactivity. The same characteristics is seen to hold for the gold foils which had a waiting time T_w = 44 hrs. + 19 minutes. This suggests that any activity that may hve been present in the gold coin or foils, would have had to be quite short lived with respect to the 2.7 day lifetime of neutron activated ^{198}Au.

TABLE I

SUMMARY OF In FOIL COUNTING RESULTS

COUNTS				SPECTRAL FEATURES
	N_β	N_γ	$N_{\beta\gamma}$	
In # 001 (10m)	$>\mathrm{BG}$	$>\mathrm{BG}$	$>\mathrm{BG}$	335, 406, 515, 662 keV (Cs-137)
In # 002 (10m)	$\overline{\sim\mathrm{BG}}$	$\overline{\sim\mathrm{BG}}$	$\overline{\sim\mathrm{BG}}$	340, 505, 662 keV (Cs)
In # 003 (10m)	$\overline{>\mathrm{BG}}$	$\overline{>\mathrm{BG}}$	$\overline{>\mathrm{BG}}$	340, 483, 662 keV
Combined (40 min.):	$\overline{>\mathrm{BG}}$	$\overline{>\mathrm{BG}}$	$\overline{>\mathrm{BG}}$	335(1), 414, 662 keV
Background (40 min.):				335(s), 662 keV

The ungated gamma spectrum obtained with a 40 minute count of the gold coin at 16:45, 12 April 1981, (∿ 2¼ hrs. wait), exhibited no clearly distinguishable spectral features not seen in the other ungated gold spectra for the longer counting periods and at later times, other than the peak at channel 38 (or 340 keV). The ^{137}Cs gamma peak and spectral features are again sharply defined.

The spectra obtained during the long term counting measurements for the gold coin and foils showed little other than the ^{137}Cs peak for the ungated gamma ray spectra, however the smoothed gated spectra exhibited other features, these being the channel 38 peak (∿ 340 keV), as seen earlier, and the channels 55-56 peak (∿ 511 keV), also seen earlier. No ^{137}Cs peak contribution was observed as can be seen in Figure 9. The same was true for the spectra obtained with the multiple gold foil sample, as was shown in Figures 10 and 11. Table II summarizes the gold-coin activation measurements.

The failure to observe the 411 keV ^{198}Au gamma ray peak in contrast to the apparent radioactivation of the Indium foils, resulted in the decision to choose indium foils as the detector system for the second series of measurements.

The beta-discriminator was lowered to better accomodate the lower energy of the indium beta rays. This led to an approximately doubled beta counting rate sensitivity.

For counting system calibration and set-up, a set of indium foils were activated with both a 5 Ci PuBe source and a small ^{252}Cf source ($\phi = 10^2$ n/cm^2 seconds) and the samples counted. The system showed excellent sensitivity for the indium activity, however, the ^{137}Cs gamma ray background persisted as can be seen in Figures 12 and 13. A careful wash-down with a detergent successfully removed most of the ^{137}Cs activity, especially its effect on the gamma ray spectra. The results are shown in Figure 14.

FIGURE 9

GOLD COIN SAMPLE GATED GAMMA SPECTRUM

12-14 April 1981 (2152.46 m (∿36 hrs))

2143.12 April 1981

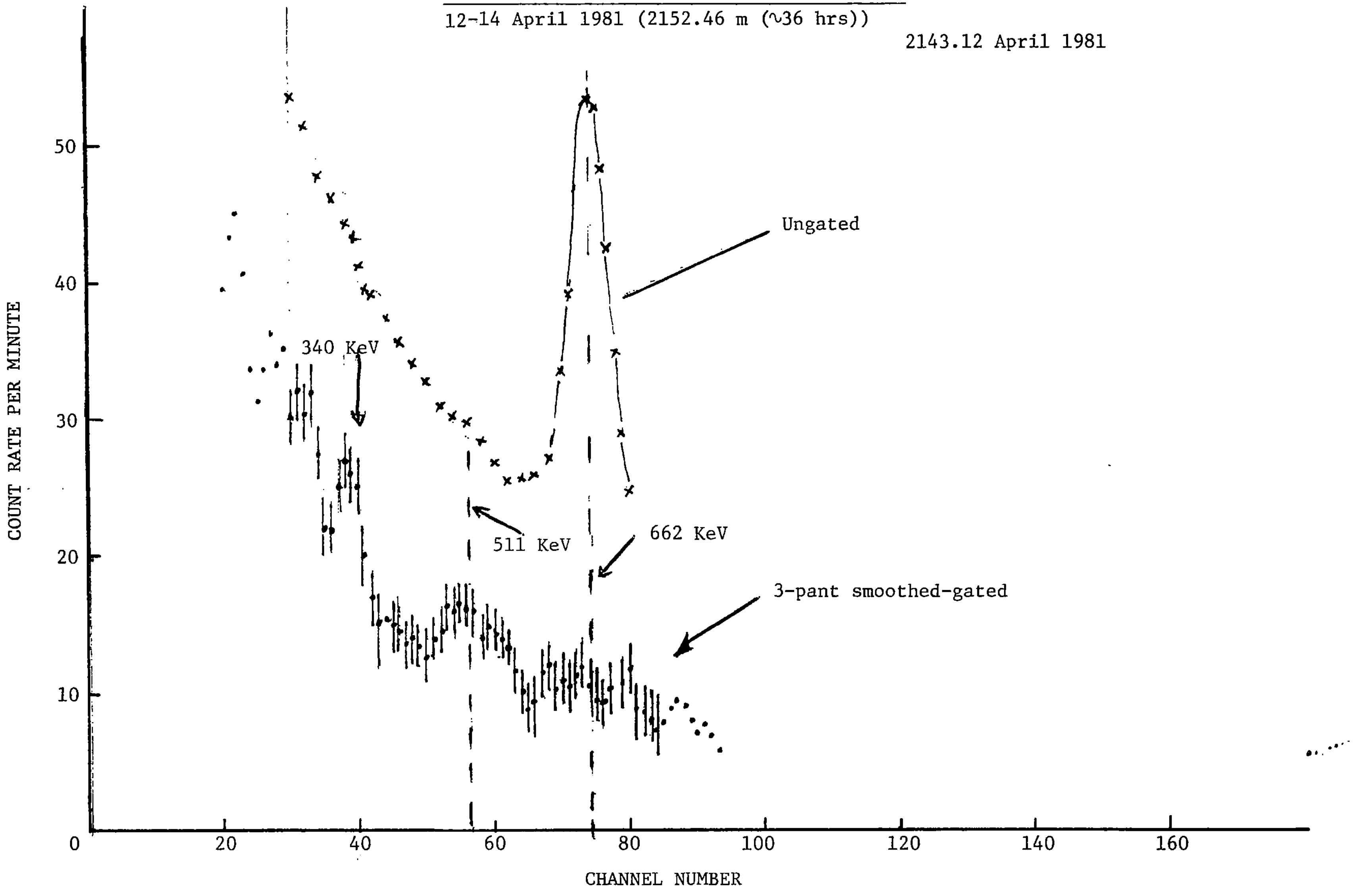

FIGURE 10

UNGATED MULTI-GOLD FOIL SAMPLE SPECTRUM
14 April 1981 to 17 April 1981
(1046, 14 April 1981)

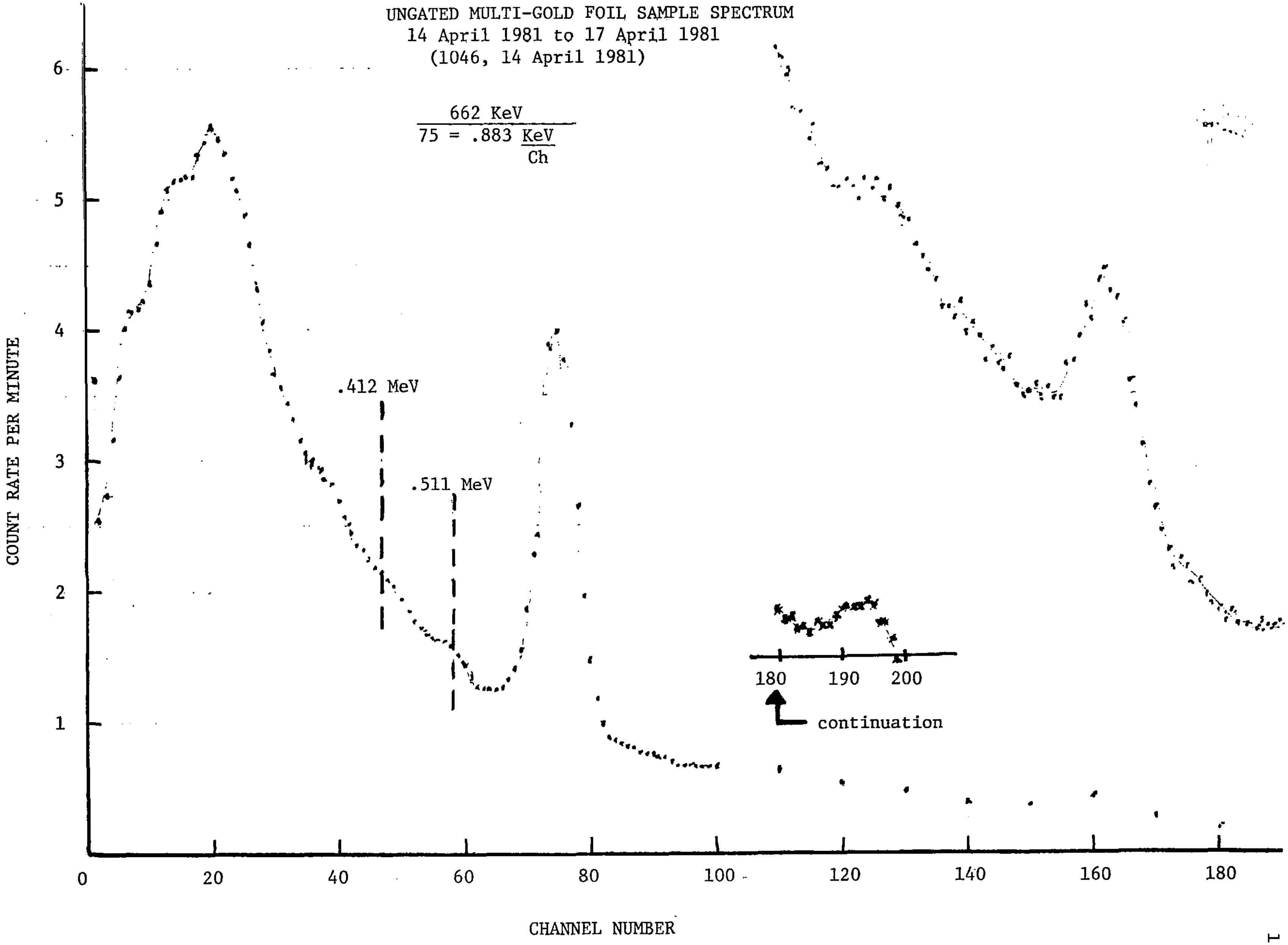

FIGURE 11

MULTI-GOLD FOIL SAMPLE SPECTRUM (GATED)
(1046, 14 April 1981) to 17 April 1981) 78.9 hrs.

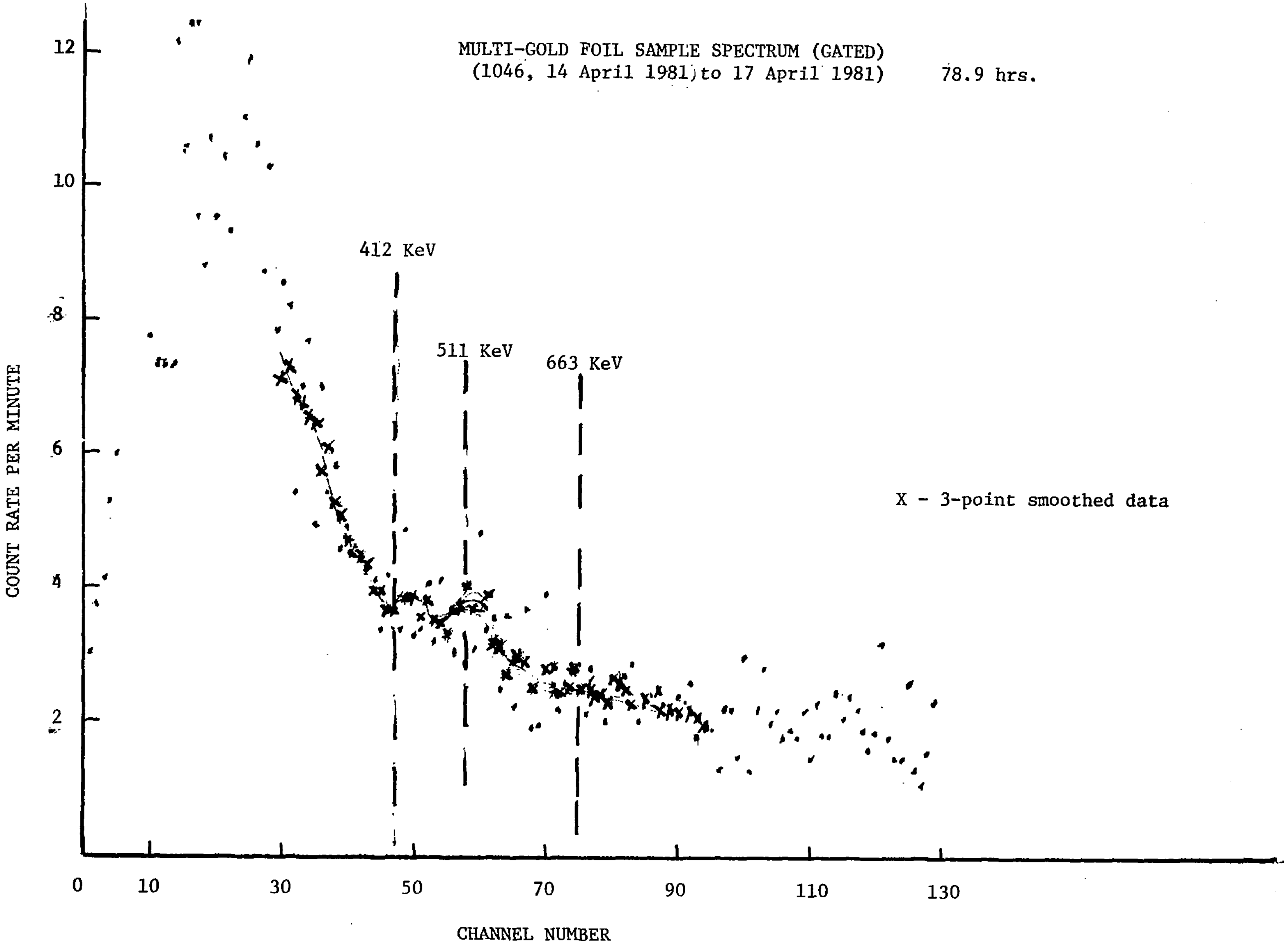

TABLE II

SUMMARY OF GOLD DETECTOR COUNTING RESULTS

COUNT RATE	N_β	N_γ	$N_{\beta\gamma}$	SPECTRAL FEATURES
Au Coin 40 min.	2.42BG	1.29BG	2.31BG	40m (ungated) 340 keV, 662 keV
800 min.	0.92BG	1.06BG	.78BG	∿36 hrs. (ungated), 662 keV 340 keV, 511 keV (gated)
Au Foils				
800 min.	0.86BG	1.03BG	.89BG	ungated , 662 keV gated, 511 keV

It should be noted in Figure 14, the gamma spectra of an activated In foil and that of background, the peaks observed previously at 662 and approximately 340 keV, are absent. This result substantiates that the shields were cleaned thoroughly. However, peaks arising from activation of ^{24}Na (15 hrs.) do appear, primarily due to the samples having been left on the ^{252}Cf activator set-up for several days, allowing the ^{24}Na to build up further toward its asymptotic limit, while the indium activity remained essentially constant. This, it appears likely that the $\sim$340 keV peak may also be part of the systems response to the background.

The cleaned and adjusted system was tested, calibrated and then transferred to RTS Laboratories for a new series of foil exposures and measurements to be undertaken.

On 13 May, 1981 the D_2 discharge was operated for one (1) hour with the In foils in place. The In detector foils were then transferred to the counter and counted for a 40 minute period.

The results of the first measurement did not appear to differ significantly from background. Also, during a background count immediately following the first measurement, it was noted that the beta and coincidence counters would intermittantly count at extremely high rates, resulting in their total counts for the period of measurements reaching values of 50 to 100% higher than previous values, attempts to identify the sources of the spurious counts were unsuccesful at first. The operation of the counting system was monitored throughout the day of 14 May and up the point when the high frequency for the discharge was turned on. The noise source had apparently disappeared and the counting rates due to background was observed to be less than that at the regular location of the equipment (the University of Florida).

In Figure 15 the indium foil spectrum is plotted along with calibration curves and peaks from a ^{22}Na source (511 keV), ^{137}Cs and ^{60}Co. No obvious expression of peaks observed in previous measurements is shown. The information

FIGURE 12

THREE POINT SMOOTHED

^{252}Cf ACTIVATED In-FOILS (IRRADIATION TIME ∿ 1 HOUR)
GATED SPECTRUM $\beta - \gamma$ COINCIDENCE

1 MAY 1981

40 MINUTE COUNT TIME

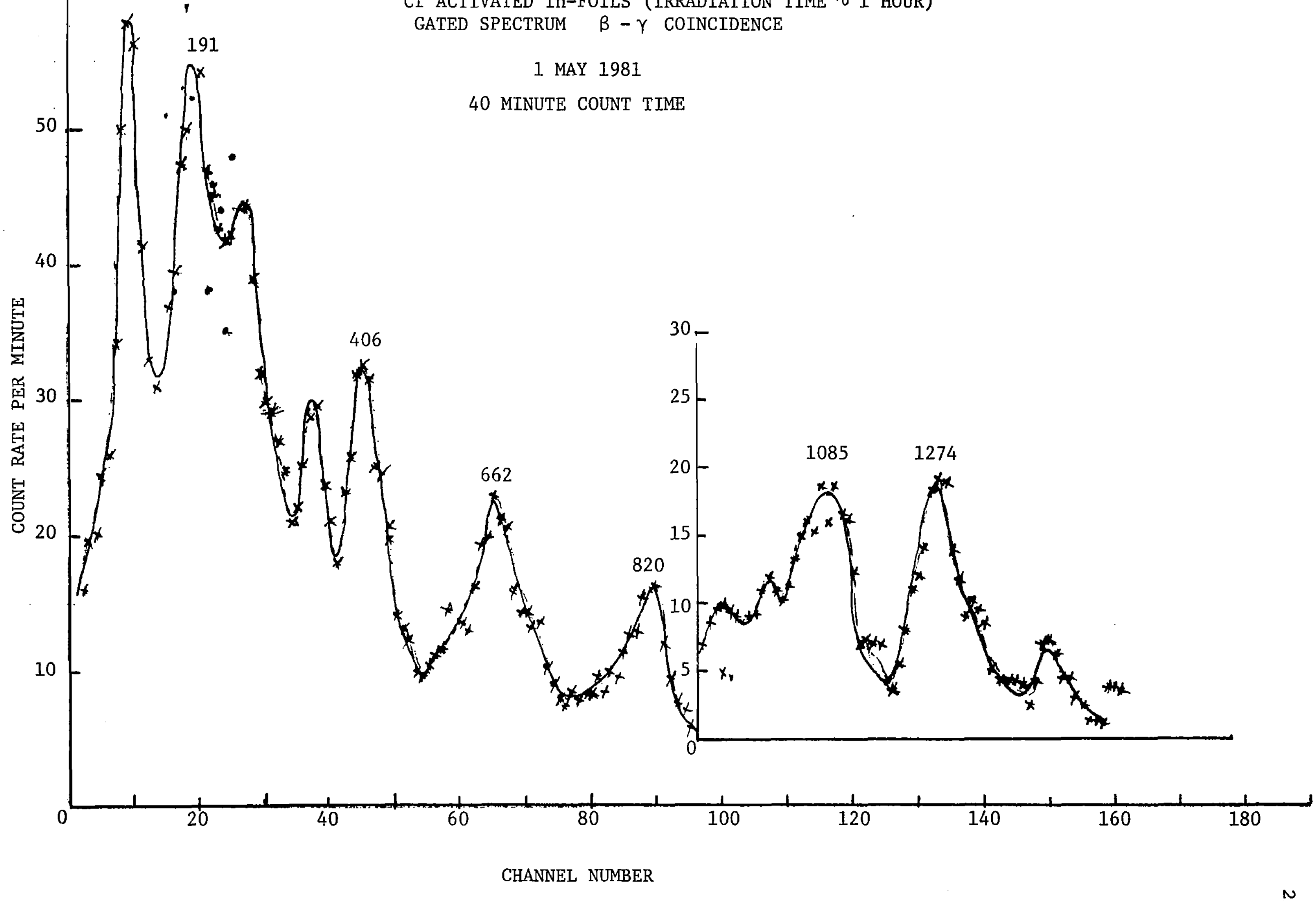

FIGURE 13

INDIUM FOIL ACTIVATED WITH Cf-252 SOURCE (THERMALIZED)

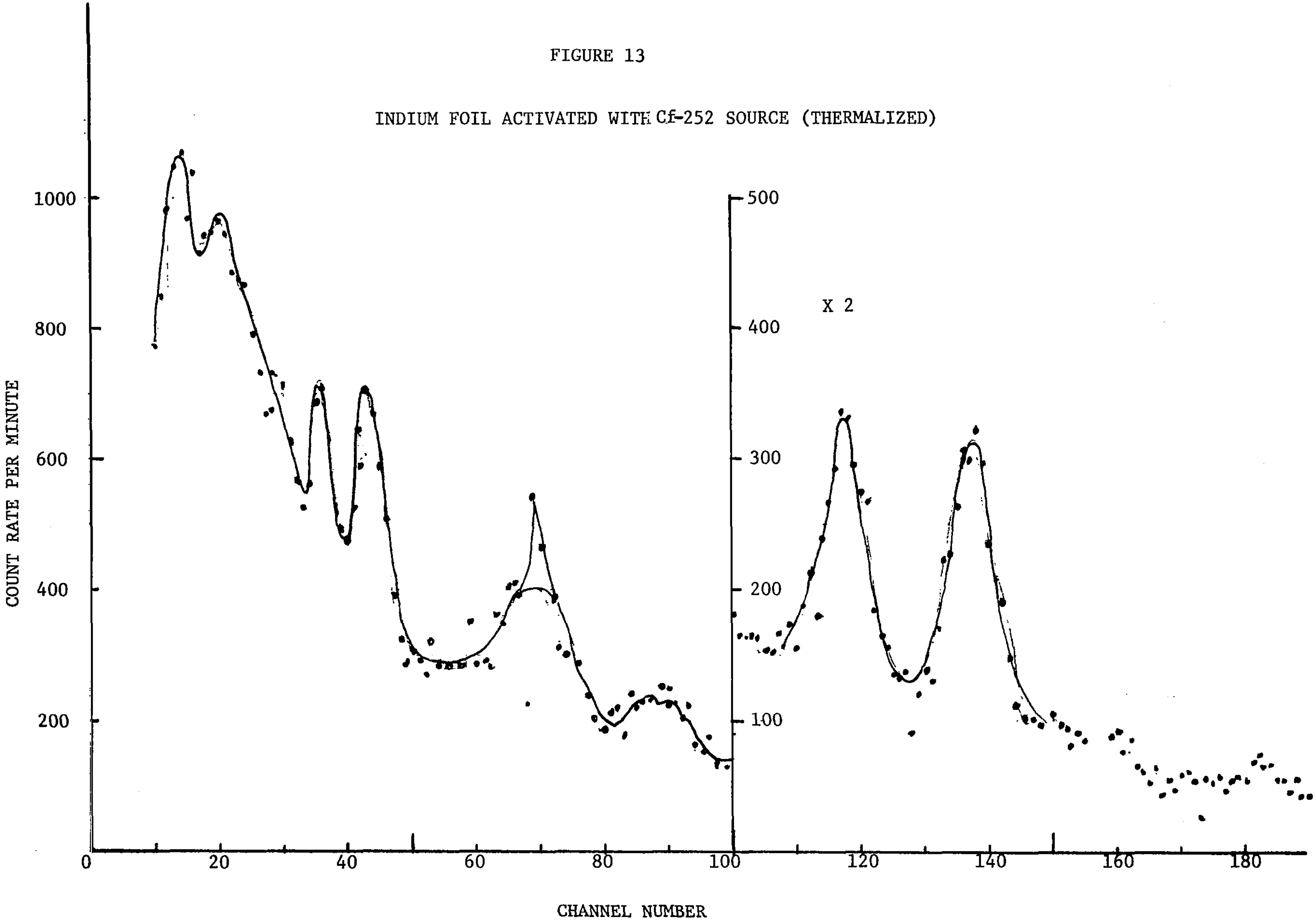

FIGURE 14

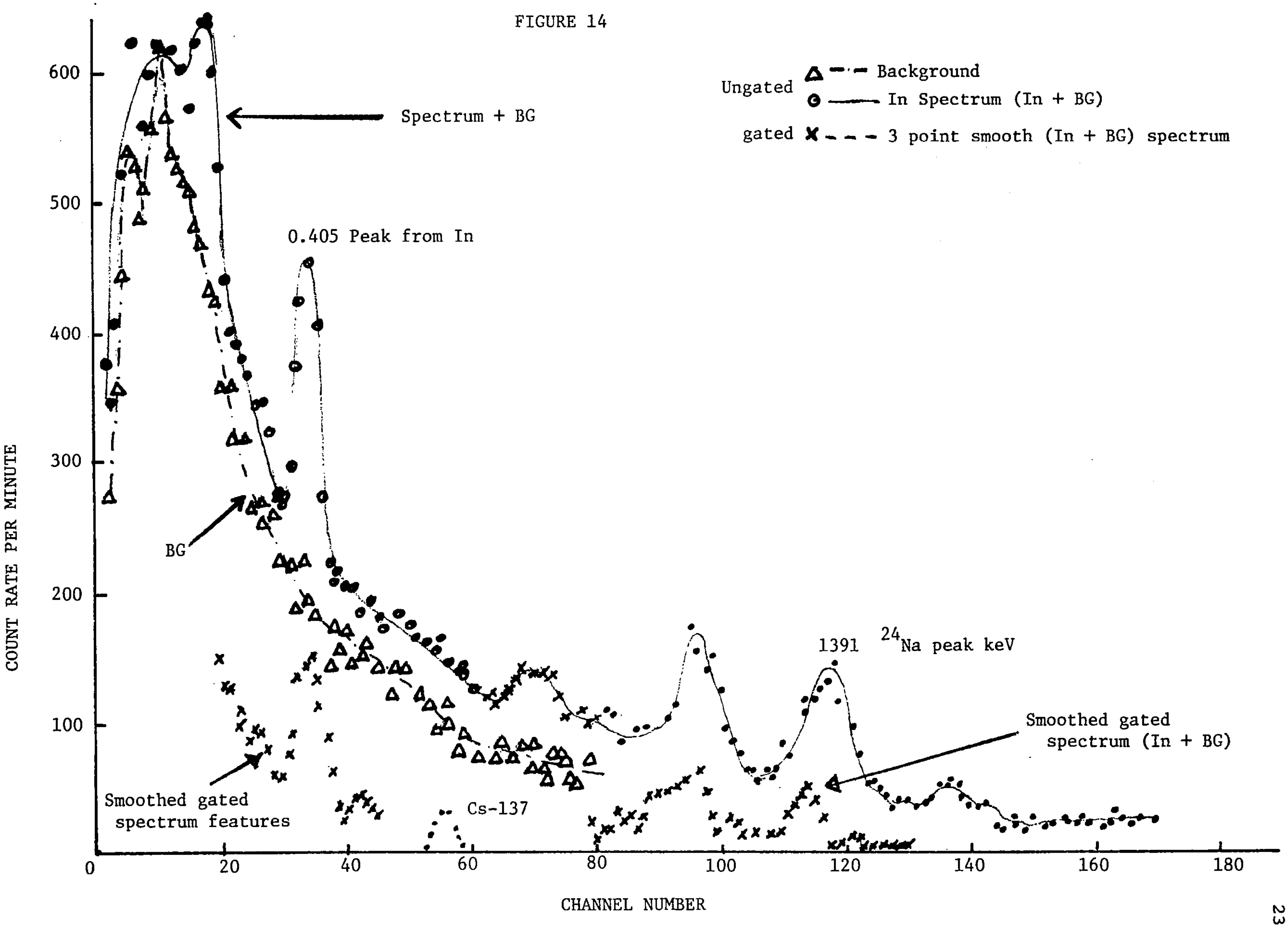

Ungated
Background
In Spectrum (In + BG)
gated
3 point smooth (In + BG) spectrum
Spectrum + BG
0.405 Peak from In
BG
1391
^{24}Na peak keV
Smoothed gated spectrum (In + BG)
Smoothed gated spectrum features
Cs-137
COUNT RATE PER MINUTE
600
500
400
300
200
100
0
20
40
60
80
100
120
140
160
180
CHANNEL NUMBER

plotted was obtained when the indium foils were used as flux detectors on the second round of experiments, 13 May 1981, with the D_2-discharge (conditions were not found to be optimum for the discharge).

For comparison, the background spectrum is shown in Figure 16. Many of its features appear to have contributed to the other measurements. The final figure, Figure 17, shows a peak at approximately 511 keV. This latter spectrum was obtained on 15 May 1981, for a set of three In foil detectors, which has been exposed in the vicinity of the D_2 discharge for a period of approximately 1 hour. Even though the total counts, especially the beta and coincidence counting rates exhibited a sensitivity to low amplitude, high frequency "noise" pulses appearing on the oscilloscope display, the gamma ray spectra appear to be relatively free of perturbing aspects, with the principal characteristics observed being the peak at 511 keV.

Conclusions

The counting rate measurements completed thus far have exhibited certain results that have been significantly greater that the average value of the observed background counting rates, indicative of radioactivity sources other than background.

Spectral measurements thus far have failed to disclose characteristics expected for thermal neutron activated gold, both in terms of peak energies and lifetimes. Spectral features characteristic of thermal neutron activated indium were observed for some but not all of the indium foil spectra. However, peaks have been observed in the spectra at 511 keV, the gamma ray energy associated with the positron annihilaiton process. Also, the apparent lifetime of the apparent radioactivity appears to be distinctly shorter than that due to ^{198}Au (2.7 days).

Thermal neutron activated ^{64}Cu (12.8 hrs.) can yield positrons from which annihilation radiation could arise, should copper be a constituate of

FIGURE 15

In FOIL SPECTRUM WITH CALIBRATION CURVE
5/13/81

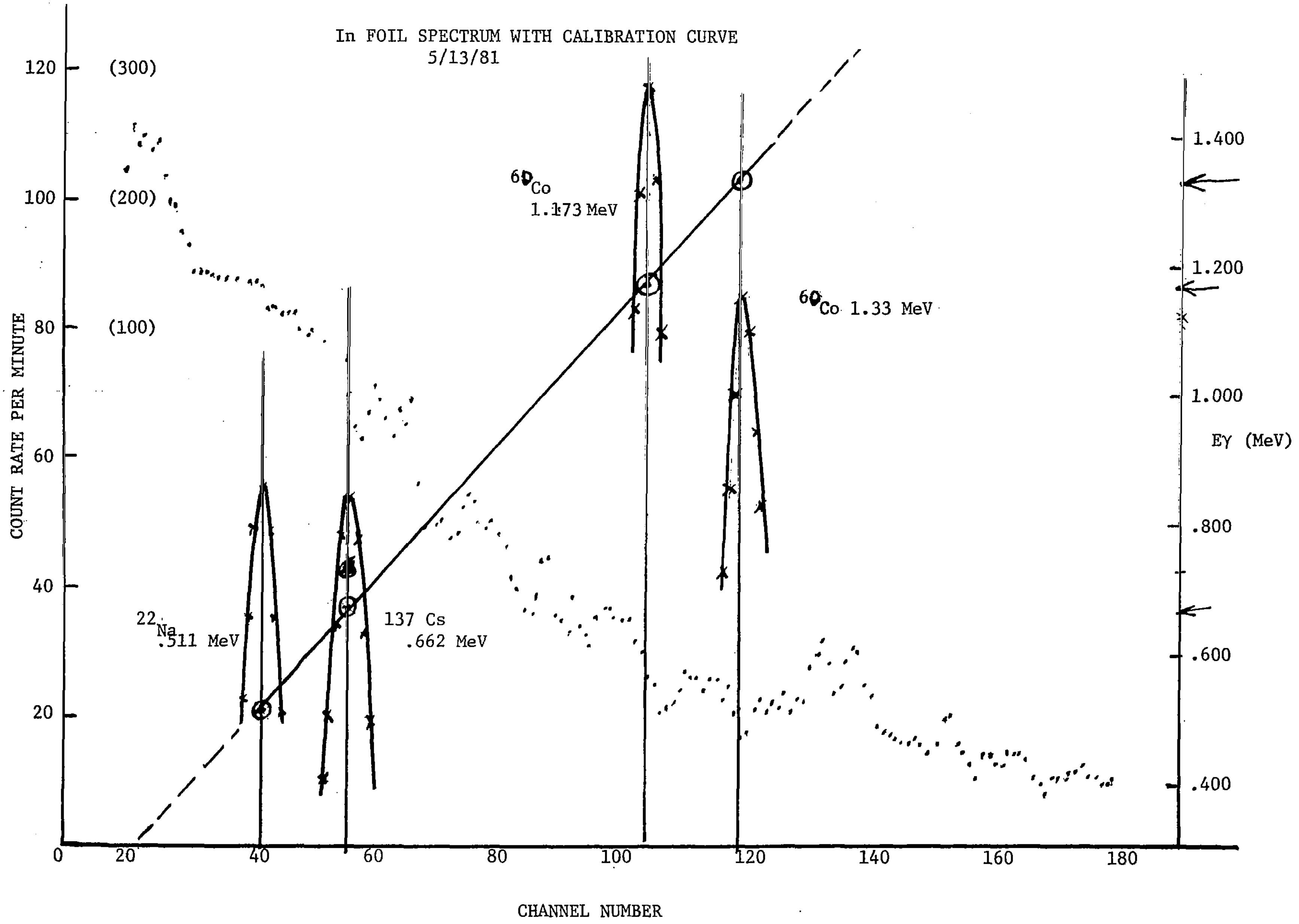

FIGURE 16

40 MINUTE BACKGROUND SPECTRUM BACKGROUND*

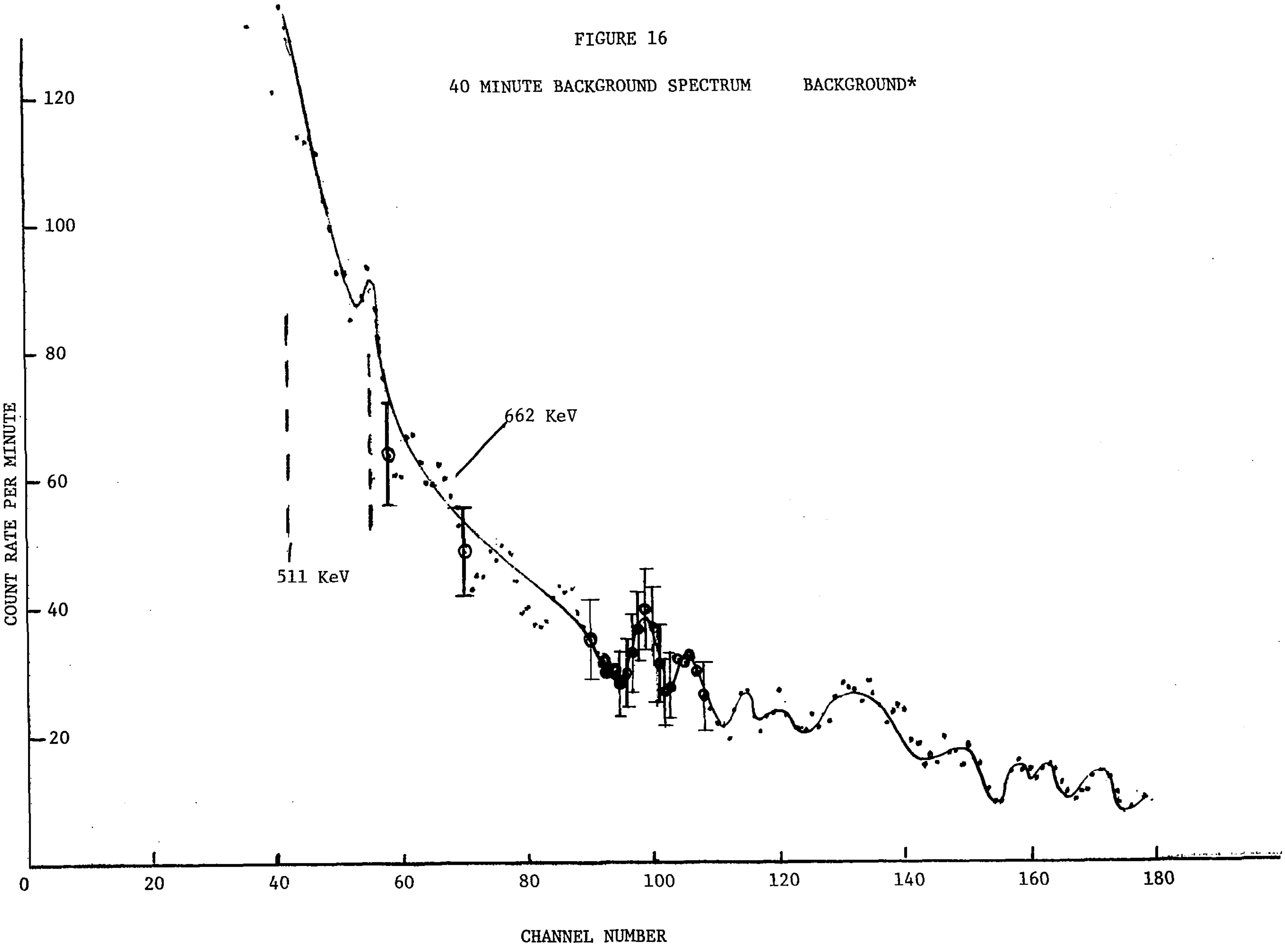

FIGURE 17

3-INDIUM FOIL MEASUREMENT

15 May 1981

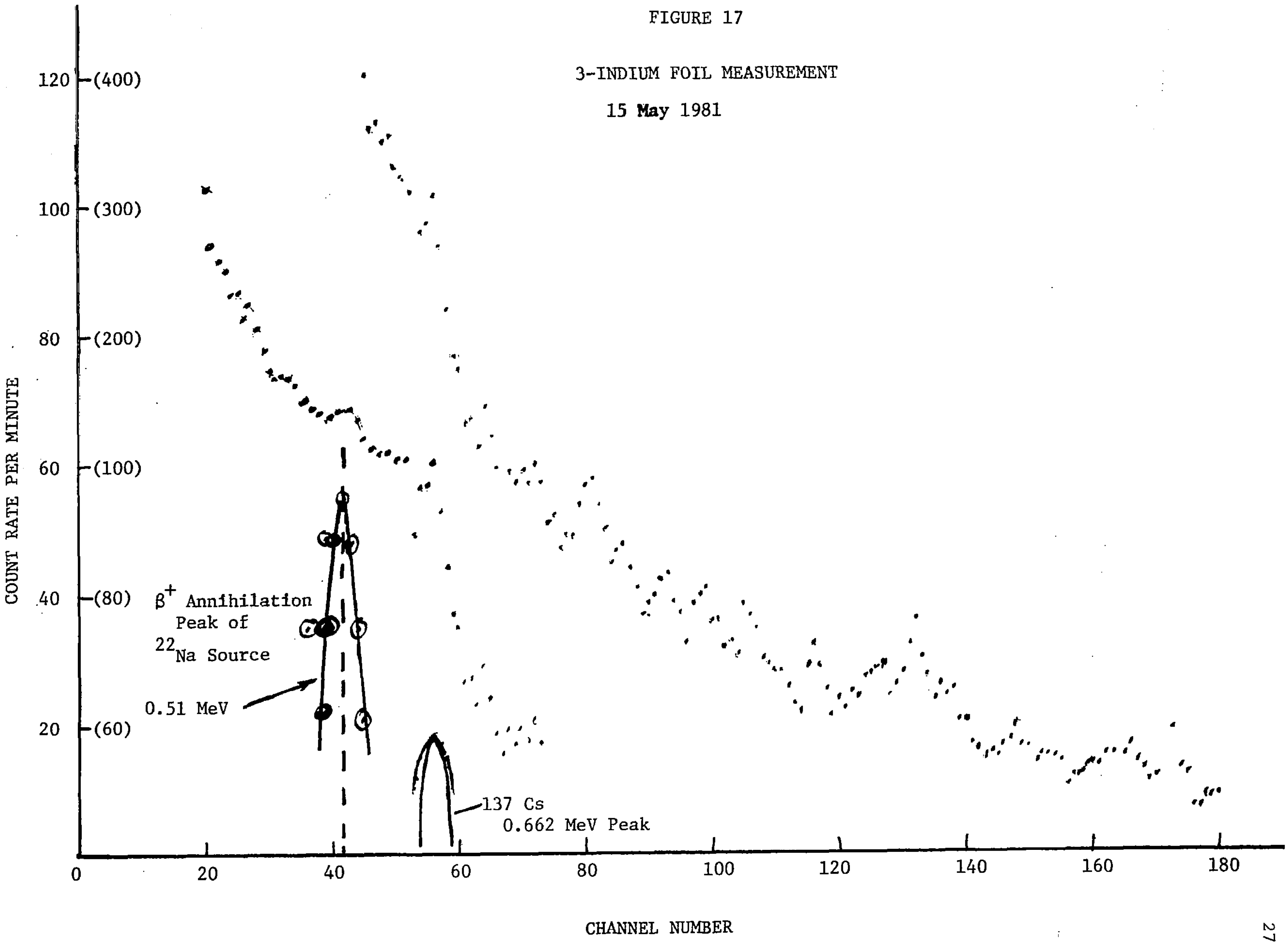

the Au coin or foil. However, its lifetime too does not correlate with some of the characteristics observed.

Fast neutron activation through the (n, 2n) reaction can produce positron activity in many materials, yet gold's (n, 2n) reaction products are principally electron capture (EC) or beta minus decay species. Indium has an (n, 2n) positron emitting product but from its least abundant isotope.

Our efforts this far have posed further questions without providing any absolute answers. More carefully controlled measurements are needed to assure that the background contributions are better quantitated. A series of measurements, including replicates, need to be performed. These should be counting rate, spectral and time dependent. Measurements should also be made with the higher resolution germanium detectors.

The apparent cross sections for the reactions that may have produced the observations must be relatively small, causing their measurement to be difficult. This is also probably true for the intensity of whatever process that may be responsible for the apparent radioactivation. Thus, subsequent measurements must be done very carefully in order to optimize the exposure times, measurement processes, data storage, retrieval, output in graphical and tabular forms.

1. Report No. NASA CR-3570	2. Government Accession No.	3. Recipient's Catalog No.
4. Title and Subtitle GENERATION OF X-RAYS AND NEUTRONS WITH A RF-DISCHARGE		5. Report Date June 1982
		6. Performing Organization Code
7. Author(s) Richard T. Schneider		8. Performing Organization Report No. RTS-2/82
		10. Work Unit No.
9. Performing Organization Name and Address RTS Laboratories, Inc. 2603 N. W. 74th Place Gainesville, Florida 32606		11. Contract or Grant No. NAS1-15812
12. Sponsoring Agency Name and Address National Aeronautics and Space Administration Washington, DC 20546		13. Type of Report and Period Covered Contractor Report
		14. Sponsoring Agency Code

15. Supplementary Notes

Langley Technical Monitor: Nelson Jalufka
Final Report

16. Abstract

An experimental study concerning disk shaped plasma structures was performed. Such disk-shaped structures can be obtained using an rf discharge in hydrogen. The applied frequency was 1-2 Mhz. In case of operation in deuterium it was found that the discharge emits neutrons and x-rays, although the applied voltage is only 2 kV. This phenomenon was explained by assuming formation of plasma cavitons which are surrounded by high electric fields. The condition for formation of these cavitons is that the applied rf frequency is equal to the plasma frequency. The ions trapped in these resonance structures acquire sufficient energy that they can undergo fusion reactions with the ions in the surrounding gas.

17. Key Words (Suggested by Author(s)) Cavitons Fusion D-D Reaction	18. Distribution Statement Unclassified - Unlimited Subject Category 75

19. Security Classif. (of this report) Unclassified	20. Security Classif. (of this page) Unclassified	21. No. of Pages 150	22. Price A07

For sale by the National Technical Information Service, Springfield, Virginia 22161

NASA-Langley, 1982